# APPLICATION OF COMPUTATIONAL FLUID DYNAMICS FOR LIQUEFIED NATURAL GAS POOL SPREADING AND VAPORIZATION ON WATER

A Dissertation

by

NIRUPAMA GOPALASWAMI

Submitted to the Office of Graduate and Professional Studies of
Texas A&M University
in partial fulfillment of the requirements for the degree of

DOCTOR OF PHILOSOPHY

| | |
|---|---|
| Chair of Committee, | M. Sam Mannan |
| Committee Members, | N. K. Anand |
| | James Holste |
| | Mahmoud El-Halwagi |
| Head of Department, | M. Nazmul Karim |

May 2016

Major Subject: Chemical Engineering

ABSTRACT

Liquefied Natural Gas (LNG) is a cryogenic liquid consisting predominantly of methane compressed to 1/600$^{th}$ of its gaseous volume for transportation. A release of LNG on water during marine operations can occur due to several factors. Upon release, a spreading liquid can form a pool with rapid vaporization, leading to the formation of a flammable vapor cloud. Safety analyses for the protection of the public and property involve the determination of consequences of such releases. The evaluation of consequences resulting from a spill of LNG on water involves the determination of the rate (vaporization rate/source-term) at which flammable hydrocarbon vapor is produced and the dynamics of the spreading pool. Two key parameters which affect pool spreading and vaporization, namely the heat flux to the LNG pool and the turbulence present within the cryogenic pool, are quantified separately through experiments. The heat flux from two different substrates comprised of water and ice is studied. The vaporization mass flux is directly influenced by the water temperature and the release rate. Similarly, the vaporization mass flux is directly influenced by the ice temperature when cryogenic liquid is released on ice. The experiment for quantification of turbulence present in cryogenic pool was performed using a high-speed camera. Flow visualization for turbulence quantification revealed the presence of wavy-structures called ‘thermals’ which catalyzed the vaporization process of cryogenic liquid released on water.

The results of key parameters study are implemented in CFD methodology to study the pool spreading and vaporization behavior. The CFD model is validated with an LNG experiment which simulates the LNG spill in space enclosed by two LNG ships

during loading operations. The results of the research can be used for decision making in facility siting studies and emergency response planning for near shore/waterfront LNG facilities.

DEDICATION

This dissertation is dedicated to the memory of my father

Gopalaswami

[1952-2015]

You are deeply missed.

To my mother for her unwavering support and affection

All my success and failures go to your feet

ACKNOWLEDGEMENTS

I would like to express my sincere appreciation to my advisor Dr. Sam Mannan for offering this challenging research and continuous support during my PhD. I would also like to thank him for providing me multiple opportunities to develop myself personally and professionally. I would like to thank my committee members Dr. James Holste, Dr. Mahmoud El-Halwagi and Dr. N.K. Anand for their guidance throughout the course of this research. Special thanks to Dr. Ray Mentzer for sharing his experience and offering guidance during my PhD.

I would like to thank the Chemical Engineering Department at Texas A&M University, Qatar for allowing me to perform field experiments. I would like to show gratitude to Dr. Luc Vechot and Dr. Tomasz Olewski for extending help in my research. I would also like to acknowledge the help extended by the staff members of Qatar Petroleum for my experiments at Ras Laffan, Qatar. I am also thankful to Mr. Nelson Antonio of Texas A&M Qatar for constructing my experimental setup. I am also grateful to Dr. Konstantinos Kakosimos for guidance and advice on CFD and generously taking time to discuss various aspects of my research. He is one of the key persons in this research and his expertise is highly appreciated.

Special thanks to Dr. Delphine Laboureur for assisting and guiding me in the flow visualization experiments. Her friendship, encouragement and wholehearted support are highly valued. I would also like to extend my appreciation to Dr. Devesh Ranjan and his students for providing the high speed camera and technical support in

flow visualization experiments. I would like to acknowledge the help extended by Mr. Randy Marek in my experimental setup.

LNG experiment expertise and assistance provided by Mr. Kirk Richardson and his team of fire fighters namely Mr. Ron Coombs and Mr. Kevin Schreiber from Texas Engineering Experiment Station (TEEX) is gratefully acknowledged. My warmest thanks go to the LNG team members comprising of Dr. Yi Liu, Dr. Bin Zhang and Dr. Josh Richardson for extending help in LNG experiment. I also want to extend my gratitude to all the Mary Kay O'Connor Process Safety Center (MKOPSC) students who participated in my LNG experiments. I would like express my appreciation to all the MKOPSC students who helped during the course of my study. Special thanks to the help extended by Valerie Green, Donna Startz, Alanna Scheinerman, and Tricia Hasan. I would like to thank BP Global Gas SPU and for their financial support in this research and National Grid for funding LNG for my experiment.

Finally, I would like to express my deep gratitude to my friends and family who helped me during my PhD. Special thanks goes to my brother and sister-in law for their affection and support. I would also like to thank my cousin and his wife for offering help during my PhD. I am also eternally grateful to my parents for their love and encouragement that they have shown me over the years.

Finally, I thank God for providing me wisdom and strength to complete my PhD and making my experience in College Station a memorable one.

.

# NOMENCLATURE

| | |
|---|---|
| BFTF | Brayton Fire Training Field |
| CCS | Cargo Containment System |
| CFD | Computational Fluid Dynamics |
| DTBTT | Ductile to Brittle Temperature Transition |
| EDR | Eddy Dissipation Rate |
| FLNG | Floating Liquefied Natural Gas |
| FSRU | Floating Storage and Regasification Unit |
| GBS | Gravity Based Structure |
| LNG | Liquefied Natural Gas |
| MKOPSC | Mary Kay O'Connor Process Safety Center |
| PERC | Powered Emergency Release Couplings |
| PPE | Personal Protective Equipment |
| RPT | Rapid Phase Transition |
| SIMOPS | Simultaneous Operations |
| TI | Turbulent Intensity |
| TKE | Turbulent Kinetic Energy |

## Alphabets

| | |
|---|---|
| $e$ | Thickness of ice (m) |
| $R$ | Radius of LNG pool (m) |
| $C_p$ | Specific heat Capacity (J/kg K) |
| $g$ | Acceleration due to gravity ($m/s^2$) |
| $h$ | Heat transfer Coefficient ($W/m^2K$) |
| $H_v$ | Latent Heat of vaporization (J/kg) |
| $k$ | Thermal Conductivity (W/mK) |
| $K_S$ | Spreading Constant |
| $m$ | Mass of the LNG pool (kg) |
| $q$ | Heat flux ($W/m^2$) |
| $t$ | Time (s) |
| $T$ | Temperature of LNG (K) |
| $V$ | Volume of the LNG pool ($m^3$) |
| $v$ | Velocity (m/s) |

## Greek Letters

| | |
|---|---|
| $\alpha$ | Thermal Diffusivity ($m^2/s$) |
| $\varepsilon$ | Constant in transition boiling |
| $\mu$ | Viscosity (kg/ms) |
| $\rho$ | Density ($kg/m^{3)}$ |
| $\sigma$ | Surface Tension (N/m) |
| $\varphi$ | Pre-factor for critical length |

## Subscripts

| | |
|---|---|
| *a* | Air |
| *c* | Critical Temperature |
| *con* | Convection |
| *Cr* | Critical value (Maximum) for heat flux and Temperature |
| *f* | Freezing |
| *L* | LNG liquid |
| *i* | Iteration Step |
| *Initial* | Initial |
| *ice* | Ice |
| *min* | Minimum |
| *rel* | Relative |
| *rad* | Radiation |
| *v* | LNG vapor |
| *vap* | vaporization |
| *w* | Water |

TABLE OF CONTENTS

Page

LIST OF FIGURES

Page

LIST OF TABLES

Page

# CHAPTER I

# INTRODUCTION

## 1.1. Overview of LNG

The demand for natural gas is increasing today in both onshore and offshore areas in different parts of the world. Liquefied Natural Gas (LNG) is a cryogenic liquid where natural gas has been condensed to 1/600th of its original volume by cooling it to a temperature of −162 °C (−260 °F). It consists primarily of methane, nitrogen and higher hydrocarbons like ethane and propane. LNG is colorless, odorless, non-corrosive and non-toxic.

## 1.2. Offshore LNG Terminals

Currently the growth of large natural gas fields in offshore areas is explored through advanced technology. Many regasification and liquefaction have been proposed and are under construction in different parts of the world.

An offshore terminal (import or export) is involved in various operations like production, gasification, docking of LNG tankers, loading and offloading operations from tanker and storage. There are different approaches to designing and operating offshore structures. Most of the scenarios for release on water are restricted to structures operating near/on the sea and a brief description of various types of LNG offshore structures (Foss, 2006) is listed below-

### 1.2.1. Fixed Structures

Fixed structures are basically considered for shallow water offshore locations with water depths limited to at most 100 ft. There are three types of fixed structures

1. **Gravity Based Structures (GBS) –** are usually constructed using reinforced concrete and the fabrication is done in a shore based facility. Some of these constructed for LNG operations consider the cryogenic temperatures and the resulting stress on the structure. LNG is usually stored in a double containment tank with membrane lining, which is usually integrated with the GBS.
2. **Offshore Platforms-** non-floating similar to GBS. Currently proposals are being made to develop LNG offshore platforms using existing infrastructure which were originally developed for hydrocarbon production or mining operations. There may or may not be a storage capacity on the platform. In the absence of a storage unit, LNG would be immediately delivered to ships or vaporized to natural gas on the platform and delivered to send out pipelines.
3. **Artificial Offshore Islands –** one of the most novel approaches which offers space for LNG storage, multiple docking berths and other space extensive services and processes which are usually difficult in offshore structures.

### 1.2.2. Floating Structures

Floating structures are basically used in deep water locations involving operations like docking, offloading, storage and regasification. The different types are

1. **Floating Storage and Regasification Unit (FSRU) -** are offshore floating structures where storage and regasification are carried out. The FSRU is a double hulled ship extending 300-400 m long and 70-100 m wide with

several LNG ships shuttling around the FSRU. FSRU's generally require water depth (>160ft) and an anchoring system to facilitate pipeline connection between the FSRU and seafloor. The regasification facilities are mainly located in the main deck and tailored to suit the gas requirements and send-out conditions.

2. **Floating Regasification Unit (FRU) –** an offshore structure where regasification is carried out. Employs conventional offloading arms and allows docking of ships.
3. **Floating LNG (FLNG) -** is an offshore unit which can produce, liquefy, store and transfer LNG. The FLNG facility is moored in the location of natural gas field. The gases are processed to produce LNG or LPG. This is done by treating impurities and liquefaction. The LNG carriers offload the LNG and other products and deliver it to markets. This is different from the conventional alternative where gas is transported via pipelines leading to a shore based facility. Once the gas field gets depleted, the floating LNG is shifted to another gas field. Some of these structures are capable of withstanding severe cyclones.

### 1.3. LNG Marine Operations

The LNG marine operations typical consists of the following processes-

1. **Transportation -** LNG is liquefied and transported through a special type of ship called an LNG carrier

2. **Ship-to-Ship Transfer** – the LNG tankers are moored side-by-side to receive and transfer LNG. The coupling points for LNG transfer are located mid-ship.
3. **Tandem Transfer**– the LNG tankers are moored at the stern of the terminal (tandem) to receive and transfer LNG. The coupling points are located at the bow of the carrier or stern of the terminal.

LNG tankers are double hulled ships that are designed to contain the leak during an incident. There are three types of cargo containment systems (CCS). These are 1) the spherical (Moss) design 2) the membrane design and 3) structural prismatic design.

During an LNG transfer operation, the LNG ship is moored next to the shuttle tanker. The loading crane handles the transfer lines of which some of them transfer LNG from supply vessel to the terminal and some of the lines are used to transfer LNG vapors. The transfer lines consist of vacuum insulated pipe systems which are tailored for cryogenic applications. The transfer lines employ a "pipe in pipe" double containment system which provides optimum thermal insulation properties and advantages in terms of leak detection. LNG is then transferred using pumps continuously through the lines. The offshore offloading process can take typically 40 hours (Martins, de Souza, and Ikeda, 2011). This process takes into account the vessels approaching and departing the ship. The side-by-side operations are equipped with tugs and standby vessels. The transfer lines are well equipped with multiple levels of automation to lower the probability of operational mistakes.

## 1.4. Bow-Tie Model for LNG Releases on Water

A bow-tie diagram was developed and represented in Figure 1 to characterize the causes and consequences of LNG releases on water. The bow-tie has a central top event of LNG release on water. The events to the left of the bow-tie represent causes of the top event. The causes are classified into two categories- basic causes and immediate causes. The basic causes provide the primary root cause of the top event. The immediate causes are secondary causes created due to primary causes. A collision is considered as an immediate cause induced due to undesirable ship maneuvering which is the primary cause of top event occurrence. The events to the right are consequences of the top event and are classified as immediate consequence and ultimate consequences. The immediate consequences often lead to ultimate consequences. An example is that the vapor dispersion can lead to flash fire in the presence of ignition source, where vapor dispersion is the immediate consequence upon top event occurrence and flash fire is the ultimate consequence.

The causes and consequences of the top event consisting of LNG releases on water are adapted from (ABS, 2014) and listed below-

### 1.4.1. Basic Causes

1. Inadvertent disconnection of hoses.
2. Failure of PERC (Powered Emergency Release Coupling).
3. Undesirable ship maneuvering due to human factor issues.
4. Rudder failure during marine transportation or maneuvering.
5. Steering and propulsion failures.

6. Tidal effect causes excessive movement of the vessel and loading arms.
7. Extreme weather scenarios like hurricanes, lightning and tsunamis.
8. Brittle fracture of materials lining the loading lines.

### 1.4.2. Immediate Causes

1. Collisions
    a. Collision of a ship with another ship while maneuvering in the sea/ocean.
    b. Collision of a berthed ship with moving ship close to the berth.
    c. Collision of a LNG ship with the LNG unloading jetty.
    d. Collision of a LNG carrier with the harbor.
    e. Collision of LNG ship with icebergs.
2. Grounding - Grounding of LNG ship on rocks, seabed, waterway side or other similar geographical features.
3. Loss of mechanical integrity of the loading line or flanged connections.
4. Intentional terrorist attacks.
5. Overfilling/over pressuring of fuel tanks of the vessel.

### 1.4.3. Immediate Consequences

1. Pool formation and vapor production.
2. Vapor dispersion.
3. Direct exposure of cryogenic liquid or vapor to personnel.
4. Brittle fractures.

### 1.4.4. Ultimate Consequences

1. Pool Fires.

2. Flash fires.
3. Jet fires (in case of LPG or other pressurized lines).
4. Vapor cloud explosion.
5. Rapid Phase Transition (RPT).
6. Fatality or injury.
7. Loss of assets.

### 1.4.5. Safeguards in an LNG Ship

An LNG ship is equipped with several active and passive safeguards that ensure smooth marine operations. The safeguards are classified into three categories (ABS, 2014)

#### 1.4.5.1. Prevention Safeguards

1. Double containment system for hull and transfer lines.
2. Standardized connections.
3. Sensors for flow measurement, liquid level, temperature and pressure for monitoring and associated alarm systems.
4. Communication between ships and shore.
5. Periodic inspection and testing of equipment.
6. Periodic certification of hoses.
7. Personal Protective Equipment (PPE).
8. Gas, Cold Spill, Fire and Gas Detectors linked to the Terminal Emergency Shutdown System.

9. Control room held in an elevated position, which will be continuously manned during ship berthing and unloading.

#### 1.4.5.2. Prevention and Mitigation Safeguards

1. Controls and/or prohibitions on Simultaneous Operations (SIMOPS).
2. Emergency Shutdown system.
3. Warning signs.
4. Comprehensive bunkering procedures.
5. Restricted vehicle traffic.
6. Accepted ship design and construction standards.

#### 1.4.5.3. Mitigation Safeguards

1. Quick Connect / Disconnect Couplings for transfer lines.
2. Foam Generation Equipment.
3. Powered Emergency Release Couplings (PERC).
4. Dry Powder Fire Extinguishing Systems.
5. Fire Fighting Systems, Deluge and Water Curtains.
6. Global positioning equipment and Global maritime distress systems.
7. Local and vessel emergency response plans.
8. Drip trays.
9. Hazardous Area Classification.

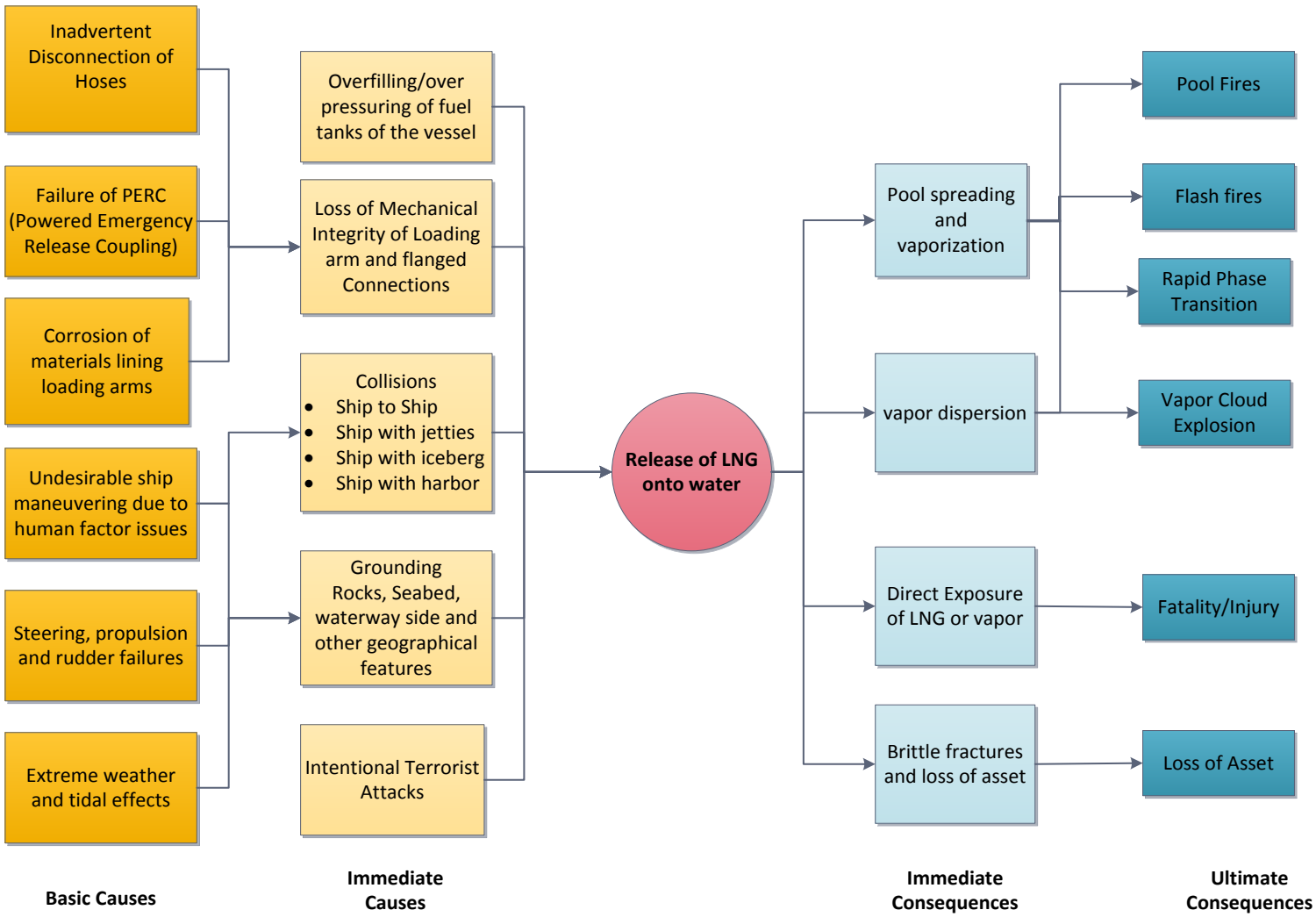


Figure 1. Bow-tie diagram for LNG releases on water showing possible causes and consequences

# CHAPTER II

# RESEARCH FRAMEWORK

## 2.1. Overview of LNG Pool Spreading and Vaporization

An LNG spill can be divided in two stages: source term formation and atmospheric dispersion. The source-term represents the amount of materials released during an incident. The source-term model generally provides a description of the rate of discharge, state of discharge (gas, liquid, and combination of both) and total quantity that is discharged. The source-term phenomenon occurs immediately after release where the behavior of the fluid is influenced by the storage conditions (*e.g.* pressure and temperature) and the release conditions (*e.g.*, geometry and location). Further away from the leak source, as the influence of the source decays, the atmospheric dispersion becomes important (Raj, 1981). The vapors that are produced are dispersed due to the effect of wind in the atmosphere. This is studied as vapor dispersion.

## 2.2. Physics of LNG Release on Water

A failure of a LNG storage vessel can lead to the two phase release consisting of vapor and liquid (Cavanaugh, Siegell, and Steinberg, 1994). Following the release, small droplets vaporize immediately and large liquid droplets collect together to form a pool. As LNG is lighter and immiscible in water, the liquid pool will spread over the water surface rapidly. As the inventory of LNG increases in the pool, the equilibrium due to gravity pushes the pool to increase in diameter and thereby its area. This spreading process is simultaneously accompanied by rapid vaporization of the inventory. The pool spreading and vaporization leads to a change in temperature difference between water

and LNG due to complex heat transfer that occurs in the form of rapid boiling and subsequent vaporization. The rapid boiling in the spreading pool adds a significant amount of turbulence which is characterized by the formation of bubbles on the pool surface. As the pool continues to spread, the thickness of the pool reaches a minimum value and the radius reaches a maximum value. At this stage the liquid pool attains equilibrium and the pool tends to regress due to vaporization. When the release is on confined water, the heat transfer process is further complicated by the formation of ice during the spreading. This phenomenon is illustrated in Figure 2.

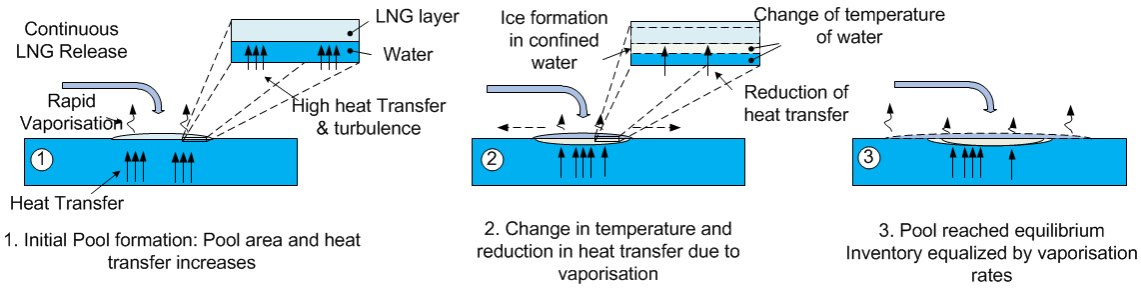


Figure 2. Physics of LNG release on water

## 2.3. Key Parameters Affecting Pool Spreading and Vaporization

The key parameters affecting the pool spreading and vaporization phenomenon was studied by analyzing the experimental datasets from literature and LNG experiments performed at the Mary Kay O'Connor Process Safety Center (Gopalaswami, Mentzer, and Mannan, 2015). They are –

### 2.3.1. Heat Flux from Water to LNG Pool

The heat flux from water to the LNG pool is dominated by the convection phenomena. The convective boiling of cryogenic liquid on water exhibits a special immiscible liquid-liquid heat transfer phenomenon where heat transfer parameters change rapidly in a short duration of time. The convective boiling of LNG over water is influenced by different physical and chemical properties of the components present in LNG and the hydrodynamic phenomena that are influencing the boiling process (Gopalaswami, Mentzer, and Mannan, 2015). The boiling process starts in the film boiling regime owing to the large temperature difference between water and cryogenic liquid. The boiling process on water is different from boiling on a solid substrate for various reasons. One of the significant differences is the ability of LNG to pick up water droplets from its surface (Boyle and Kneebone, 1973a). Furthermore, there is also an absence of nucleation sites on the surface of water unlike in a solid substrate. When LNG contacts water, the temperature difference is more than what is required for film boiling and this leads to superheating. The superheating leads to the formation of small bubbles instantaneously by flashing. This process is called homogeneous nucleation. This is different from heterogeneous nucleation in boiling on a solid substrate where nucleation takes place due to irregularities on the surface. It is important to determine the temperature difference and heat transfer coefficient at every instant to determine the heat flux from water to LNG dynamically.

### 2.3.2. Heat Flux from Ice to LNG Pool

The LNG ship passes through different water bodies of which some are completely water and some are ice borne water. Special ships called ice class carriers are used to navigate ice borne waters. One of the LNG incident scenarios is the collision of an LNG carrier on an iceberg during marine transportation. A collision can result in damages to the vessel and lead to the leakage of the contents on ice or an ice-water mixture. When cryogenic liquid comes in contact with ice, it undergoes rapid vaporization due to the difference in temperature between the ice and cryogenic liquid (Gopalaswami, Vechot, Olewski, and Mannan, 2015). This process is different from the heat transfer between water and cryogenic liquid as ice is a solid and thus heat transfer to the pool occurs primarily through conduction**.** The ice is generally present in a temperature that is greater than LNG. Hence heat is transferred from ice to LNG. This leads to cooling down of ice to a temperature lower than its original temperature before the spill. Very few experiments were performed by releasing cryogenic liquids on ice. It is important to determine the amount of heat lost by ice when LNG is spilled on ice borne environment.

### 2.3.3. Turbulence in the Cryogenic Liquid Pool

When LNG is released on water, the turbulence is generated due to vertical velocity of the gas traversing through the pool due to rapid vaporization. Several effects like variations in temperature can cause variations in fluid density, surface tension and viscosity. These factors can have a profound influence on the heat transfer taking place between LNG and water. One such effect in fluids with variable density is the generation

of convection currents within the cryogenic liquid. The fluid regions with turbulence produce convection currents and interact with convection currents radiated from other regions. Turbulence can be produced locally by the breaking of thermal convection currents. This in turn can add to the mean turbulent flow through increased momentum and energy. These waves are called ‘thermal plumes’ and are believed to be important in heat transfer between water and cryogenic liquid like LNG.

These two factors with high priority, the heat flux from substrate and the turbulence in the pool, are the focus of this research study as they have significant influence in the mass, momentum and energy transfer taking place in the cryogenic pool. These parameters tend to directly influence the cloud formation and thereby the safety impact resulting from it. Others parameters were identified to be the effect of waves when LNG is released on unconfined water bodies like seas and oceans. The study of this factor is extensive and is beyond the scope of this study.

## 2.4. Problem Statement

With the rapid development of floating offshore structures like FLNG, there is an increase in the number of LNG marine operations. When LNG is released on water, a spreading liquid can form a pool with rapid vaporization, leading to the formation of a flammable vapor cloud. Safety analysis in the LNG industry involves a thorough evaluation of potential consequence of incidental releases and the risk imposed by such events to the public. A thorough analysis of consequence resulting from LNG release on water is performed here. The consequence analysis of the hazards resulting from a real or hypothetical release of LNG on water requires data on the vaporization rate (source-

term) as this serves as an important input parameter for performing vapor dispersion modeling. A better understanding of the phenomena occurring upon LNG spillage onto water by taking into account the different factors influencing it is currently needed to develop better source-term models. The improvement in the vaporization rate estimation and turbulence quantification will reduce the uncertainties in the results obtained from source dispersion modeling. To date, there does not appear to have been any established experimental methods or three-dimensional CFD code for LNG pool spreading and vaporization in the literature. In addition to above, a time variant and scale independent heat transfer model for LNG vaporization is yet to be implemented in modeling. The challenge is to close the gaps in the state of understanding and to identify, quantify and study the impact of different factors that aid in efficient analysis of determining source-terms.

### 2.5. Significance

The source-term (vaporization rate) includes the physical description of the LNG pool to simulate the gas phase generation. The extent of hazard depends strongly on this source strength (quantity), pool size and variation of source-term with respect to time. It is thus important to determine this as accurately as possible. Additionally, a precise modeling of the source-term can improve the accuracy of the vapor dispersion modeling, which supports decision making in facility-siting.

Currently vaporization rates with respect to time are required for determining the time to leak detection, isolation and blow-down time of particular process equipment in an LNG facility.

Source-term is also used to determine the Ductile to Brittle Temperature Transistion (DTBTT). This helps in determining the capacity of structures for LNG exposure. Mitigation measures and emergency response planning is based on the rate of vapor cloud formation and this will help in implementing safety measures around areas with LNG operations. Additionally, estimation of vaporization rates aids in inherent safety practices through proper design and integrity for prevention against hazards. Source term modeling can also improve marine facility siting techniques like ship to ship spacing that will prevent or cause less damage during ship to ship collisions, ship to shore collisions and credible terror attacks. Finally, the source-term estimation is also performed to comply with regulations.

## 2.6. Objectives

The research work primarily focuses on the potential use of a Computational Fluid Dynamics (CFD) model for simulating the LNG pool spreading and vaporization behavior. The objectives of the research are to:

1. Understand the current state of LNG pool spreading and vaporization modeling and identify gaps in this modeling through a literature review.
2. Identify key parameters influencing the LNG pool spreading and vaporization phenomena through analysis of existing data.
3. Establish experimental determination methods for measuring the pool spreading parameters and vaporization rates.

4. Quantify the key parameters through small-scale experiments and models. The results and techniques employed will serve as sub-models for the pool spreading and vaporization model.
5. Develop a methodology in CFD to simulate the pool spreading and vaporization phenomena through a CFD model and validate the CFD model with LNG experiments for specific scenario of LNG leak on water.
6. Provide recommendations for improving emergency response based upon the research results.

## 2.7. Methodology

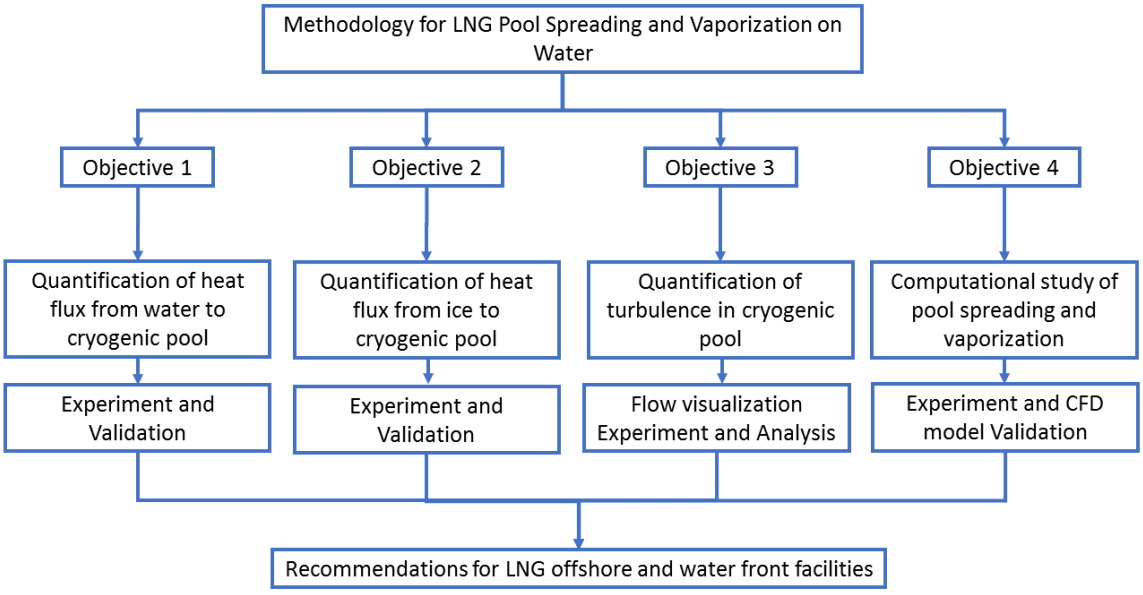


Figure 3. Research methodology

The main objective of the research is to advance the status of LNG source-term modeling through experiments and CFD. In addition, the parameters which influence the

pool spreading and vaporization are studied and implemented as sub-models in the CFD methodology. The methodology for current research is shown in Figure 3. The methodology is explained with respect to organization of the dissertation. The dissertation is organized to meet these objectives. The dissertation is structured into eight chapters. Chapter I provides an introduction to the LNG industry and focuses on the LNG offshore facilities. The LNG marine operations, existing safe-guards and potential incident scenarios of an LNG leak on water are discussed. Chapter II gives an overview of source-term modeling and physics involved in LNG release on water. Problem statement, motivation and significance of research are discussed here. The chapter III provides a review of the experimental datasets for LNG spills on water. In addition to it, models developed for LNG pool spreading and vaporization are discussed with its advantages and disadvantages. Chapter IV covers objective 1 of this research. The quantification of heat flux from water to cryogenic liquid pool is studied through small-scale experiment. A model for predicting the heat transfer coefficient during vaporization is validated against experiment. This model is implemented as sub-model for heat transfer in CFD methodology. Chapter V covers objective 2 of this research. The quantification of heat flux from ice to cryogenic liquid pool is studied through small-scale experiment. The one dimensional conduction model is validated against experiment. A case study is undertaken to determine the vaporization mass flux of LNG on ice. Chapter VI covers objective 3 of this research. The turbulence present in the cryogenic pool due to vaporization is studied through flow visualization experiment. The turbulence parameters obtained as a result from this study serves as input to the main

pool spreading and vaporization model. Chapter VII covers objective 4 of this research. A methodology in CFD for pool spreading and vaporization is developed. The implementation of the turbulence and vaporization model is performed and the resulting vaporization rate (source-term) is studied. An LNG experiment is performed to simulate an incidental leak during loading operations and the CFD model is validated with the experiment. The chapter VIII includes conclusions based on the research performed. Recommendations based on the research and topics for future research are provided.

# CHAPTER III

# LITERATURE REVIEW

In this chapter, a detailed literature review of the mathematical models and experiments for pool spreading and vaporization are detailed in the subsequent sections. The literature review initially discusses all the experiments performed by governmental agencies and private institutions for LNG releases on water. The review of mathematical models considers the models that have been developed in the past for pool spreading and vaporization phenomenon. A literature survey was also performed by UK Health and Safety Executive and was published as a guidance document (Webber, Gant, Ivings, and Jagger, 2010).

## 3.1. Review of Experiment

### 3.1.1. Bureau of Mines Test

An investigation of the release of LNG onto water was studied in 1972 by Bureau of Mines (Burgess, Murphy, and Zabetakis, 1970). About 2,000 gallons of LNG were consumed in various tests. All these spills were instantaneous. Small-scale explosions were observed when LNG was released on water. Small-scale tests were performed to study the vaporization rate of LNG and large-scale tests were performed to study the vapor dispersion behavior. The downwind distances of flammable cloud was determined for large-scale tests. The first report drew conclusions on the pool diameter, vaporization rate, gas dispersion, heat transfer, and explosion hazard. The conclusions of this report led to another series of tests that were performed by the Bureau of Mines. The report came out in 1972 (Burgess, Biordi, and Murphy, 1972). In these tests, about

12,000 gallons of LNG were released. LNG came from two different sources with different compositions of hydrocarbon. The main objectives of these tests were to study physical explosions called rapid phase transitions in order to understand their mechanism and also to study the atmospheric dispersion of natural gas with ignition.

### 3.1.2. Esso Tests

Tests were conducted in two spill sizes of 250 gallons and 2,500 gallons (May, McQueen, and Whipp, 1973). A total of 17 spills were carried out in varying weather conditions. The experiment was focused on capturing the parameters required for determining the exclusion distance. The LNG was pumped rapidly at 5,000 gpm, making it an instantaneous release. The vaporization rate with respect to time was calculated, and it was consistent with Burgess *et al* (1970). An average vaporization rate was also determined when the pool size attained a constant value. The study attempted to correlate the minimum pool thickness with pool diameter. It was estimated to be between 5-8 mm and a minimum pool thickness of less than 5 mm was used in pool models.

### 3.1.3. Shell Tests at Thornton Research Center

A series of lab-scale and small-scale tests were conducted by Shell for American Petroleum Institute (API) in 1973 (Boyle and Kneebone, 1973b). The study had classified spills as steady-state, instantaneous and intermediate source conditions. Laboratory and small-scale tests were performed to study the rate of LNG vaporization, rate of spreading, water pick-up, ice formation on the water surface, and the dispersion

of cold vapor in wind tunnels for LNG spills on water. A parametric analysis was also performed for the calculated parameters.

### 3.1.4. Maplin Sands

LNG tests were conducted by the National Maritime Institute at Maplin Sands, England. The test was initiated by Shell (Puttock, Blackmore, and Colenbrander, 1982). The tests were conducted to study the dispersion and thermal radiation behavior of LNG and liquid propane releases on water. A total of twenty-four continuous and ten instantaneous spills were conducted. The wind speed varied from 3.8-8.1 m/s during the tests. A barge was unloaded rapidly to create an instantaneous release. The instantaneous spill sizes varied from 5–20$m^3$. The release rates for continuous spills varied from spill 0.025- 0.067 $m^3$/s. The entire spill area was surrounded by a dike of diameter 300m. The maximum extent of the pool was around 10m and the pool was observed to regress at $2\times10^{-4}$ m/s. The average vaporization rate was determined to be 0.085 kg/$m^2$s.

### 3.1.5. Burro Series

The Burro series was conducted by Lawrence Livermore National Laboratories (LLNL) under the sponsorship of the Department of Energy (DOE) (Koopman *et al.*, 1982).The Burro series was a part of liquefied gaseous spills developed to study the pool spreading, vaporization, dispersion, ignition, combustion, explosion, and damage effects. A series of eight experiments was conducted to determine the vapor dispersion behavior of LNG released on water. The spill volume ranged from 24 to 39 $m^3$, the spill rate from 11.3 to 18.4 $m^3$/min, the wind speed from 1.8 to 9.1 m/s and atmospheric stability ranging from unstable to slightly stable. Multiple parameters like wind speed, wind

direction, gas concentration, temperature, humidity and heat flux from the ground were measured at different distances from the spill point and at different elevations. The experiment was recorded using cameras and IR imagers. LNG was found to boil preferentially during the test. A rapid phase transition also occurred and data was recorded. The vaporization rate was determined by calculating the amount of gas passing through an arc of gas sensors. The concentrations were integrated over time and total spill amount to obtain the vaporization rate. This was also used to determine the adequacy of coverage of the sensors in their locations.

### 3.1.6. MKOPSC LNG Datasets

In 2005, British Petroleum (BP) contracted the Mary Kay O'Connor Process Safety Center for the "LNG Vapor Cloud Control and Mitigation Research Program". The project focused on detection, control, suppression of LNG vapor and fire. From 2005 to 2009 LNG experiments were conducted by Mary Kay O' Connor Process Safety Center at the Brayton Fire Training Field. A series of tests were conducted in November 2007 to understand LNG vapor cloud dispersion behavior and to measure the effectiveness of water curtain and high expansion foam on mitigating LNG vapor fires. A total of eight tests named TEEX1- TEEX8 were performed during the experiment. The TEEX1 and TEEX2 vapor dispersion tests for release of LNG on water is considered in this study. A summary of experiments is given in Table 1.

Table 1. Summary of experiments from literature

| No | Reference | Test Name | Spill Size ($m^3$) | Pool Diameter (m) | Pool Thickness (m) | Spreading Rate (m/s) | Vaporization mass flux ($kg/m^2s$) |
|---|---|---|---|---|---|---|---|
| **1** | (Burgess, Murphy, and Zabetakis, 1970) | U.S Bureau of Mines | 0.0055-0.36 | 0.5-12.1 | 0.03 | 0.76 | 0.156-0.181 |
| **2** | (May W.G. et al., 1973) | Esso Test | 0.8-10.8 | 29.2 | NA | 1.2 | 0.195 |
| **3** | (Boyle and Kneebone, 1973b) | Shell Lab Test | 0.02-0.085 | 4- 7.3 | 0.0018 | 0.76 | 0.195 |
| **4** | (Koopman *et al.*, 1982) | Burro Series | 24-39 | 8.0-10 | NA | NA | ~0.195 |
| **5** | (Puttock *et al.*, 1982) | Maplin Sands | 5.0-20 | 20 | NA | NA | 0.085 |
| **6** | (Cormier, Qi, Yun, Zhang, and Mannan, 2009) | MKOPSC TEEX Test | 3.26-7.5 | 6- 6.6 | 0.0019 | 0.76-0.84 | 0.191 |

Accurate data for pool spreading and vaporization is currently limited. The most comprehensive experiments are carried out primarily to understand vapor dispersion and these have certain uncertainties in the measurements and models that are used to determine the source-term. This is due to difficulties in direct measurement of the vaporization rates or pool spreading parameters like pool height, pool radius and spreading rate. In the literature survey of experiments, it is noted that there is no well-established method to determine the pool spreading parameters. The vaporization rate in LNG experiments is determined through one of three methods. The first method is the measure of the loss of LNG mass that is occurring due to vaporization (Boyle and Kneebone, 1973b). The vaporization rate is obtained by determining the slope of mass loss data. This method has been applied widely in small-scale experiments. The second method is to measure the temperature of water during the experiment and to apply empirical correlations on heat transfer mechanisms like convective boiling or conduction to obtain the vaporization rate (Burgess *et al.*, 1970). This method has been widely used in small and medium-scale LNG tests. The third method is to determine the rate of flow of vapor through an array of gas sensors. The vaporization rate is determined by integrating the measured concentration data across the area covered by gas sensors. This method has been widely used in large-scale LNG experiments like the Esso tests (May W.G. et al., 1973). It is important to note that current understanding of LNG spills over water is conservative, where an average value of vaporization rate is used although, it is a transient parameter that can change with time. Such models involving an average

vaporization rate lack experimental validation in the analyses that have a direct influence on the exclusion zones.

## 3.2. Review of Models

### 3.2.1. Phenomenological Models

The phenomenological models provide a hypothesized relationship between the variables influencing a phenomenon, where the relationship seeks best to describe the phenomenon. The LNG pool spreading on water relations were developed based on movement of oil slicks in the sea. Many researchers (Otterman, 1975); (Fay, 2007); (Raj, 1981); (Opschoor, 1977); (Briscoe and Shaw, 1980); (Webber, 1991); (Waite, Whitehouse, Wakbham, and Winn, 1983); (Dodge, Park, Buckingham, and Magott, 1983) developed relationships based on forces acting on the pool. Each of the relations developed varied in the forces that were taken into account to develop the pool spreading parameters, namely pool radius, pool height, and spreading rate. The vaporization relations were developed from the various heat inputs to the pool. A synopsis of the phenomenological models is given below.

#### 3.2.1.1. Pool Spreading

The spreading process is usually associated with three regimes and in each regime; two opposing forces are involved. The forces acting on the pool is shown schematically in Figure 4.

**1. Gravity – Inertia**

Initially the pool is relatively thick and the dominant phenomenon is the head of the spilled fluid causing the pool to accelerate radially. The gravity force opposes the inertia of the pool (which is related to its mass).

**2. Gravity – Viscous**

As the pool becomes thinner and the spreading slows down, the viscous drag of the substrate on the pool becomes significant. The gravity force is opposed by the frictional drag force.

**3. Surface Tension - Viscous**

At some point the pool becomes so thin that gravitational forces become negligible and the relatively small interfacial tension at the periphery of the pool becomes significant. The net surface tension force tending to spread the pool is opposed by the frictional drag force. A change from gravity-inertia to gravity viscous occurs when the viscous forces are greater than the gravitational force. Similarly a change from gravity-viscous regime to surface tension-viscous regime can occur when the surface tension forces are larger than viscous forces.

The gravitational force acts downward. This leads to an unbalanced pressure distribution in the pool. This phenomenon causes it to push the pool radially outward. The force on a liquid pool acts in the direction of decreasing pool thickness. As a result of this, the gravitational force decreases as the pool area increases and the pool height reduces. The gravitational force ($F_G$) acts horizontally causing the pool to spread radially outward and is given by Briscoe and Shaw, (1980)

$$F_G = \pi\rho g\delta R\left(1 - \frac{\rho}{\rho_w}\right) \quad (1)$$

The driving forces for pool spreading are balanced out by the inertial force. This inertial force ($F_I$) of the liquid is expressed as

$$F_I = -\rho\pi R^2 h.\frac{d^2R}{dt^2} \quad (2)$$

The radial movement of LNG is opposed by retarding viscous forces ($F_V$) which represent the frictional drag offered by water to spreading LNG. It is expressed as a product of viscous shear stress and the area.

$$F_V = \frac{dR}{dt}.\sqrt{\frac{\rho_w\mu_w}{t}}(\pi R^2) \quad (3)$$

After spreading for some time the thickness of the pool reaches a minimum value and gravitational forces become negligible and the relatively small interfacial tension at the periphery of the pool becomes significant. However, a surface-tension driven regime of pool spreading is never reached. The spills will stop spreading when the pool thickness reaches a minimum value or the pool breaks down to smaller pools.

The surface tension force ($F_{ST}$) is given by the product of surface tension coefficient and circumference of the pool in which the force is acting on.

$$F_{ST} = 2\pi R\sigma \quad (4)$$

#### 3.2.1.2. Vaporization

The heat input to the pool is comprised of three components: convective heat from water, convective heat from air and radiation from the sun.

The heat input from water to LNG in the form of convection is given by

$$Q_{con} = h_w\pi R^2 h_w(\Delta T) \quad (5)$$

There are three regimes possible: nucleate boiling, film boiling and transition boiling. LNG predominantly film boils on water. The convective heat from water is a transient quantity due to the rapid change taking place due to boiling. The heat transfer coefficient is determined from correlations and it changes for each boiling regime. As the temperature difference between LNG and water is reduced, the heat flux associated with it also changes and the amount of LNG vaporized changes with it.

The convective heat input from air above the pool is given by

$$Q_a = h_a \pi R^2 (T_a - T_L) \tag{6}$$

The heat input due to solar radiation to the pool is given by

$$Q_{rad} = q_{rad} \pi R^2 \tag{7}$$

The total heat input to the pool is given by the sum of all other heat inputs, as depicted in Figure 4 below.

$$Q = Q_a + Q_{con} + Q_{rad} \tag{8}$$

The mass evaporated is determined from heat of vaporization and energy balance. LNG vaporization rates are estimated from

$$M_{vap} = \frac{Q\ \Delta t}{\Delta H_v} \tag{9}$$

where $\Delta t = t_{i-1} - t_i$ (10)

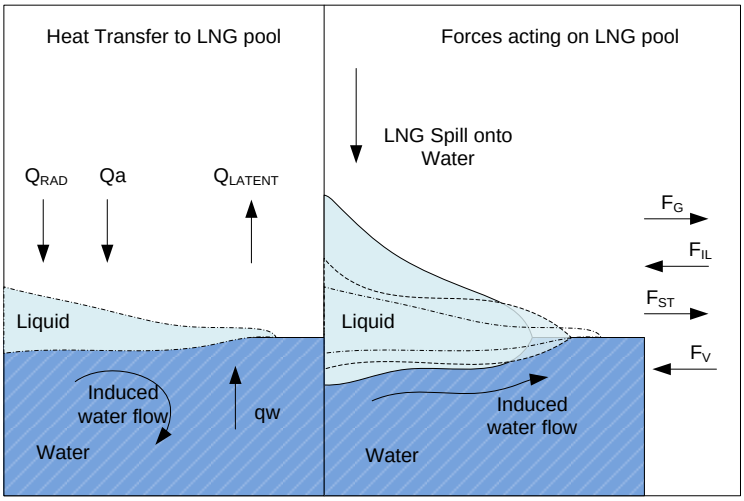


Figure 4. Schematic of heat transfer and forces acting on the LNG pool adapted and redrawn from Briscoe and Shaw, (1980)

#### 3.2.1.3. Advantages

The phenomenological models provide the basis to relate the variables influencing the pool spreading behavior. Pool spreading and vaporization behavior is treated separately allowing models to be used for non-vaporizing spills too.

#### 3.2.1.4. Disadvantages

Complex phenomenon like hydraulic jump, turbulence, flashing, and jetting, scenarios involving geometry cannot be modeled.

### 3.2.2. Integral Models

An integral model calculates the dynamic behavior of pool spreading and vaporization through mass and energy balances. Software like PHAST (DNV (Det Norske Veritas), 2012) , SOURCE5 (Atallah, Sirdesai, and Jennings, 1993) and SAFESITE3G (Baker Engineering and Risk Consultants, 2005) use this methodology for

this physics. Correlations for continuous and instantaneous releases of LNG on water were developed. A pool is usually idealized to be a circular cylinder of particular radius and uniform thickness. A mass conservation equation consists of mass that is continuously added to the pool and the mass evaporated from the pool. This is given by

$$\frac{dM}{dt} = \dot{M} - M_{evap} \tag{11}$$

where $\dot{M}$ is rate at which mass is added to the pool and $M_{evap}$ represents the rate of mass evaporated from the pool. The term $\frac{dM}{dt}$ is assumed to be zero for instantaneous spills.

For spills of finite duration, the mass of fluid released is integrated over the finite time interval given by

$$M_{pool}(t) = \int_0^t m(t).dt = m_{ave}\Delta t \tag{12}$$

where $m_{ave}$ is the average rate of mass discharged in the pool for a finite duration $t$.

The pool spreading equations are developed in a manner similar to phenomenological models. However, time varying variable is included in the equations. For continuous releases, the pool stopping condition is based on mass balance or force balance. When a mass balance is adopted, the pool stops spreading when the mass released is equalized by the mass evaporated. For a force balance based approach, the pool stops spreading if the pool thickness reaches a minimum value. The minimum pool thickness should never be less than the value limited by the surface tension and is usually of the order of 1 mm for water substrates.

The integral models vary based on the assumptions made for spreading rate, heat transfer models used for vaporization, release types (continuous vs instantaneous) and the numerical technique used for solving the equations.

#### 3.2.2.1. Advantages

A time-based analysis for instantaneous, continuous and semi-continuous spills can be performed using integral models. The models are reasonably accurate and have been validated for many LNG experiments.

#### 3.2.2.2. Disadvantages

Complex phenomenon like hydraulic jump, turbulence, flashing and jetting, rapid phase transition, and scenarios involving geometry cannot be modeled. The integral models assume a constant thickness along its length and it is invariant with time. However, the height of the pool can vary with respect to location and time.

### 3.2.3. Shallow Water Equations

Pool spreading equations based on Shallow Water Theory were initially provided by Fannelop and Waldman (1972). Several other models based on Shallow Water Theory implemented in CFD were given by (Webber and Ivings, 2010). The Shallow Water Theory describes the pool behavior in terms of horizontal components and scalar depth field. The shallow water equations are a set of partial differential equations where pool velocity and height are dependent variables and spatial coordinate r and time t are independent variables. The equations do not take into account the variation of transport properties with respect to elevations and this can happen when the pool is shallow.

The mass conservation (13) and momentum conservation equations (14), (15) for a symmetric circular pool are given by:

$$\frac{\partial(h)}{\partial t} + \frac{1}{r}\frac{\partial(rhu)}{\partial r} = 0 \tag{13}$$

$$\frac{\partial(hu)}{\partial t} + \frac{1}{r}\frac{\partial(rhu^2)}{\partial r} = -\frac{g}{2}\frac{\partial h^2}{\partial r} \tag{14}$$

$$g^* = g(1 - \frac{\rho}{\rho_w}) \tag{15}$$

#### 3.2.3.1. Advantages

The Shallow Water Equations provide a useful idealization of pool spreading behavior that closely resembles the physics. Phenomenon like hydraulic jumps and channel flows can be modeled easily.

#### 3.2.3.2. Disadvantages

When LNG is released on water, a part of it submerges and pushes the water outward at the front of the spreading pool. This is called front resistance and is difficult to model accurately in shallow water theory if water is modeled as wall. A three dimensional solver is required to implement the turbulence models, and since shallow water equations are two dimensional, turbulent convection taking place in LNG cannot be modeled. Additionally, including the vaporization phenomenon in the mass balance equation and friction in the momentum equation in the shallow water equations poses significant difficulty. An alternate method is to apply CFD to solve the shallow water equations. This was implemented in both FLACS (Melheim, Ichard, and Pontiggia, 2009) and SPLOT (Ivings and Webber, 2007) software.

A modified Shallow Water Equations with mass conservation (16) and momentum conservation equation (14) including the vaporization and friction effects are given by:

- $\frac{\partial(h)}{\partial t} + \frac{\partial(hU)}{\partial r} = \frac{(\dot{M} - M_{evap})}{\rho_l}$ (16)
- $\frac{\partial u_i}{\partial t} + \frac{u_j \partial u_i}{\partial x_j} = F_G, i + F_\tau, i$ (17)
- $F_G, i = g\left(1 - \frac{\rho}{\rho_w}\right)\left(\frac{\partial(h+z)}{\partial x_i}\right)$ (18)
- $F_\tau, i = \frac{1}{2} f_f u_i |u|$ (19)
- $f_f = \left(\log\left(\frac{h}{3.7\epsilon_g}\right)\right)^{-2}$ (20)

where $F_G$ is the gravitational force, $F_\tau$ is the shear stress, $f_f$ is the friction factor and $\epsilon_g$ is the roughness factor.

### 3.2.4. CFD Models

A recent improvement in modeling is the use of CFD for pool spreading and vaporization. Most CFD models are based on the Reynolds-Averaged Navier-Stokes (RANS) equations that describe fluid flow. Modern CFD codes use a CAD-like front-end to generate the geometry. CFD simulations can take from a few hours to many days or weeks to run depending on the complexity of the scenario and the number of cells used within the computational mesh.

The general purpose CFD codes provide a range of sub-models for turbulence, multiphase flow, and flexibility in modeling releases of different sizes. Many shortcomings of other models are overcome by CFD models.

#### 3.2.4.1. Advantages

CFD involves the numerical solution to the 3-dimensional time-dependent fluid flow equations and is advantageous in that the variations of transport properties in all three cartesian coordinates can be modeled. One such example is the bund over-filling; when LNG fills the bund, the height of LNG in the bund increases and becomes comparable to length and breadth of the pool. Such scenarios are handled well by CFD when compared to other type of models. CFD also has the capability to model convective turbulence through turbulence models. There is also a variety of turbulence models to model various kinds of turbulence. The CFD modeling approach allows for the representation of complex geometry like a sloped trench and its effects on multiphase flow. CFD provides an advantage of modeling site specific hazards like the space between an onshore platform and a marine carrier.

#### 3.2.4.2. Disadvantages

The main disadvantage of CFD approaches for LNG pool spreading is that they are generally complex, costly and time-consuming. Usually a fine mesh is required to capture the interface characteristics and large-scale spill scenarios involving a large domain with millions of cells. This becomes computationally expensive.

A summary of models used for pool spreading and vaporization is provided Figure 5

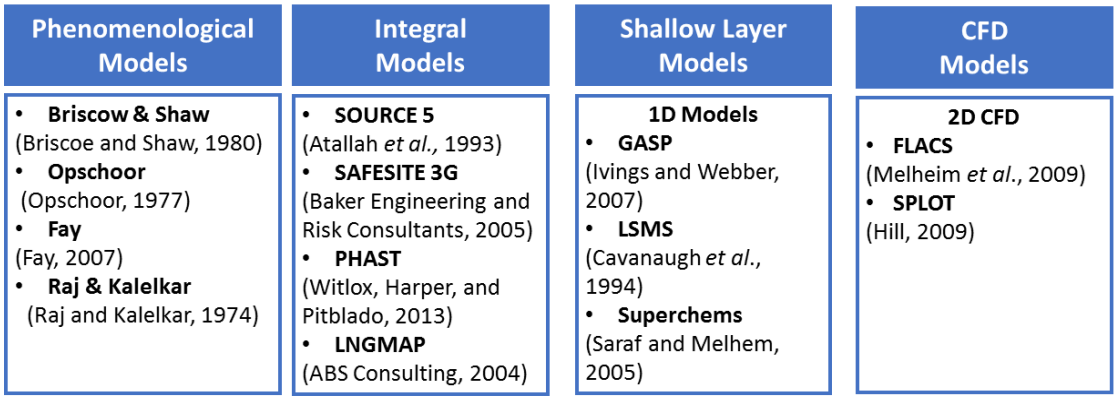


Figure 5. Summary of models

### 3.3. Gap Assessment

Currently there is no established method for experimental determination of vaporization rate and pool parameters like pool diameter, pool height, and spreading rate. This is due to experimental difficulties like vapor blocking that occur during the experiment. Additionally, a single average value for vaporization rate is used instead of a transient vaporization rate. The vaporization rate is a transient quantity and it changes with time due to change in heat input to the pool.

Currently there is a need for a 3-D CFD model for pool spreading and vaporization. A 3-D CFD model will involve a multiphase model where the liquid and vapor phases of LNG can be tracked simultaneously. A 3-D CFD is useful in complex scenarios like LNG flow in sloped trenches and bund overtopping. A transient vaporization rate obtained from a multiphase simulation will also eliminate the need for links between source-term modeling and vapor dispersion as vapor is produced dynamically by this method. While modeling in CFD, knowledge on turbulence is

required. In this physics, turbulence plays an important role in heat transfer and currently the turbulence parameters like intensity, kinetic energy, and eddy dissipation rate are assumed and there are no bench mark experiments to explain the causes of turbulence or magnitude of these parameters.

There are certain uncertainties arising in both experiments and modeling. This is due to the two phase nature of LNG which can affect instrumentation and modeling approaches. An attempt to capture the uncertainties in both experiments and modeling is performed in each step of this research. Knowledge on uncertainties is required for designing statistical performance measures specifically for source-term modeling.

### 3.4. Summary

In this chapter, the predictive models and the experiments for LNG pool spreading and vaporization phenomenon were reviewed. The gaps present in this research were highlighted. Methods for capturing the pool spreading parameters and vaporization parameters were reviewed. The limited availability of turbulence information and experimental data for evaluating CFD models was noted. The lack of proper 3-D CFD model for LNG pool spreading and vaporization was highlighted.

# CHAPTER IV

# QUANTIFICATION OF HEAT FLUX FROM WATER TO CRYOGENIC POOL[1]

## 4.1. Introduction

The hazards associated with spills of Liquefied Natural Gas (LNG) on water are a cause for concern as its vapors are flammable. The flammable vapors can cause hazards near the leak source or distances away from the leak source, if dispersion is strong. The rate at which vapor is generated largely depends on the rate of heat transfer from water to cryogenic liquid. The evaluation of consequences resulting from an incidental spill of LNG on water involves proper determination of this rate at which flammable hydrocarbon vapor is produced.

As a part of safety evaluations, many experiments were specifically performed to determine the vaporization fluxes of LNG on water ((Ali, Drake, and Reid, 1975; Burgess *et al.*, 1970; Drake, Jeje, and Reid, 1975a; Jeje, 1974; Nakanishi and Reid, 1971)). Accurate data for vaporization is currently limited. The most comprehensive experiments that were carried out were primarily to understand vapor dispersion behavior (Koopman *et al.*, 1982), (Cormier *et al*., 2009), (Qi, Ng, Cormier, and Mannan, 2010). In all these experiments the source- term was calculated by measuring the heat flux through mass loss or water temperature. The first method involved the measure of the loss of LNG mass that was occurring due to vaporization (Drake *et al*., 1975a),

[1] Reprinted with permission from "Small-scale experimental study of vaporization flux of liquid nitrogen released on water" by Gopalaswami, N., Olewski, T., Véchot, L. N., & Mannan, M. S., Journal of Hazardous Materials, Copyright [2015], Elsevier

(Nakanishi and Reid, 1971), (Boyle and Kneebone, 1973b). The vaporization flux was obtained by determining the slope of mass loss data with respect to the cryogenic pool area. The second method was to measure the temperature of water during the experiment and to apply empirical correlations on heat transfer mechanisms like convective boiling or conduction to obtain the vaporization flux (Burgess *et al.*, 1970). Both these methods had been applied widely in small-scale experiments and are being considered in the current study. These two methods are used here to establish a suitable procedure to determine the vaporization flux of cryogenic liquids boiling on water. It is also noted that most of these experiments are instantaneous in nature, with a lack of bulk water and surface water temperature values that are necessary for heat flux calculations. These instantaneous spills also lack information on the variation of the vaporization flux with respect to time, which is important in determining the time at which the vaporization flux becomes constant. Moreover, only average values of vaporization flux are reported in most of the experiments and a time-dependent vaporization flux is reported only in few experiments (Drake *et al.*, 1975a), (Nakanishi and Reid, 1971), (Boyle and Kneebone, 1973b). In addition to these, the tests which reported the time dependent behavior were performed in small boiling cells. The results of these small-scale experiments are difficult to scale up, as the bulk water in small confined space of the cell cools down very rapidly. As a result of this, the vapor film breaks quickly, as the temperature difference is not sufficient to maintain a film boiling regime. The size of the water body is also different in all experiments, which resulted in a different amount of reduction in water temperature. The scale up of small-scale data to large releases of LNG

involves the analysis of factors that will reflect these issues. Several theoretical correlations were also developed by many researchers and it is important to note that these were originally developed for boiling on a solid surface and seemed to under-predict the heat flux values and hence the vaporization fluxes for water substrate (Drake *et al.*, 1975a), (Drake, Jeje, and Reid, 1975b).

## 4.2. Objective

The main objective of this phase of the study is to investigate the convective boiling model for transfer of heat from water to cryogenic liquid through small-scale experiments. The experimental study is to aid in accurate prediction of heat fluxes and vaporization rates over a range of experimental data. A continuous spill of liquid nitrogen reflecting a spill of LNG on water is studied. The study is also performed to independently validate the vaporization model for cryogenic liquid boiling on water and verify the film boiling regimes of cryogenic liquids boiling on water. In doing this, the source-term is obtained by mass and temperature measurement. Convective boiling models with modified coefficient are applied to address the effect of water as a substrate for boiling. The study provides a basis for predicting the heat flux from water to cryogenic liquids for source-term modeling. The vaporization model can be coupled with pool spreading dynamics to model the cryogenic pool spreading and vaporization on water.

## 4.3. Experimental Setup and Procedure

The experimental setup designed for small-scale spills of liquid nitrogen on water is shown in Figure 6. Liquid nitrogen was used as a safe analog to LNG. The setup

consisted of a metallic cylinder with an inner diameter of 58.5 cm and a height 87.5 cm made of carbon steel. A stainless steel chimney with dimensions of 35X35X80 cm was placed inside the metal cylinder to protect it from cryogenic fractures. The stainless steel chimney was square shaped in cross section and was devoid of top and bottom covers. The square cross-sectional area was $0.13m^2$. The temperature of water, liquid nitrogen and nitrogen vapor was monitored by distributed N-type thermocouples. The thermocouples were mounted on two polycarbonate boards and each board includes sixteen thermocouples distributed vertically. One board was mounted near the wall of the stainless steel box and the other was held in the center of the box. The depths of the thermocouples with reference to the initial water level are given in Table 2. The polycarbonate board was suspended into the metallic cylinder in such a way that thermocouples measured the temperature below water, as well as the temperature of liquid nitrogen and nitrogen vapor above the pool. Each of these thermocouples was calibrated for a temperature range between -200℃ and 50℃ prior to experiment. The cryogenic discharge hose was placed in the middle of the setup to ensure smooth discharge of liquid nitrogen on water in the center of the chimney. The entire setup was placed on a balance (maximum load – 300 kg and sensitivity – 100g) to monitor the mass change when nitrogen vaporized. The sensors' output was recorded every second (1Hz) by a Data Acquisition system (DAQ), and the recorded data were sent to a computer for processing.

Table 2. Thermocouple position for water substrate experiment

| Thermocouple Board 1 | | Thermocouple Board 2 | |
|---|---|---|---|
| **Thermocouple number** | ***Distance from water level (cm)** | **Thermocouple number** | ***Distance from water level (cm)** |
| TC-201 | -10.25 | TC-204 | -9.85 |
| TC-202 | -8.15 | TC-205 | -7.7 |
| TC-203 | -6.25 | TC-216 | -5.67 |
| TC-206 | -4.25 | TC-218 | -3.65 |
| TC-207 | -3.25 | TC-219 | -2.65 |
| TC-208 | -2.35 | TC-222 | -2.25 |
| TC-209 | -1.25 | TC-224 | -0.75 |
| TC-210 | -0.8 | TC-225 | -0.25 |
| TC-211 | -0.25 | TC-226 | 0.35 |
| TC-212 | 0.25 | TC-227 | 0.75 |
| TC-213 | 0.65 | TC-228 | 1.25 |
| TC-214 | 1.65 | TC-229 | 2.35 |
| TC-215 | 2.65 | TC-230 | 3.25 |
| TC-217 | 4.75 | TC-231 | 5.35 |
| TC-220 | 7.75 | TC-232 | 8.25 |
| TC-221 | 22.25 | TC-233 | 23.45 |
| Discharge Pipe | | | 13.75 |

* Distance from water surface; positive value means above the water surface, negative one below the water surface


Figure 6**.** Top and lateral views of experiment setup (1) Thermocouple Board 1 (2) Thermocouple Board 2 (3) Carbon Steel Cylinder (4) Stainless Steel Chimney (5) LN2 Discharge Hose (6) Thermocouples

Liquid nitrogen was discharged continuously from a tank of 180 liter capacity through a cryogenic hose (length 15 m, internal diameter 0.013 m). The mass of the entire setup was recorded every 1 second. The rate of mass change was used to quantify the liquid nitrogen ($LN_2$) vaporization rate. The water temperatures at various depths were recorded continuously during the experiment. The release rate was calculated by determining the slope between mass and time and the values are provided in Table 3. In doing this the flashing of $LN_2$ in the air during discharge was neglected due to difficulties in measurement. After completion of each experimental run (when liquid nitrogen is completely vaporized), the ice thickness (if formed) was estimated and the water was stirred to uniform temperature and the final bulk temperature was measured.

The experiment was repeated five times with different amounts of liquid nitrogen. A summary of the five experimental runs with important results is given in Table 3.

Table 3. Summary of water substrate experiment

| Run No. | $LN_2$ Amount Spilled (kg) | Release Rate (kg $s^{-1}$) | Initial Water Tempera-ture (℃) | Final Water Tempera-ture (℃) | Vaporization Flux (kg $m^{-2}s^{-1}$) | Estimated Heat Flux to the pool (kW $m^{-2}$) |
|---|---|---|---|---|---|---|
| Run 1 | 4.7 | 0.07 | 45 | 40 | 0.31±0.06 | 62.3 |
| Run 2 | 9.4 | 0.05 | 40 | 32 | 0.33±0.05 | 66.0 |
| Run 3 | 9.8 | 0.03 | 31 | 22 | 0.34±0.05 | 68.1 |
| Run 4 | 9.0 | 0.03 | 13 | 9 | 0.22±0.08 | 49.8 |
| Run 5 | 14.6 | 0.13 | 41 | 31 | 0.39±0.09 | 78.5 |

### 4.4. Convective Boiling Model

The boiling of cryogenic liquid spilled on water can be modeled by the convective boiling model. The model involves the dynamic determination of heat transfer from the bulk water to the cryogenic liquid pool as the function of the heat transfer coefficient and the temperature difference between water and the cryogenic liquid. The convective boiling of $LN_2$ on water is influenced by different physical properties of the liquid and the hydrodynamic phenomena that influence the boiling process. When a cryogenic liquid touches the water surface, a large temperature difference exists between these two immiscible liquids and this result in rapid boiling with a potential formation of vapor film between cryogen and water surface leading to film boiling. When the water temperature decreases with time, the temperature difference between the two liquids is reduced. This can lead to a shift in boiling regime. The boiling regimes are usually expressed in the Nukiyama curve that shows the wall

superheat on the horizontal axis and heat flux on the vertical axis (see Figure 7). Two critical points are observed in such behavior to characterize the shift in boiling regimes, namely the Leidenfrost point and Critical Heat Flux (CHF) point. The film boiling occurs above the Leidenfrost point, whereas the nucleate boiling occurs below the Critical Heat Flux (CHF) point. Any temperature difference between these two points results in transition boiling. The boiling regimes can be determined based on the temperature difference between water and cryogenic liquid.

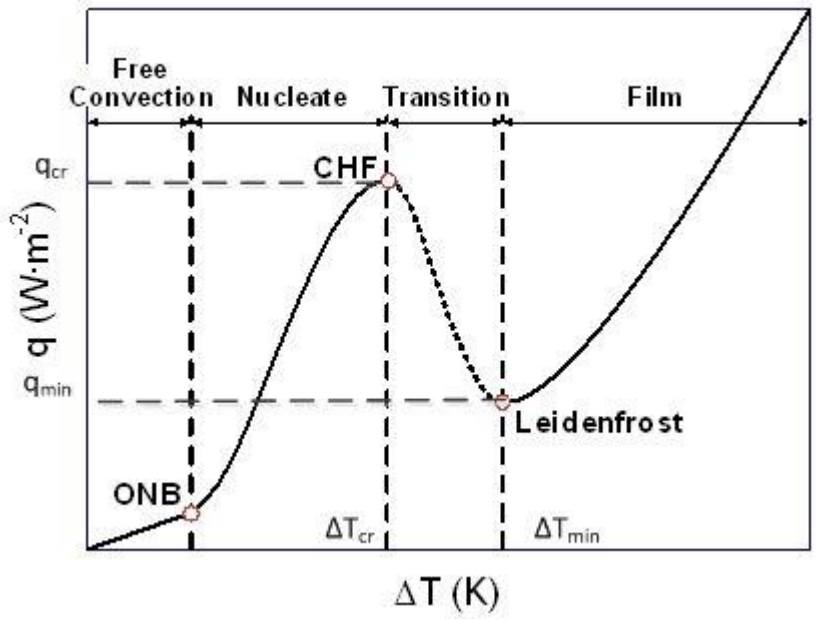


Figure 7. Boiling curve adapted from Nukiyama (1934)

Substantial theoretical correlations exist for predicting the heat flux produced in each regime. Two film boiling correlations differing in underlying theories are

discussed. Berenson (Berenson, 1961) applied the Taylor hydrodynamic instability theory to film boiling based on assumptions of a laminar flow in the vapor film and regular distribution of nucleation sites. Assuming a constant distance between the bubbles and their departure diameters to be proportional to the critical wavelength of the Taylor instability, he obtained the equation for convective heat transfer coefficient $o_{f:}$

$$h_f = C\left[\frac{k_{vf}^3\left(\Delta H_v+\frac{19}{20}C_{p_v}\Delta T_w\right)\rho_{vf}g\left(\rho_l-\rho_{vf}\right)}{\mu_{vf}\Delta T_w\sqrt{\frac{\sigma}{g\left(\rho_l-\rho_{vf}\right)}}}\right]^{\frac{1}{4}} \quad \text{given if} \quad \Delta T > \Delta T_{min} \qquad (21)$$

A value of C=0.425 was used by Berenson for n-pentane and carbon tetra chloride. Similar correlations were developed by Baumeister *et al* (Baumeister, Papell, and Robert, 1964) with a variation in coefficient value of 0.41. Their study involved the boiling of liquid hydrogen, liquid nitrogen and Freon 113 on solid substrates. It is important to note that Berenson did not account for the time variation of the bubble height or bubble diameter in the liquid. This is due to the fact, that hydrodynamic theories like the Taylor instability theory does not account for the effect of substrate. The theory is based on the fact that near the minimum heat flux point in film boiling, the bubble spacing and growth is influenced by Taylor instability alone, rather than fluid depth, substrate type or viscosity. However, when cryogenic liquid is released on water, the characteristic length changes and it is dependent on the angle of contact between the liquid, its vapor and the substrate surface. Berenson's model also assumes that the hot surface temperature remains constant with time and space. However, when liquid nitrogen is released on water, the interface is dynamic and temperature and local heat

flux can vary during the evolution of the interface. To account for these variations, a coefficient value of C=1.4 was applied in the heat transfer coefficient parameter. The coefficient value employed here was determined in an empirical manner for liquid nitrogen boiling on water. Similar modification was previously studied through experiments for various types of cryogenic liquids spilled on water (Jeje, 1974). In that study, the effect of water as a substrate for boiling was incorporated by including a pre-factor value ($\phi = 8.12$) to the critical length variable $\phi\left(\frac{\sigma}{g(\rho_L-\rho_V)}\right)^{-\frac{1}{2}}$ for the $LN_2$-water system. A pre-factor value of φ=7.6 (Jeje, 1974) or a coefficient value of C=1.9 (Gopalaswami *et al.*, 2014) was determined for LNG (comprised of 100% liquid methane) applications.

In contrast to the Taylor instability theory, Klimenko provided an approach to pool film boiling on a horizontal surface on the basis of the Reynolds analogy (Klimenko, 1981). He assumed that the heat-transfer rate in a region depends on the size of the heating surface and established an empirical formula for laminar and turbulent region of the film allowing for this effect given by

$Nu = 0.003\, Ar^{\frac{1}{3}} Pr^{\frac{1}{3}} f_1(\beta)$ for Laminar region where $Ar < 10^8$ (22)

$Nu = 0.00137\, Ar^{\frac{1}{2}} Pr^{\frac{1}{3}} f_2(\beta)$ for Turbulent region where $Ar > 10^8$ (23)

$f_1 = 1$ for $\beta > 0.71$ (24)

$f_1 = 0.89\, \beta^{-\frac{1}{3}}$ for $\beta < 0.71$ (25)

$f_2 = 1$ for $\beta > 0.5$ (26)

$f_2 = 0.71\, \beta^{-\frac{1}{2}}$ for $\beta < 0.5$ (27)

where Nusselt number, Nu is expressed as $\frac{hl_c}{k}$, Prandtl number is expressed as $\frac{C_p\mu}{k}$, Archimedes Number is expressed as $\frac{(2\pi)^3 g l_c^3 \rho_v(\rho_l-\rho_v)}{\mu^2}$, Superheat Parameter, $\beta = \frac{C_{p_v}\Delta T}{\Delta H_v}$. It is important to note that physical properties of liquid nitrogen as function of temperature are required to predict heat flux using Klimenko's model. Similar to Berenson's correlation, Klimenko's correlation had to be modified to take into account the effect of water substrate. To address these changes that occur in water substrate, a value of 0.003 was applied for equation (23) alone as the Archimedes number (Ar) was found to be greater than $10^8$ for the $LN_2$-water system.

The wall superheat at Leidenfrost point $\Delta T_{min}$ is given by Kalinin *et al* (Kalinin, Berlin, Kostyuk, and Nosova, 1976)

$$\Delta T_{min} = (T_c - T)\left[0.16 + 2.4\left(\frac{\rho_l C_{P_l} k_l}{\rho_w C_{p_w} k_w}\right)^{\left(\frac{1}{4}\right)}\right] \quad (28)$$

The minimum heat flux associated with the Leidenfrost Point is provided by Zuber (Forster and Zuber, 1955)and is expressed as

$$q_{min} = 0.177\ \Delta H_v \rho_v \left[\frac{\sigma g(\rho_l-\rho_v)}{(\rho_l+\rho_v)^2}\right]^{\frac{1}{4}} \quad (29)$$

The vaporization mass flux of nitrogen vapor '$m_v$' can further be calculated from an energy balance using sensible heat '$q$' due to convection from water and latent heat due to vaporization of liquid nitrogen given by

$$m_v = \frac{q}{\Delta H_v} = \frac{h\Delta T}{\Delta H_v} \quad (30)$$

## 4.5. Results and Discussion

With the experimental apparatus described in section 4.4, extensive measurements were carried out to obtain experimental data. Typical experimental data are presented in the following sections 4.4.1 and 4.4.2. A comparison of experimental and predicted heat flux are discussed in sections 4.4.3 and 4.4. Additional uncertainty analysis is addressed in section 4.4.5.

### 4.5.1. Vaporization Flux

The mass flux of vapor was determined from mass loss data obtained during the experiment. The averaged vaporization flux obtained for each run is summarized in Table 3 along with 95% confidence intervals. The average heat flux is obtained by multiplying the average vaporization flux with latent heat of vaporization of liquid nitrogen. The spill area that was used to calculate vaporization flux includes a constant cross sectional area of the water surface ($0.13 m^2$) and variable area based on the height of the liquid nitrogen interacting with the stainless steel walls. The cryogenic liquid height was high during the start of vaporization and decreased gradually to zero with vaporization. The average area determined based on the height of cryogenic liquid varied from 0.01 to 0.09 $m^2$. The vaporization fluxes were averaged on a 30s basis and are provided in Figure 8.

Figure 8 indicates that the initial vaporization fluxes were dependent on the liquid nitrogen spill rate. This dependency can be observed as different values of initial vaporization mass fluxes. When the release rate was high, liquid nitrogen covered a large area of water in a short duration of time, leading to an increase in initial heat flux offered

by water. This trend can be explicitly observed in run 5, where a very high initial heat flux was obtained due to the high flow rate with which liquid nitrogen was released in that run.

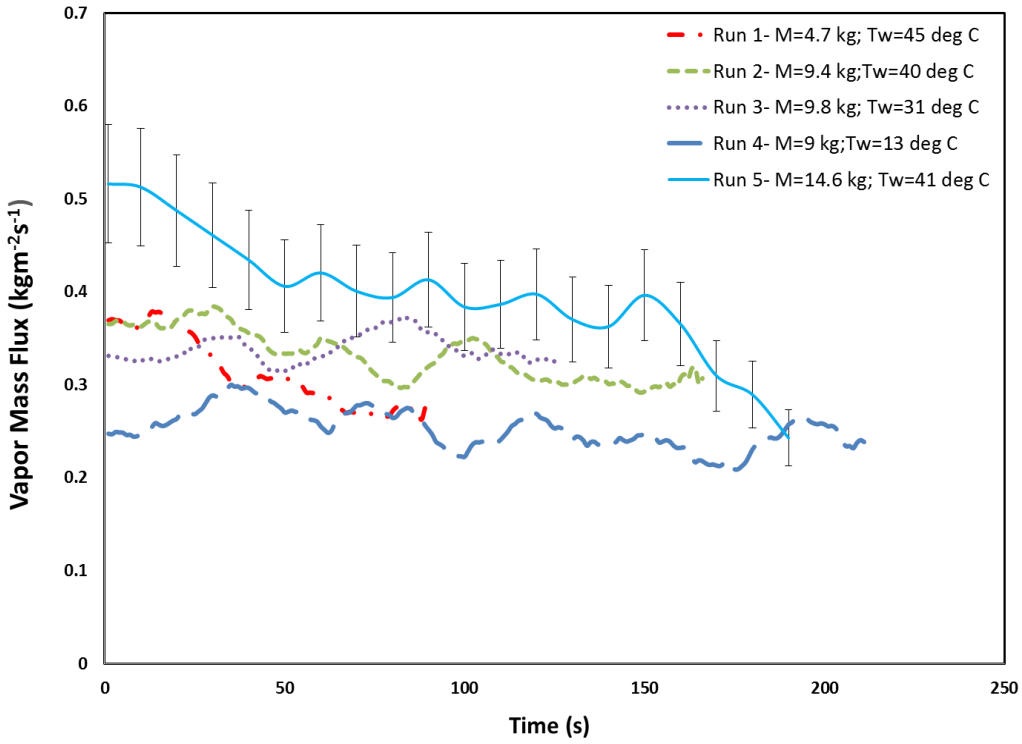


Figure 8. Vaporization mass flux of nitrogen vapor for all runs

The vaporization mass flux was also found to have weak dependence on the initial water temperature. This dependence was based on the variation of the heat transfer mechanism that occurs with change in water temperature. Initially the amount of vapor produced was high when the temperature difference between liquid nitrogen and water was high. As water cooled down, the temperature difference between liquid

nitrogen and water was reduced and heat transfer to the pool was also reduced. The vapor mass flux showed a decreasing trend in all experimental runs where the initial water temperature was high. When the initial water temperature was high, the heat transfer from water to the liquid nitrogen occurred through the convection mechanism *i.e.* the water surface that was cooled by liquid nitrogen was replenished by the hot water from the bulk fluid to the surface. In run 1, run 2 and run 5, when the initial water temperature was more than 40˚C, no ice formation was observed due to convection that occurred throughout the spill. However, this convective heat transfer was restricted completely when a thick ice sheet was formed in the case when the initial water temperature was 13℃ (run 4). When the initial temperature was 31˚C (run 3), ice was found deposited on the walls of the setup and polycarbonate board (Figure 9(a)). The ice formed in run 3 was powdery and melted quickly. When the initial temperature was reduced further to 13˚C (run 4) an ice sheet of thickness 6.5 ± 0.5 cm was formed. The ice formed was smooth and opaque in nature (Figure 9(b)). A constant vaporization flux was observed in these two tests. When the initial water temperature was low, heat transfer to the cryogen was restricted by the growing ice sheet that does not allow hot bulk fluid to be replaced at the surface. The ice sheet served as resistance to heat transfer between water and cryogenic liquid. This resistance is also responsible for the long vaporization time in Run 4. One can infer that this type of prolonged vaporization is possible in real LNG incidental spills, as the water temperature is comparable to sea temperature. This condition can sometimes lead to accumulation of a flammable vapor cloud near the leak area, when non-neutral atmospheric conditions exist.

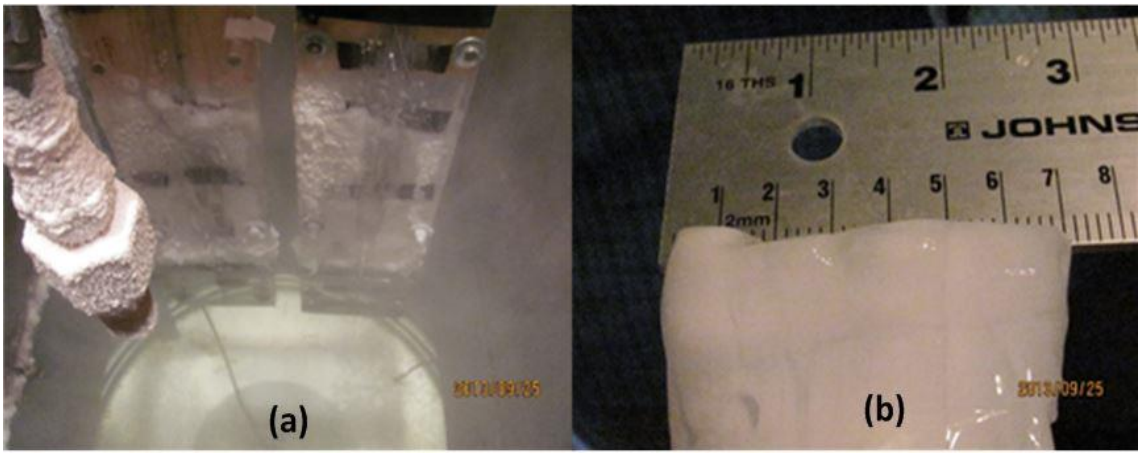


Figure 9. Ice formation in Run 3 (left) and (b) Run 4 (right)

The average vaporization flux and the corresponding heat flux are compared with literature values with similar experimental conditions in Table 4. The average vaporization fluxes obtained in this experiment were found to be 2-3 times greater than the than average vaporization mass fluxes obtained by Bureau of Mines ( Burgess *et al*., 1970) and Drake *et al* (1975a), (Jeje, 1974). The average vaporization mass fluxes obtained in these tests were also comparatively higher than the values reported in LNG dispersion experiments like Burro test series (Koopman *et al.*, 1982) and relatively recent medium-scale LNG tests (Cormier *et al*., 2009), (Qi *et al.*, 2010), (Gopalaswami *et al.*, 2014.) which reported a value of 0.2 kg $m^{-2}s^{-1}$. The variation can be attributed to the size of water body with different spill area observed in literature tests. As the size of water body and spill area increases, the heat available for convection increases. As a result of increased convection in water, the vaporization rate of liquid nitrogen increased.

Table 4. Comparison of results with literature data

| Experiment | Mass of $LN_2$ spilled | Total mass of water | Initial water temperature | Final water temperature | Spill area | Water Mass/ Spill Area | Avg. heat flux | Avg. vaporization mass flux |
|---|---|---|---|---|---|---|---|---|
| | kg | kg | °C | °C | $m^2$ | kg $m^{-2}$ | kW $m^{-2}$ | kg $m^{-2}s^{-1}$ |
| Bureau of Mines ( Burgess *et al.*, 1970) - Run 1 | 1.8 | 19 | 32 | Not Available | 0.18 | 106 | 24 | 0.13 |
| Drake *et al* (Jeje, 1974) - Run 181 | 0.054 | 0.8 | 31.4 | ~ 8 | 0.074 | 11 | 24 – 30 | 0.16 |
| This Experiment (Run 3) | 9.8 | 128 | 31 | 23 | 0.13 | 1045 | 68 | 0.34 |
| This Experiment (all runs) | 4.7 – 14.6 | 127 – 138 | 13-45 | 9 – 40 | 0.13 | 1045 - 1127 | 50 – 78 | 0.22- 0.39 |

### 4.5.2. Temperature Profiles Below Water Surface

Figure 10 shows the temperature values at various levels below water for run 1. Similar temperature values from thermocouples are obtained for other runs. Figure 10 also shows the change in mass with respect to time during the spill as dashed black line. As $LN_2$ mass was continuously added to the setup, the thermocouples contacted liquid nitrogen instead of water and it reflected $LN_2$ temperature. This is observed in thermocouples placed at 0.3 cm and 0.8 cm below the water surface. The trend is possibly due to circulation of water present inside the stainless steel chimney to outer metallic cylinder when liquid nitrogen is discharged in the setup. Among the thermocouples placed closer to the surface, the ones which did not contact liquid nitrogen were used to determine the predicted heat flux. It can also be observed from Figure 10 that throughout the experiment, fluctuations (noise) are observed in the temperature profiles. The fluctuations in thermocouples can be possibly attributed to the penetration of $LN_2$ jet into the water during discharge. The fluctuations increase along with the mass and reach a maximum value when mass of liquid nitrogen reaches a maximum value. This reflects the increase in penetration of $LN_2$ jet into water with increase in $LN_2$ mass. The frequency of fluctuations observed in thermocouples during $LN_2$ discharge was found to be higher than the fluctuation frequency obtained after discharge. The high noise during discharge can be attributed to external interaction like discharge of liquid nitrogen which was not present when discharge was cutoff. The fluctuations observed after discharge can be attributed to movement of convection currents from water surface to bulk water (during vaporization).

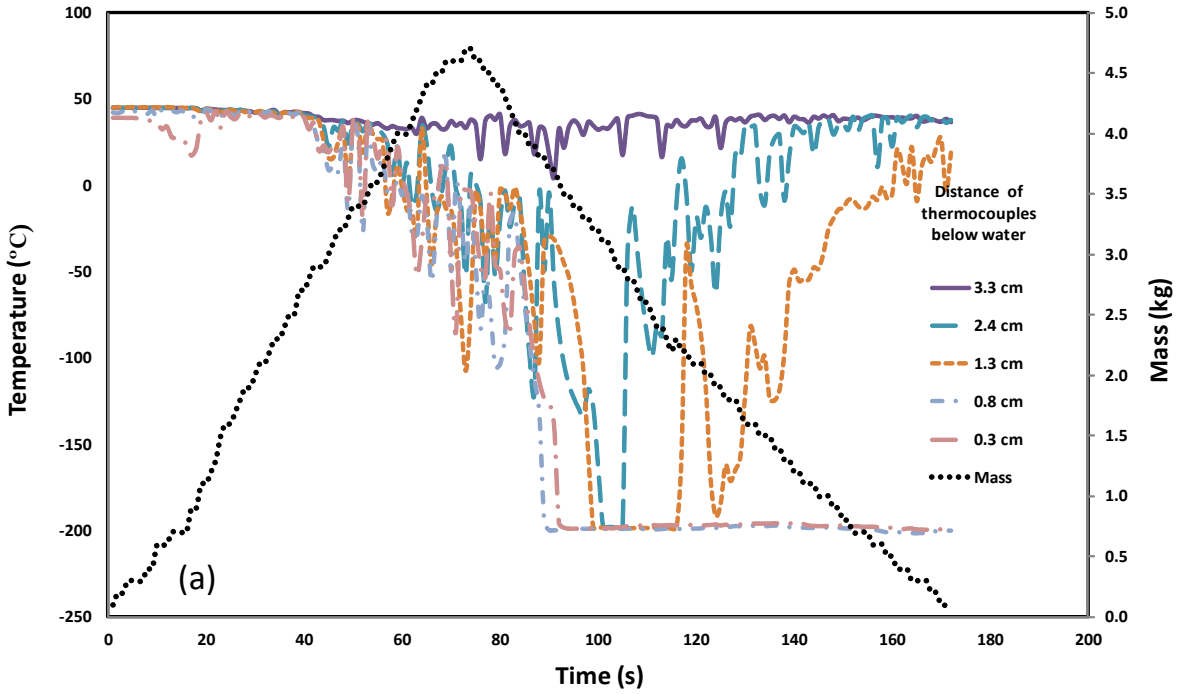


Figure 10. Temperature profile below water surface for Run 1

Figure 11 shows the bulk temperature profiles of water for all runs. Thermocouples placed deeper than 6 cm below the water surface registered very low change in temperature and they represented the bulk water temperature for the entire experiment duration. This observation indicated that large temperature gradient in water happens closer to the water surface. The bulk water temperature profiles for the current study were obtained from TC-201 that was placed at a distance of 10.25 cm below water surface. An overall reduction in bulk water temperature of 5-10 ℃ was observed in each run. This temperature difference in water was sufficient to provide the heat required to vaporize the entire $LN_2$ spilled in the experiment. This behavior is attributed to the large difference in heat capacity observed in $LN_2$ and water.

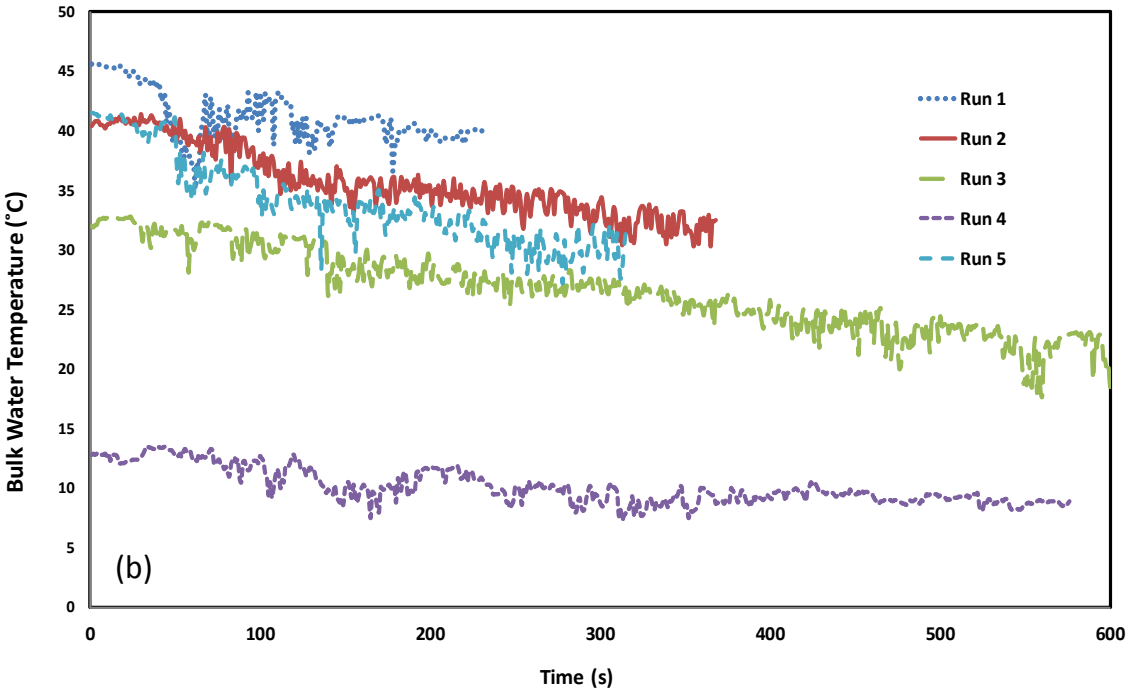


Figure 11. Bulk water temperature profiles for all runs

### 4.5.3. Comparison of Experimental and Predicted Heat Flux

A comparison of heat flux predicted by the model with the heat flux obtained in the experiment (presented in section 4.4.1) is presented in Figure 12-16. The predicted heat flux was calculated using Berenson's correlation and Klimenko's correlation discussed in section 4.3.

Both the predicted heat flux and experimental heat flux were in good agreement for the first four runs using Berenson's correlation. The Klimenko model's prediction was in good agreement for run 3 where a constant vaporization mass flux was obtained. However, both under-prediction and over-prediction was observed for Klimenko's correlation. All the first four runs showed an overall decreasing trend which was well

captured by the Berenson's model. However, the heat flux is found to be independent of time for Klimenko's model. In run 4, a bias is observed in Klimenko's model due to the significant ice formation that was observed during the experiment. As initial water temperature was 13℃, water had cooled down rapidly below the freezing temperature during the experiment. Since the prediction model does not account for ice formation, the variation in heat flux due to ice formation is not captured by the model. Similar bias between predicted and experimental heat flux was observed for run 5 for both the models. In run 5, very high initial heat flux was observed due to the high flow rate with which liquid nitrogen was released. When the release rate was high, liquid nitrogen covers a large area of water in a short duration of time, leading to an increase in initial heat flux offered by water. Since the pool boiling correlations are developed for a stationary pool, variations that occur due to pool movement are not captured by the model. Both the correlations were found to be effective in predicting an average heat flux from water to $LN_2$. However, the heat flux obtained by Klimenko's correlation was found independent of time, which does not reflect observed data.

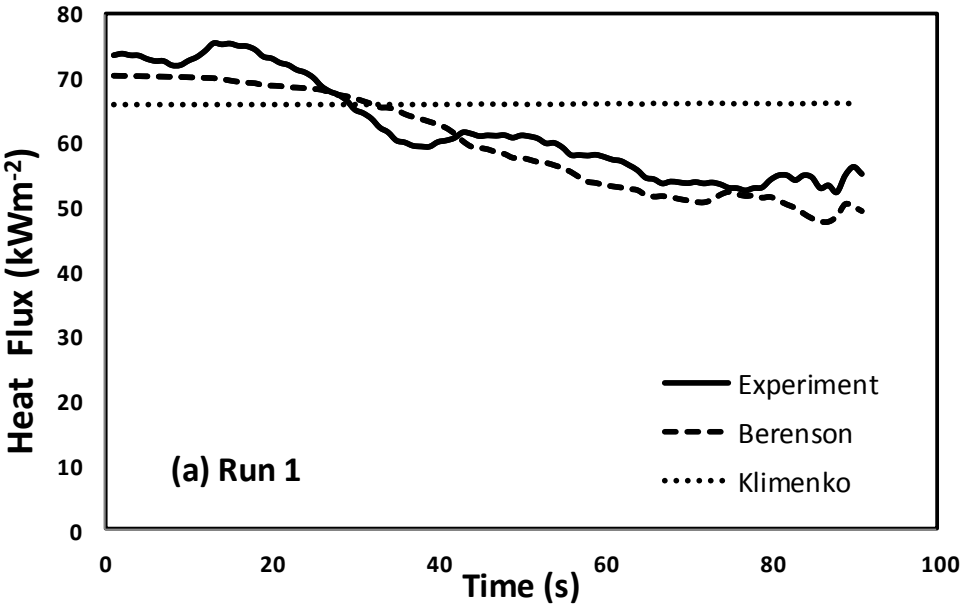


Figure 12. Comparison of predicted and experimental heat flux with time for Run 1

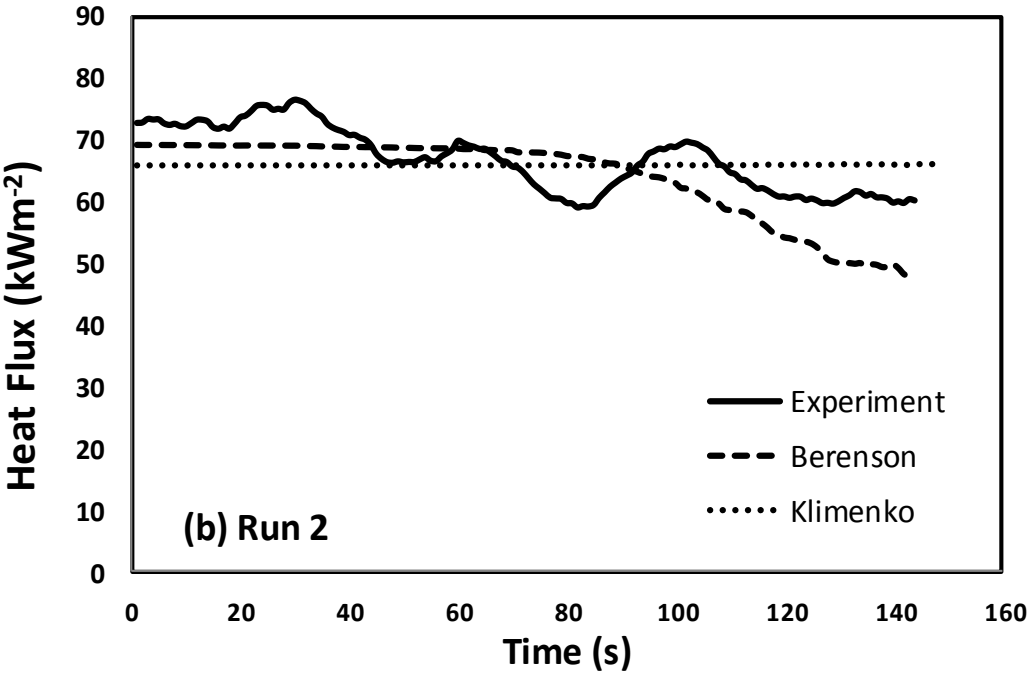


Figure 13. Comparison of predicted and experimental heat flux with time for Run 2

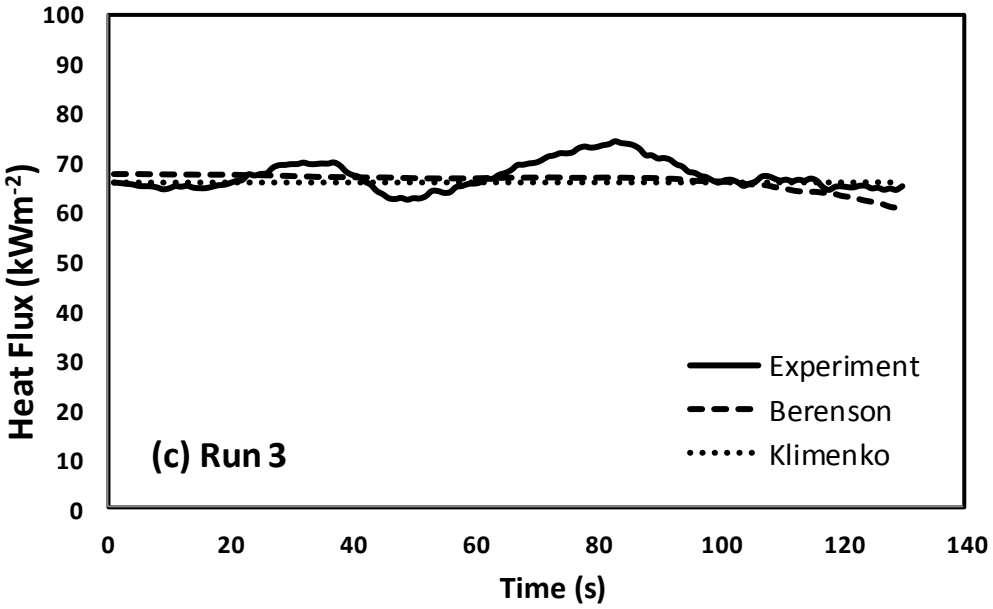


Figure 14. Comparison of predicted and experimental heat flux with time for Run 3

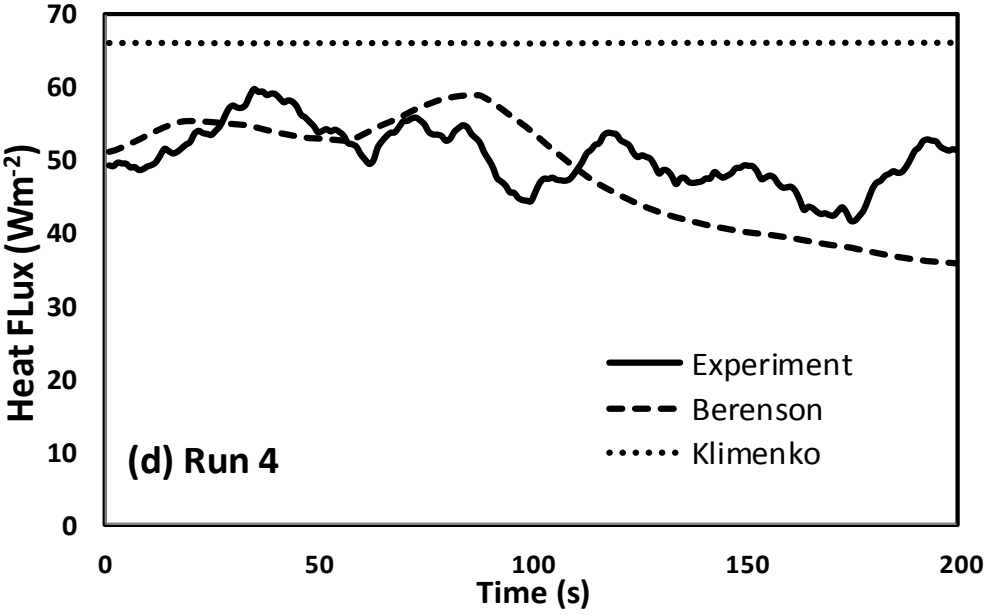


Figure 15. Comparison of predicted and experimental heat flux with time for Run 4

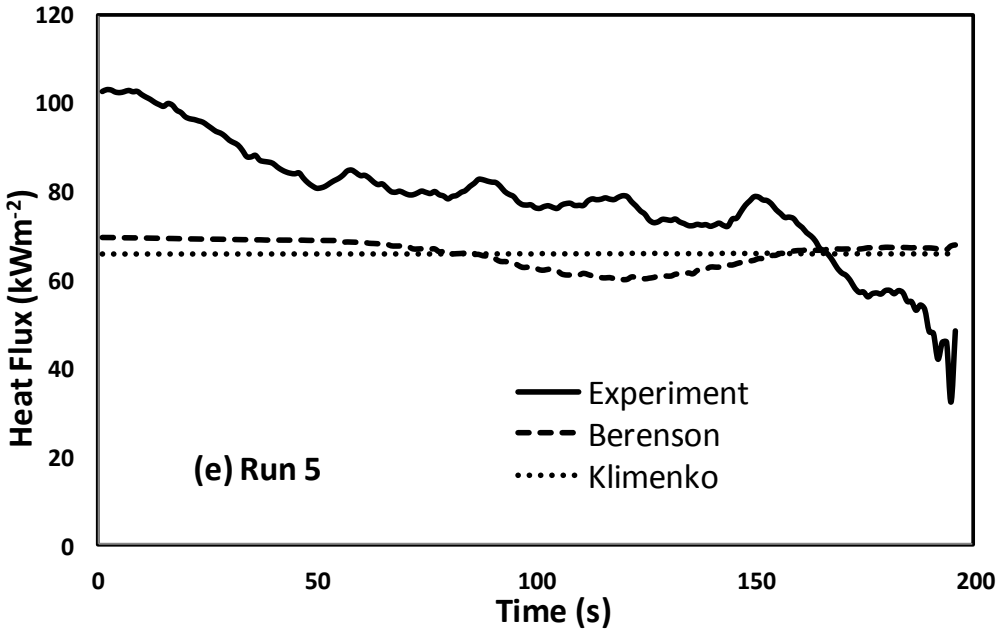


Figure 16. Comparison of predicted and experimental heat flux with time for Run 5

### 4.5.4. Boiling Regimes

A boiling curve was developed using empirical correlations (Equations (21), (28) and (29)) to determine the boiling regimes of the liquid nitrogen boiling on water (discussed in section 4.4.4). The Leidenfrost point, which determines the temperature boundary between film and transition boiling, was calculated to be 75 K. The experimental heat flux determined from mass loss data for all experimental runs are shown in the boiling curve (Figure17). The heat flux data obtained in all experimental runs are representative of film boiling regime. From Figure 17, it can be observed that the initial heat flux obtained in experiment was found to be significantly higher than the predicted heat flux. This is possibly due to the continuous release of liquid nitrogen leading to the agitation of cryogenic liquid pool. The agitation enhances the mixing and

subsequent heat transfer. Wall superheat values and corresponding heat fluxes reflecting nucleate boiling and transition boiling were not observed in the experiment. Figure 18 shows the comparison of two theoretical film boiling correlations with experimental heat flux values. It can be observed that Berenson's model expresses a similar trend and provides a good fit for initial heat flux when the temperature difference is high ($\Delta T >$ 175K). At this stage the film is bound to be laminar in nature due to continuous formation and detachment of vapor bubbles. In real spills of LNG on seas and oceans, the $\Delta T$ is likely to be greater than ~185K and the water body acts as an infinite heat source keeping the water temperature constant. For such cases Berenson's model will provide a better prediction of heat flux from water to cryogenic pool. However, Klimenko's correlation follows a different trend and is more representative of heat flux obtained with a low temperature difference (175- 100K). This temperature difference is less likely in real spills. At this stage the film is bound to be unstable and constitutes both laminar and turbulent regions in the film. Several additional points can also be made based on the current method for predicting heat flux based on convective boiling. Berenson's model provides a good prediction without taking into account the variations of pertinent physical properties involved in convective boiling of cryogenic liquids on water. However, a variation in physical properties of liquid nitrogen with respect to temperature is required for proper prediction of heat flux using Klimenko's model. This is expected, as the underlying theories of these models vary significantly. It can be demonstrated that the $\beta$ value in Klimenko's model plays an important role in determining the dependence of temperature difference on the heat transfer coefficient.

When $\beta$ value is small (<0.5), the heat transfer coefficient is expected to vary as $\Delta T^{-\frac{1}{2}}$ or $\Delta T^{-\frac{1}{3}}$ and when $\beta$ value is large, the heat transfer coefficient is found to be independent of temperature difference. Since $\beta$ is observed to be large (β=1.3) for the liquid nitrogen-water system, a straight line is observed for Klimenko's correlation in Figure 18 indicating that the heat transfer coefficient was independent of the temperature difference. This was a contributing factor for sub-optimal performance of this model in capturing the decreasing trend of heat flux with respect to time.

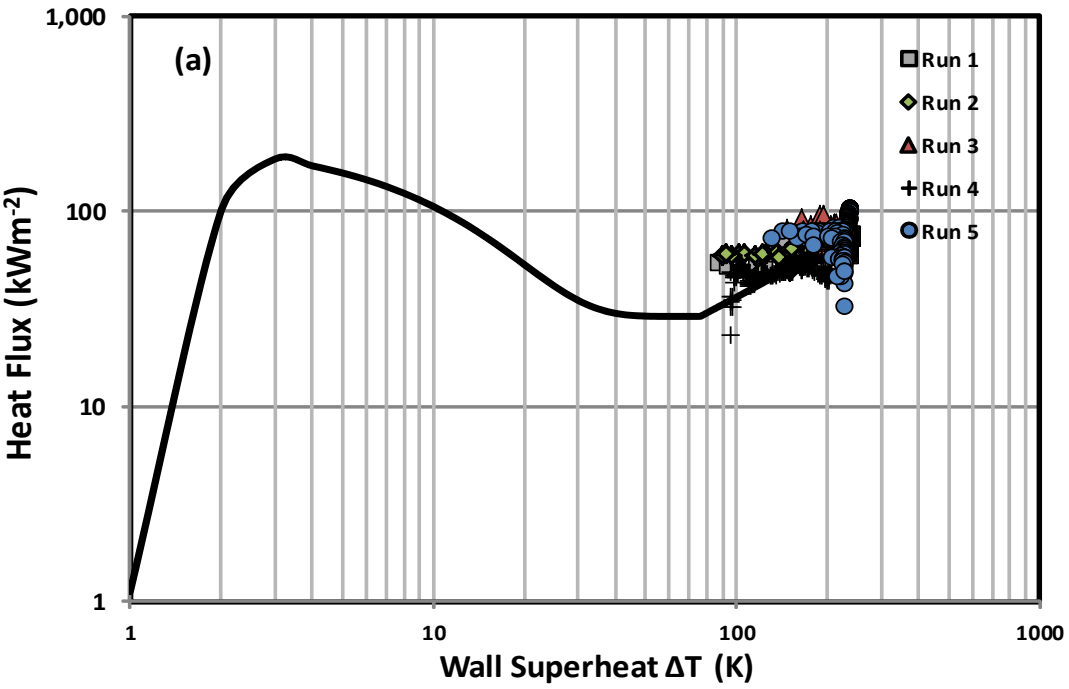


Figure 17. Boiling regimes of liquid nitrogen released on water shown on the boiling curve

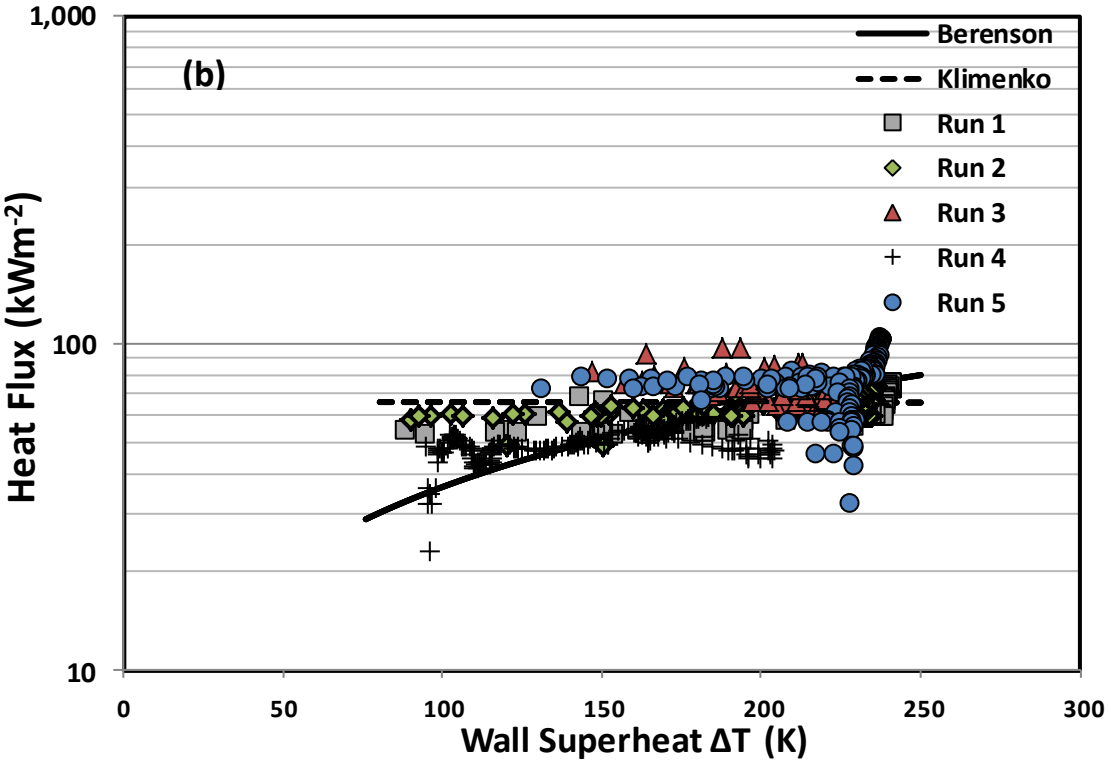


Figure 18. Enlarged view of film boiling regime of liquid nitrogen boiling on water

### 4.5.5. Uncertainty Analysis

The release of cryogenic liquid on water involves a two-phase flow with complex physics. The results of such complex physics are often associated with significant uncertainty, which primarily arise from various measurements involved in the experiment. The uncertainty associated with the experimental heat flux ($q_e$) is estimated from the uncertainty of measured variables like mass (m), time (t) and area (A). The propagation of error in the derived parameter, heat flux is given by Bevington (Bevington and Robinson, 2003)

$$\frac{\Delta q_e}{q_e} = \sqrt{\left(\frac{\partial q_e}{\partial m}\right)(\Delta m)^2 + (\frac{\partial q_e}{\partial t})(\Delta t)^2 + (\frac{\partial q_e}{\partial A})(\Delta A)^2} \quad (31)$$

The resolution of the weighing balance used in the present study is 0.1 kg. The uncertainty associated with the averaging time is 0.03s. The uncertainty estimated in the variable, area was found to be 0.015 $m^2$. Hence the error propagated to experimental heat flux was ±9.7%. Similarly the uncertainty in predicted heat flux was a function of temperature. The uncertainty in predicted heat flux is given by

$$\frac{\Delta q_p}{q_p} = B\left(\frac{\Delta T}{T}\right) \quad (32)$$

where B is a constant dependent on the physical properties of liquid nitrogen and water. The N-type thermocouples were calibrated at temperatures ranging from 77 to 308 K. The temperature offset, which is the difference between reference temperature and measured temperature during calibration, was obtained using interpolation between three calibration temperatures (77 K, 237K and 308 K). A Piecewise Cubic Hermite Interpolating Polynomial (PCHIP) method implemented in Matlab® (version 7.0) was used to calculate the offset. The offset was found to be ±2.3 K. The tolerance value of N-type thermocouples is ±1.7 K. The total uncertainty propagated to the predicted heat flux was found to be around ±12.3%. A visual interpretation of the total uncertainty on vaporization mass flux is presented for run 5 in Figure 8. In addition to these, uncertainty existed due to change in position of thermocouples during the experiment, which could not be quantified.

### 4.5.6. Application to Real Scenarios

It is to be noted that the vaporization of LNG spilled on open water is different from the vaporization of LNG on a confined area of water. The LNG spills on open water do not form any ice during the pool spreading and vaporization process. In general, as the size of the water body increases, the temperature change in water decreases. This is due to the fact that as the size of water body increases, the water available for supplying heat through convection increases. This results in little or no temperature change of bulk water when virtually infinite heat source like oceans and seas act as a substrate. As a result of this, the temperature difference between LNG and water will remain constant, and the Leidenfrost point will never be crossed. The entire boiling process is then described by the film boiling phenomenon. The resultant vaporization mass flux is bound to remain constant with respect to time. However, the vaporization rate will vary as long as the pool is spreading. After the maximum pool diameter has been reached, the pool area decreases. The pool spreading parameters will follow a trend similar to unconfined spills. However, the vaporization mass flux will be constant with respect to time.

When the temperature of sea water is higher than normal, large amount of vapor will accumulate in short duration of time. In large seas and oceans, the pool can also break into smaller pools due to actions of waves and tides, which is not present in confined area of water. Similarly the vaporization of LNG is different from liquid nitrogen from the fact that LNG can contain a mixture of hydrocarbons whereas liquid nitrogen is a pure component. Due to this reason, preferential vaporization can take place

in LNG leading to higher vaporization rates with accumulation of higher hydrocarbons. However, if LNG is light consisting entirely of pure methane then, there would be no preferential vaporization. A vaporization trend similar to liquid nitrogen can be expected with changes in magnitude in the vaporization mass flux.

## 4.6. Conclusion

An experimental investigation of small-scale continuous releases of liquid nitrogen on water was performed to improve the understanding of source-term modeling of cryogenic liquid spills. The vaporization fluxes obtained were independent of the amount of liquid nitrogen spilled. However, initial vaporization flux was dependent on liquid nitrogen spill rate and initial water temperature. The vaporization mass flux was also found to increase with the size of water body and spill area. Significant ice formations were observed in spills where the initial water temperature was 13℃. The ice formation increased the vaporization time due to increased heat transfer resistance. It was demonstrated that the convection in water is the dominant heat transfer mechanism when cryogenic liquids are spilled on water. Additionally, liquid nitrogen was found to be in the film boiling regime when released on water. The experimental heat flux values were validated with two prediction correlations for convective heat flux. Berenson's model was able to capture the decreasing trend of heat flux with respect to time, which was not possible by Klimenko's model. The validated heat flux prediction model proves beneficial for source-term modeling of cryogenic liquids released on water.

# CHAPTER V

# QUANTIFICATION OF HEAT FLUX FROM ICE TO CRYOGENIC LIQUID[2]

## 5.1. Introduction

One of the potential LNG incident scenarios is the collision of an LNG ship with an iceberg during marine transportation (Lee and Nguyen, 2011). Detailed consequences analysis considering various scenarios and hypotheses through calculations are required for LNG carriers. Consequence analyses in such cases depend on features of the ice and the structural strength of the LNG carrier. Two of the common types of collision that can occur are the side collision between side of the LNG vessel and iceberg and bow collision between forward part of hull and iceberg (Dahl, 2012). Special carriers like 'ice class LNG carrier' are being designed which have a strengthened hull to enable them to navigate through sea ice. However a collision with an iceberg can result in damage of the vessel and allow leakage of contents on ice or ice-water mixture. Such a scenario is common in areas where ice is predominantly present throughout the year like the Arctic Circle. Upon spillage of contents, one of the most important factors that affect cryogenic liquid release on ice is the heat flux from ice to cryogenic liquid. This process is different from the heat transfer between water and cryogenic liquid as ice is a solid and conduction phenomena is more dominating than convection due to boiling.

Very few experiments were performed by releasing cryogenic liquids on ice. In 1971, Nakanishi observed that when cryogenic liquids like Condensed Pipeline Gas

[2] Part of this section is reprinted with permission from "Small-Scale Experimental Study of Vaporization Flux of Liquid Nitrogen Released on Ice", by Gopalaswami, N., Vechot, L., Olewski, T., & Mannan, M. S. Journal of Loss Prevention in the Process Industries, Copyright [2015]. Elsevier

(CPG, with composition CH4 92.7%, N2 7.3%; boiling point about -111.6K) and Liquid Nitrogen ($LN_2$, boiling point -77 K) were poured on an ice layer maintained at -150 ˚C, there was no vapor film formation under the cryogen's layer and both liquids were found to be boiling in the nucleate regime (Nakanishi and Reid, 1971). When the experiment was repeated by pouring onto an ice layer maintained at -5 ˚C, a vapor film was observed to occur for liquid nitrogen alone, but not for CPG. It was concluded that when CPG was spilled on ice, it stays in film boiling for a brief period. This might have been due to the fact that the temperature difference between ice and CPG would have been small to sustain film boiling for a long period. This phenomenon was not addressed in detail in their research work.

In another study, small-scale experiments were performed with liquid nitrogen and LNG (Burgess, Murphy, and Zabetakis, 1970). The primary objective of this study was to measure the heat flux and the vaporization rates. The experiments were performed at laboratory scale, (spill area - 0.18 $m^2$) where cryogenic liquid was poured onto a flat tray (30.5 x 61 cm) of ice. The ice was made 4 cm thick and covered the entire surface of the tray such that the cryogenic liquid contacted only ice. LNG and $LN_2$ were released on ice. An array of thermocouples was placed below the ice to measure the time dependent temperature and associated heat transfer. However, wrinkling of the ice-cryogen interface disturbed the position of thermocouples and a spatial variation of heat transfer was not obtained in the test. The amount of cryogenic liquid poured was varied and the vaporization rate was reported for the experiment. The vaporization rates of nitrogen on ice varied from 0.08-0.12 kg $m^{-2}s^{-1}$. The small-scale tests showed a lot of

variation in the vaporization rates reported for liquid nitrogen. The vaporization rates were reported for discrete values of time rather than for a continuous time interval.

A heat transfer model for growing ice thickness involving conduction and convection phenomena for release of cryogenic liquids on shallow water was undertaken by Vesovic (2007). However, the model was not validated with any experimental data. In all these experiments the source-term and the heat flux from the substrate (ice) to the pool was calculated by measuring the temperature difference between the substrate and cryogenic liquid pool with time. This was possible by measuring the temperature difference between the substrate and cryogenic pool and using analytical expressions to determine the heat flux. The conclusions of small-scale experiments had limited effects due to the small confined space of the boiling cell. Most of the tests were also qualitative in nature and currently there are very few quantitative results for cryogenic liquids released on ice. It is also important to note that the current results do not show the time dependent behavior of vaporization rates.

An experimental investigation is undertaken here to improve the understanding of cryogenic liquid releases on ice and to provide benchmark qualitative and quantitative results. The small-scale experimental study was performed to verify the heat transfer mode of cryogenic liquids released on ice and independently validate the one dimensional conduction for cryogenic liquid released on ice. In doing this, the vaporization mass flux of liquid nitrogen was determined by mass loss in the experiment and temperature measurement. The results of the experiment were reported with respect to time to understand the variation of vaporization rates with respect to time.

## 5.2. Experimental Setup and Procedure

The experimental setup designed for small-scale spills of liquid nitrogen on ice is shown in Figure 19 and Figure 20. Figure 19 shows the ice block which was used as substrate for the experiment. Figure 20 shows the entire experimental setup. The small-scale experiments were performed in Fire Station 2 of the Ras Laffan Industrial City, Qatar. The setup consisted of a metallic cylinder with an inner diameter of 58.5 cm and a height 87.5 cm made of carbon steel. A stainless steel chimney (box) with dimensions 35X35X80 cm was placed inside the metal cylinder to protect it from fractures resulting from a cryogenic liquid spill. The stainless steel chimney was a square shape in cross-section and devoid of top and bottom. The square cross-sectional area was 0.13 $m^2$. The stainless steel chimney was lowered into the metallic cylinder using a steel support in such a way that the metallic cylinder is half filled with water at any point of time during the experiment and the liquid nitrogen was spilled inside the chimney. The setup ensured that liquid nitrogen interacted only with stainless steel walls of the chimney and water thereby protecting it from fractures. An ice slab of length 25cm, breadth 25cm and height 10 cm was placed inside the stainless steel chimney on top of water. A thermocouple to measure the temperature of the ice was embedded into the ice slab. Additional ice cubes were added around the ice slab to create an ice-water mixture and to limit contact of $LN_2$ with water. The temperature of ice, water below ice, liquid nitrogen and nitrogen vapor was monitored by distributed N-type thermocouples. The thermocouples were mounted on two polycarbonate boards and each included sixteen thermocouples distributed vertically. One board was mounted near the wall of the

stainless steel box and another was held in the center of the box. The dimensions of the thermocouples relative to top surface of ice are given in Table 5. Each of these thermocouples was calibrated for measuring liquid nitrogen and ice temperature. The position of each thermocouple and cryogenic discharge hose nozzle is shown in Table 5. The cryogenic hose was placed in the middle of the setup to ensure smooth discharge of liquid nitrogen on ice. The entire setup was placed on a balance (maximum load – 300 kg and sensitivity – 100 g) to monitor the change of mass when nitrogen vaporizes on ice. The sensors' output was recorded every second (1 Hz) by a Data Acquisition system (DAQ), and the recorded data were sent to a computer for processing.

The liquid nitrogen was discharged continuously from a tank of 180 liter capacity through a cryogenic liquid hose of length 15m and internal diameter 0.0127m, until desired amount of $LN_2$ was reached. The mass of the experimental setup was recorded every 1 second and was used to measure the $LN_2$ vaporization mass flux. The time of opening the cryogenic liquid valve and the time when liquid nitrogen contacted with the ice was noted. The release rate of $LN_2$ was then calculated from the time and mass data (where release rate is discharge rate subtracted by the vaporization rate during the spill). The time to complete vaporization of liquid nitrogen was also noted. The discharges were repeated several times and the total amount of liquid nitrogen released was varied. The temperature of ice decreased after each experimental run due to release of liquid nitrogen on it. A summary of the six experimental runs with initial temperature of bulk water, initial temperature of ice and the amount of liquid nitrogen is given in Table 6.

Figure 19. Ice block as substrate


Figure 20. Top and lateral views of experiment setup (1) thermocouple board 1 (2) thermocouple board 2 (3) metallic cylinder (4) stainless steel chimney (5) $LN_2$ discharge pipe (6) thermocouples (7) ice substrate

Table 5. Thermocouple positions for ice substrate experiment

| Thermocouple number | *Distance from ice surface (cm) | Thermocouple number | *Distance from ice surface (cm) |
|---|---|---|---|
| **TC-201** | -10.25 | **TC-204** | -9.85 |
| **TC-202** | -8.15 | **TC-205** | -7.7 |
| **TC-203** | -6.25 | **TC-216** | -5.67 |
| **TC-206** | -4.25 | **TC-218** | -3.65 |
| **TC-207** | -3.25 | **TC-219** | -2.65 |
| **TC-208** | -2.35 | **TC-222** | -2.25 |
| **TC-209** | -1.25 | **TC-224** | -0.75 |
| **TC-210** | -0.8 | **TC-225** | -0.25 |
| **TC-211** | -0.25 | **TC-226** | 0.35 |
| **TC-212** | 0.25 | **TC-227** | 0.75 |
| **TC-213** | 0.65 | **TC-228** | 1.25 |
| **TC-214** | 1.65 | **TC-229** | 2.35 |
| **TC-215** | 2.65 | **TC-230** | 3.25 |
| **TC-217** | 4.75 | **TC-231** | 5.35 |
| **TC-220** | 7.75 | **TC-232** | 8.25 |
| **TC-221** | 22.25 | **TC-233** | 23.45 |
| **TC inside Ice** | 5 | **Discharge Pipe** | 13.75 |

*Distance from top of ice surface; positive value means above the ice surface, negative value means below the ice surface

Table 6. Summary of ice substrate experiment

| Run Number | Total Amount Spilled, (kg) | Release rate, ($kg.s^{-1}$) | Initial temperature of ice, (˚C) | Water Temperature below ice, (˚C) |
|---|---|---|---|---|
| **Run 1** | 4.3 | 0.02 | -11 | 8 |
| **Run 2** | 10.5 | 0.08 | -5 | 13 |
| **Run 3** | 5.3 | 0.05 | -66 | 10 |
| **Run 4** | 2.6 | 0.02 | -51 | 9 |
| **Run 5** | 8.0 | 0.03 | -44 | 8.3 |
| **Run 6** | 13.6 | 0.01 | -119 | 7.4 |

## 5.3. Theory

When a cryogenic liquid contacts the ice surface, a large temperature difference exists between ice and liquid nitrogen which results in rapid vaporization of liquid nitrogen. The heat transfer from ice to liquid nitrogen is predominantly controlled by conduction phenomenon. In this study, one dimensional semi-infinite unsteady heat conduction equation with ideal contact of liquid nitrogen and ice is used to describe the heat transfer process (Carslaw and Jaeger, 1986). This model was mainly chosen for two main reasons. In the experiment there was no pool spreading and the experimental setup was compact with ice layer making perfect contact with the cryogenic liquid. In such cases, the 1D conduction equation provides reasonable estimates of heat flux and temperature. The model was also found to show good results for release on concrete (Olewski, Véchot and Mannan, 2013).

According to the model, the heat flux $q$ from ice to $LN_2$ is expressed as

$$q = \left(\frac{k}{\sqrt{(\pi\alpha t)}}\right)(T_i - T_b)\, exp\left(-\frac{z^2}{4\alpha t}\right) \quad (33)$$

The heat flux is also proportional to inverted square root of time expressed as

$$q = \left(\frac{k}{\sqrt{(\pi\alpha)}}\right)(T_i - T_b)\, exp\left(-\frac{z^2}{4\alpha t}\right).\, t^{-0.5} \quad (34)$$

The temperature $T$ inside the ice at the $z$ depth is expressed as

$$T = T_i - (T_i - T_b).\, erfc\left(\frac{z}{2\sqrt{\alpha t}}\right) \quad (35)$$

where the $T_i$ represents the initial temperature of ice, $T_b$ is the temperature of liquid nitrogen, $k$ is the thermal conductivity and $\alpha$ is the thermal diffusivity of ice. A

perfect thermal contact between liquid nitrogen and ice is assumed in calculating the temperature variation of ice.

## 5.4. Results and Discussion

The results of small-scale experiments are discussed in subsequent sections. The vaporization fluxes determined from mass loss data obtained during the experiment are discussed in Section 5.4.1. The validation of the model with experimental data is provided in Sections 5.4.2 and 5.4.3.

### 5.4.1. Vaporization Mass Flux

The mass flux of vapor (vaporization rate per unit area) was obtained from direct measurement of mass loss data obtained during the experiment (Figure 21.). The vaporization mass flux was obtained by calculating the slope of mass loss with respect to time and area of the pool. The time-period taken for determining the slope refers to the averaging time used in this study. An averaging time of 60 seconds was used to compute the vaporization mass flux of the liquid nitrogen on ice. The selection of averaging time was based on a sensitivity analysis shown in Figure 22. Four averaging times were chosen to calculate the mass vaporization flux of $LN_2$ vapor. The time periods selected for the sensitivity analysis was obtained from literature (D. Burgess *et al.*, 1970). An averaging time of 10 and 20 seconds resulted in large fluctuations in vaporization flux due to low resolution in mass measurement (maximum capacity of balance was 300 kg and resolution was 100 g). An averaging time of 30 seconds resulted in a fairly smooth curve but still with periodic fluctuations. An averaging time of 60 seconds was found to give low variations and thus sufficiently described the vaporization mass flux without

much loss in the actual trend. The spill area included the constant cross sectional area of the 0.13 $m^2$ to determine the vaporization mass flux.

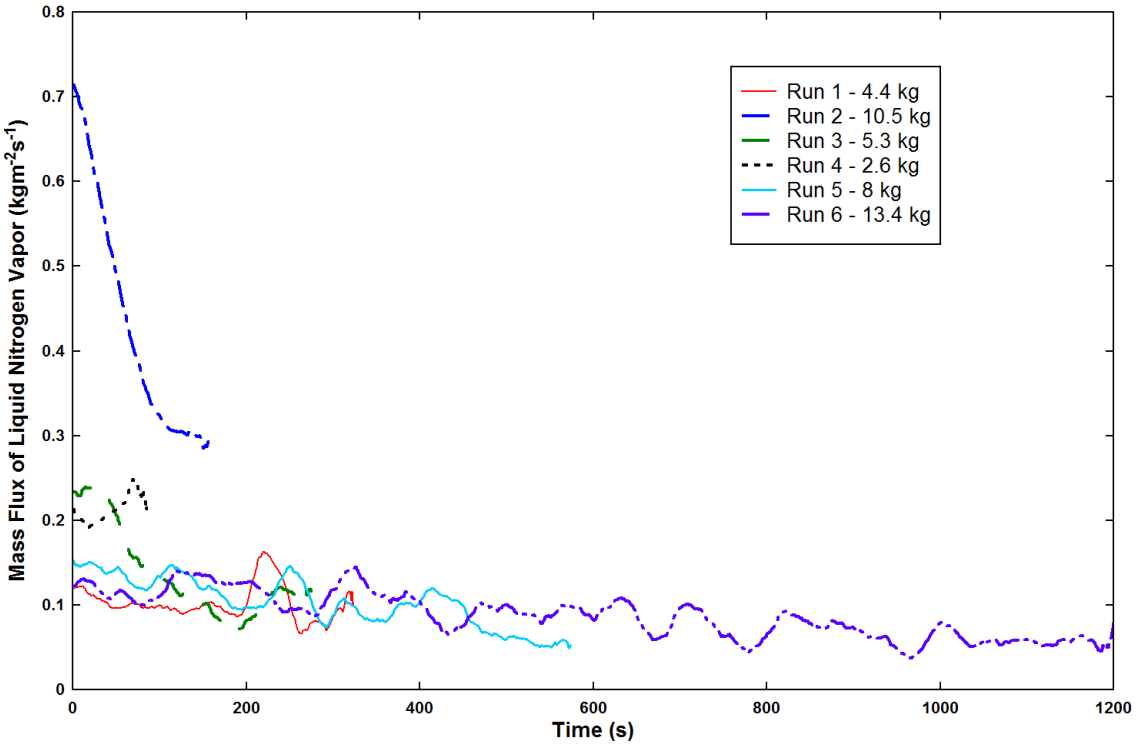


Figure 21. Vaporization Mass Flux

The vaporization mass flux was observed to be dependent on the release rate. Higher release rates lead to higher initial vaporization mass fluxes. This can be observed from the initial values of vaporization mass flux. When the spill rate is higher, the initial contact area of ice wetted by the cryogenic liquid pool is high. Atypical for conduction, a decreasing trend of vaporization mass flux was observed when the release rate was relatively high (0.8 $kgs^{-1}$ and 0.5 $kgs^{-1}$ in run 2 and run 3). When the release rate was

greater than the vaporization rate, the vaporization mass flux follows a decreasing trend. However, the vaporization mass flux became comparatively constant, when the release rate dropped down below 0.3 kg/s, (run 1 and runs 4 to 6).

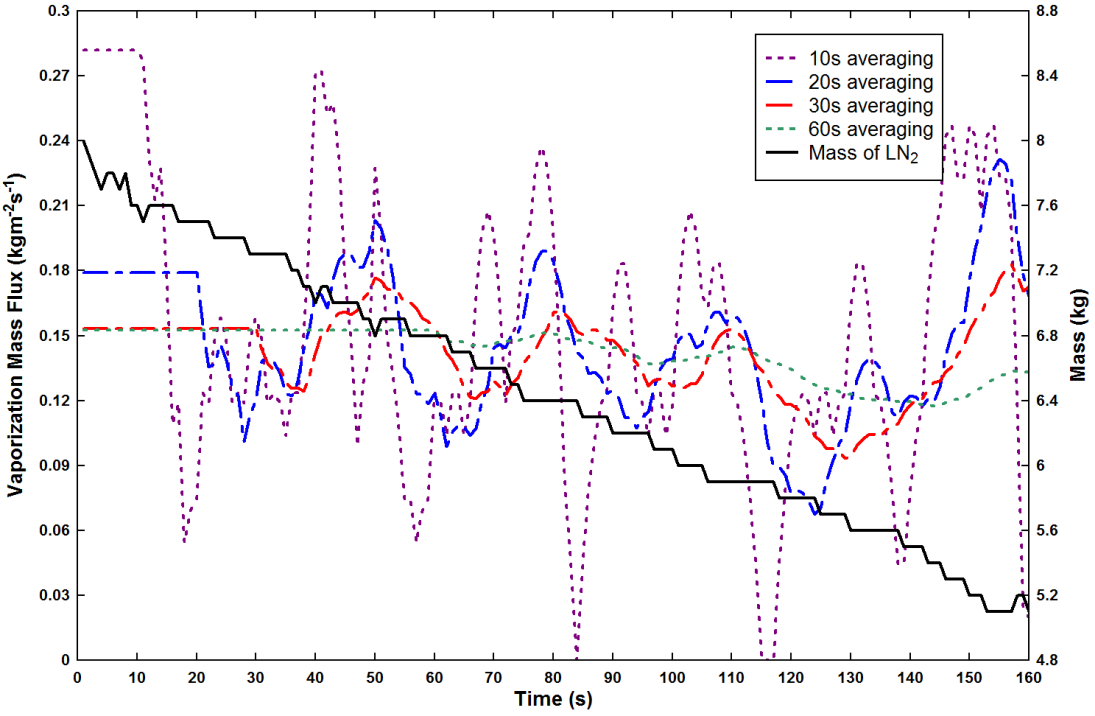


Figure 22. Vaporization flux for different averaging times

As the release rate was reduced, the release rate becomes equal to the vaporization rate. A steady-state is achieved leading to constant vaporization mass flux. This steady-state was also responsible for increasing the time for complete vaporization of cryogenic liquid. It is to be noted that similar results for vaporization mass flux were obtained by the Bureau of Mines (Burgess *et al.*, 1970), where a decreasing trend was observed at the initial stage of the spill on ice. This decreasing trend can be attributed to

rapid decrease in temperature difference between ice and liquid nitrogen during the vaporization process. Once the ice substrate temperature equalizes the cryogenic liquid pool temperature, constant vaporization mass flux is obtained. This indicated that the release rate influences the variations in ice temperature. Additionally a small peak in vaporization mass flux was observed during run 1 (Figure 21). This is potentially attributed to interaction of liquid nitrogen in water causing a peak in vaporization mass flux. After each spill, the ice temperature and water temperature reduced significantly.

A summary of results for all experimental runs is shown in Table 7. An average heat flux of 36.6 $kWm^{-2}$ was measured in the tests, which represents an average vaporization flux of 0.18 $kgm^{-2}s^{-1}$. The values of vaporization mass flux were compared with experiments conducted by Bureau of Mines (1970). The average heat flux obtained in their experiment was around 25.85 $kWm^{-2}$ with corresponding vaporization flux determined to be 0.13 kg $m^{-2}s^{-1}$. The variability can be attributed to the lack of water and ice mixture that was not present in their experiments. A combination of ice and water mixture results in heat fluxes that are intermediate between heat fluxes obtained due to convection and conduction.

Table 7. Summary of results for ice substrate experiment

| Run Number | Average Vaporization Mass Flux ($kg\ m^{-2}s^{-1}$) | Average Vaporization Rate ($kg\ s^{-1}$) | Estimated Heat Flux to the pool ($kW\ m^{-2}$) |
|---|---|---|---|
| **Run 1** | 0.10 | 0.01 | 20.6 |
| **Run 2** | 0.42 | 0.05 | 82.7 |
| **Run 3** | 0.13 | 0.02 | 26.6 |
| **Run 4** | 0.21 | 0.03 | 41.9 |
| **Run 5** | 0.10 | 0.01 | 20.3 |
| **Run 6** | 0.09 | 0.01 | 17.6 |

Initially during the start of experimental runs, the ice block was transparent in nature. With the release of liquid nitrogen in every test, the thickness and opacity of ice increased. This variation can be explained due to the formation of different phases of ice with changing temperature. Currently sixteen crystalline phases and three amorphous phases are observed at different temperature and pressures (Zheligovskaya and Malenkov, 2006). As liquid nitrogen was spilled, reduction in ice temperature occurred. This led to the formation of hexagonal ice ($I_h$) which occurred at temperature ranges between -115-0˚C at atmospheric pressure (Kuhs and Lehmann, 1986). Further reduction in temperature at constant atmospheric pressure produced cubic ice ($I_c$). It is produced at temperatures between 130 and 220 K, and can exist up to 240 K after which it transforms into hexagonal ice $I_h$. In addition to it, small ice balls were formed during each experiment on the surface of ice, which might be attributed to super-cooling of water from air at atmospheric pressure. The ice balls formed are amorphous in nature and called Low Density Amorphous (LDA) ice. The ice balls and opaque ice sheet formed during the experiment are shown in Figure 23. The size of the ice balls ranged from 0.35-0.9 cm. As the spill continued the thickness of ice increased from an initial

value of 10 cm to a final value of 11.5±0.03 cm. As the thickness increased, the temperature change in ice due to spill decreased. It is important to note this growing ice thickness in the pool, created resistance to heat transfer and thus controlled the heat flux supplied to the cryogenic pool. This resistance is also responsible for constant trend of vaporization mass flux with respect to time for all runs (except run 2) in Figure 21. The resistance additionally increases the time for liquid nitrogen to vaporize completely. This can be observed from vaporization mass flux curves of Run 5 and Run 6 whose vaporization time were high. These tests were noted to have maximum ice thickness owing to repeated spills of liquid nitrogen.

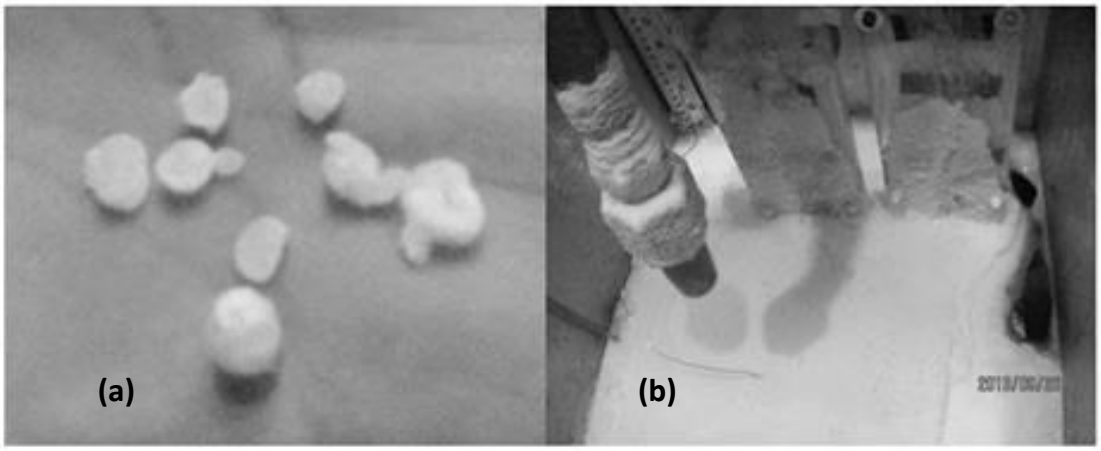


Figure 23. Ice formation during the spill (a) ice balls (b) opaque ice sheet

For consequence analysis of real large-scale scenarios one should consider the different types of icebergs in the analysis. A general classification of different types of iceberg based on size is given in Table 8 (Diemand, 2001). A detailed classification of

ice is available in sea ice nomenclature, which can be adopted for performing consequence analysis (Bushuyev, 1970). The classification takes into account different features of ice like origin, formation, salinity and size. Large icebergs are likely to be detected by radars installed in the ship or by airborne radars. However, the small icebergs are less likely to be detected by radars and hence they require special attention. Additionally, small icebergs with large thickness tend to prolong the vaporization time. This can cause the accumulation of flammable vapors near leak area. Hence a severe risk is associated with collision with small icebergs like growlers and Bergy bits. These account for rare events and should not be disregarded when modeling incidental scenarios. Once the type of iceberg is chosen, appropriate properties of iceberg (size, temperature, physical properties) can be included in the model for determining the vaporization rates.

Table 8. Classification of iceberg based on size (Diemand, 2001)

| Size Category | Height (m) | Length (m) |
|---|---|---|
| **Growler** | < 1 | < 5 |
| **Bergy Bit** | 1-5 | 5-15 |
| **Small** | 5-15 | 15-60 |
| **Medium** | 16-45 | 61-120 |
| **Large** | 46-75 | 121-200 |
| **Very Large** | over 75 | over 200 |

Another important consideration for modeling real incidental scenarios is the salinity of water in which ice is present. For releases on ice-water mixture, it should also be noted that release of cryogenic liquid on salt water is different from a release on fresh water. The salinity of seawater is around 3.5% whereas for fresh water it is around 0.1 %

(Sharqawy, Lienhard V, and Zubair, 2010) . As a result of this, the freezing point of seawater ($-2^0$C) is greater than fresh water which is present at lower salt concentration ($\sim 0^0$C). Due to this difference in freezing point, ice formation is prevented or formed later when cryogenic liquid is released on salt water. However, when cryogenic liquid is released on fresh water, there will be significant ice formation similar to the current experiment.

Another significant difference between sea water and fresh water is the convective heat from the water. The convective heat from water to cryogenic liquid is a buoyancy-induced flow produced by inhomogeneity of fluid density in the presence of gravity (Caldwell, 2006). This convective heat can be thermo-gravitational if the density variations are caused by changes of temperature (single diffusion) and thermohaline if the density inhomogeneity is caused due to both variations in temperature and salt content (double diffusion) (Caldwell, 2006).A release of cryogenic liquid on sea water can lead to convection which is both thermo-gravitational and thermohaline in nature. This phenomenon can lead to bubble formation due to rapid boiling and can eventually prevent or prolong the formation of ice.

### 5.4.2. Temperature Profile of Ice

The variation of ice temperature during the spill was analytically calculated from equation (33) and compared with experimental values at seven different depths, and the result obtained for experimental run 5 is shown in Figure 24. Similar temperature profiles were obtained for other experimental runs. The solid lines represent the temperature measured during the experiment and the dashed lines represent the predicted

temperatures. A good agreement was observed between the experimental and predicted temperatures. It is to be noted that the initial constant temperature profile of ice in this run (run 5) was an effect of the previous spill (run 4). The thermocouples placed near the top surface of ice (distance-0.3cm) recorded lower temperature values and as the distance from surface increased, the temperature values of thermocouples (distance-3.65cm) placed also increased. Also, the thermocouples placed near the top surface are cooled earlier than the thermocouples below, due to the release of liquid nitrogen. A deviation in predicted temperatures is observed after 750 seconds. This is likely due to the variation in thermal properties of ice with temperature, which is not accounted for in the model.

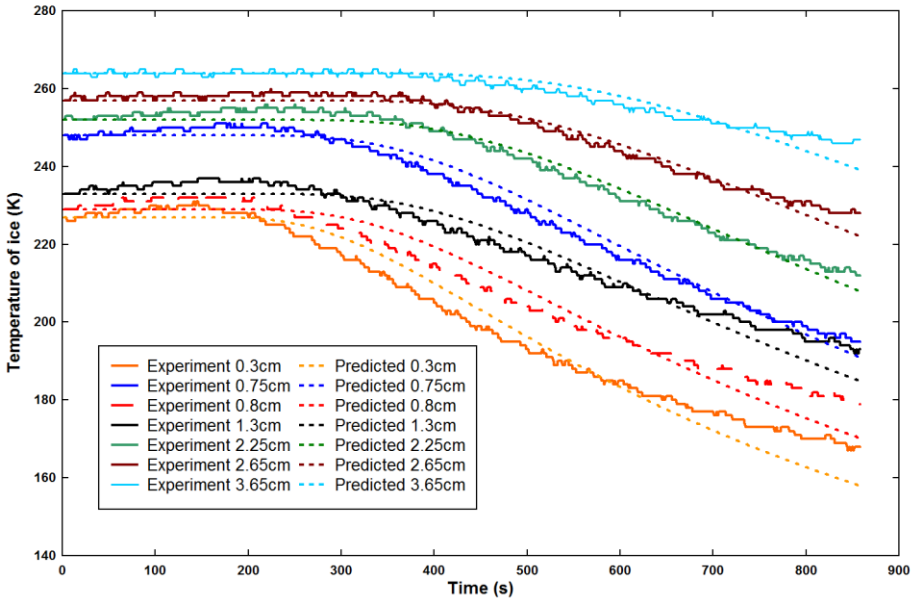


Figure 24. Temperature profiles of thermocouple below ice surface

### 5.4.3. Comparison of Experimental and Predicted Heat Flux with Respect to Time

A comparison of the predicted heat flux and experimental heat flux as a function of time is given for run 5 in Figure 25. The trend for one experimental run is shown here since all the experiments except run 2 followed similar trends. Figure 25 represents the comparison of predicted heat flux obtained from equation (33) and experimental heat flux with respect to time. The heat flux obtained from experiment was found to be varying above and below the predicted heat flux representing both under-prediction and over-prediction by the model. This is attributed to the averaging time which is used for determining the vaporization mass flux. However, the variations in the predicted values were comparatively low. Figure 26 represents the comparison of predicted heat flux obtained from equation (34) and experimental heat flux with respect to inverted square root of time. The results are in good agreement except for run 2. However, run 2 was a case where the liquid nitrogen was spilled on a mixture of ice and water, thus it cannot be appropriately modeled by conduction equations and is closer to convection phenomenon, like the spill on water.

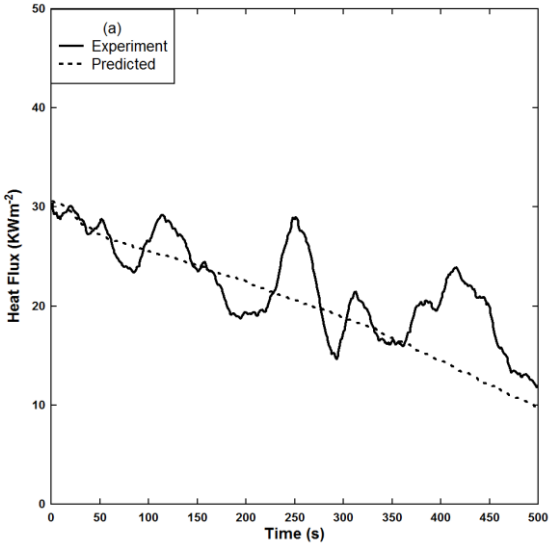


Figure 25. Comparison of experimental and predicted heat flux vs time for run 5

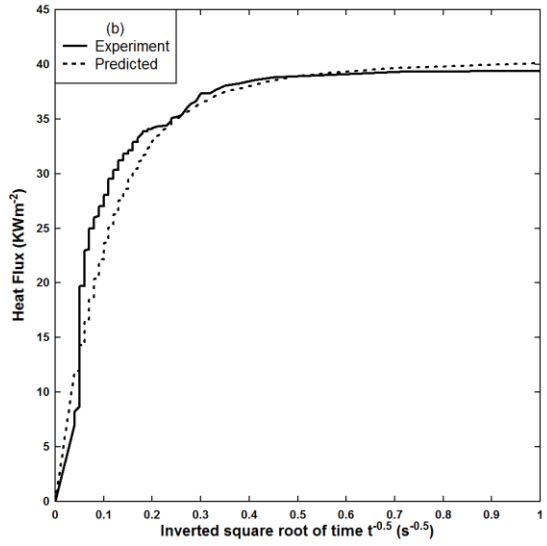


Figure 26. Comparison of experimental and predicted heat flux vs inverted square root of time for run 5

It is to be noted that the prediction model was based on the temperature values of ice recorded during the experiment whereas the experimental heat flux was obtained by taking the slope of the mass loss data. The fluctuations that arise in experimental heat flux ($q_e$) were different from fluctuations that arise in predicted heat flux ($q_p$). The determination of derived parameter heat flux involved primary measurable parameters like mass and temperature. Since the measurable parameters depend on the resolution of physical units, an error analysis was required to test the efficiency of the heat flux prediction model. Four error analysis correlations (Taylor, 1996) were chosen for this purpose and are they are listed below.

Mean Absolute Error, $MAE = \frac{1}{n}\sum_{i=1}^{n}|q_p - q_e|$ (36)

Mean Relative Error, $MRE = \frac{1}{n}\sum_{i=1}^{n}\frac{(q_p - q_e)}{q_e}$ (37)

Root Mean Square Error, $RMS = \sqrt{\sum_{i=1}^{n}\frac{(q_{e_i} - q_{p_i})^2}{n}}$ (38)

Standard Deviation Error, $SDE = \sum_{i=1}^{n}\frac{\left(q_{e_i} - \overline{q_{e_i}}\right)^2}{n}$ (39)

where 'n' refers to the number of measurements, 'i' refers to the ith measurement.

Table 9. Performance of prediction model

| Run Number | MAE ($kWm^{-2}$) | MRE (no unit) | RMSE ($kWm^{-2}$) | SDE ($kWm^{-2}$) |
|---|---|---|---|---|
| **Run 1** | 5.1 | 0.22 | 6.92 | 4.6 |
| **Run 2** | 13.4 | 0.15 | 16.2 | 9.3 |
| **Run 3** | 4.1 | 0.17 | 5.01 | 3.0 |
| **Run 4** | 5.6 | 0.21 | 7.6 | 5.2 |
| **Run 5** | 2.3 | 0.09 | 2.9 | 1.9 |
| **Run 6** | 5.5 | 0.3 | 6.3 | 3.1 |

A summary of errors obtained for all experimental runs is shown in Table 9. The Mean Absolute Error (MAE), Root Mean Square Error (RMSE) and Standard Deviation Error (SDE) were relatively low for all experimental runs except run 2. However, in run 2 the vaporization flux followed a decreasing trend as mentioned in section 4.1. This trend is characteristic of release on water rather than ice. This might have been due to the fact that, in run 2 liquid nitrogen contacted water more than ice due to high flow rate of liquid nitrogen causing a forceful discharge on the ice-water substrate. The Mean Relative Error was a measure of magnitude of error with respect to its true value which was the experimental heat flux. This difference can occur because of randomness or if a particular temperature measurement is selected to determine the heat flux resulting in sampling error. The Mean Relative Error is over 20% in Run 1, Run 4 and Run 5 representing the error propagated from thermocouples that were used to determine the heat flux. High Mean Relative Error was observed for almost all experimental runs due to the variation of physical properties of ice with temperature which was not attributed in the model. The variation in physical properties was noted to be rapid due to the two phase nature of cryogenic flows accompanied by turbulence. This variation introduced certain uncertainty and was treated using a detailed uncertainty analysis.

The uncertainty of dependent variables predicted and experimental heat flux can be determined as a function of variables influencing it (Bevington and Robinson, 2003). The uncertainty propagated to experimental heat flux $q_e$was estimated from the uncertainty of measured variables mass (m) and area (A). The propagation of error in the derived quantity heat flux was given by

$$\frac{\Delta q_e}{q_e} = \sqrt{\left(\frac{\Delta m}{m}\right)^2 + \left(\frac{\Delta A}{A}\right)^2} \quad (40)$$

The resolution of the weighing balance used in the present study is 0.1 kg. The uncertainty estimated in the variable, area was assumed to be 1%. The error propagated to experimental heat flux was ±8.6%. Similarly the uncertainty in predicted heat flux was a function of temperature. The uncertainty in predicted heat flux arises from measurements of temperature and variation of properties like thermal conductivity (k), density (ρ) and specific heat ($C_p$) with temperature given by

$$\frac{\Delta q_p}{q_p} = \sqrt{\left(\frac{\Delta T}{T}\right)^2 + \left(\frac{\Delta k}{k}\right)^2 + \left(\frac{\Delta \rho}{\rho}\right)^2 + \left(\frac{\Delta C_p}{C_p}\right)^2} \quad (41)$$

The N-type thermocouples were calibrated at temperatures 77, 238 and 308 K using liquid nitrogen (77 K) and silicone oil (238 and 308K) in a calibration bath. The temperature offset, which was the difference between reference temperature and measured temperature, was obtained using interpolation between three calibration temperatures. A Piecewise Cubic Hermite Interpolating Polynomial (PCHIP) method implemented in Matlab (version 7.0) with function "pchip" was used for calculating the offset. The uncertainty value of N-type thermocouple obtained from calibration is ±1.8 K for thermocouple measuring the ice temperature. The uncertainties associated with variation of properties like thermal conductivity, density and specific heat were found to be around 11%, 0.2% and 2.5% respectively. The total error propagated to the predicted heat flux was found to be around ±13%.

## 5.5. Case Study

For consequence analysis of real large-scale incident scenarios one should consider the different types of icebergs in the analysis. A general classification of different types of iceberg based on size is given in Table 8 (Diemand, 2001). A detailed classification of ice is available in sea ice nomenclature, which can be adopted for performing consequence analysis (Bushuyev, 1970). The classification takes into account different features of ice like origin, formation, salinity and size. Large icebergs are likely to be detected by radars installed in the ship or by airborne radars. However, the small icebergs are less likely to be detected by radars and hence they require special attention. Additionally, small icebergs with high thickness tend to prolong the vaporization time. This can cause the accumulation of flammable vapors near leak area. Hence a severe risk is associated with collision of ships with small icebergs like growlers and Bergy bits. Such cases account for rare events and should not be disregarded when modeling incidental scenarios. Once the type of iceberg is chosen, appropriate properties of iceberg (size, temperature, physical properties) can be included in the model for determining the vaporization rates.

A case study is undertaken to model the collision of LNG moss type carrier on a Bergy bit iceberg of diameter 10 m and height 1m. A prognostic analysis is carried out to critically analyze the pool spreading and vaporization behavior of LNG. The pool spreading and vaporization of LNG is modeled using FLACS pool model (Melheim *et al*., 2009). The model is based on two-dimensional shallow water equations which assume that the pool thickness is smaller than its horizontal dimensions. The realistic

scenario involves a collision where the volume of one moss sphere tank in the LNG carrier is damaged due to collision. The pool is assumed to be radial initially and is bound to spread in the space between the carrier and iceberg. The details of the scenario and the iceberg properties are provided in Table 10.

Table 10. Input parameters of FLACS simulation

| Parameters | Value |
|---|---|
| **LNG flow rate** | 10 kg/s |
| **Spill Duration** | 100 s |
| **Density of ice** | 980 kg/ $m^3$ |
| **Thermal Conductivity of ice** | 2.18 W/mK |
| **Thermal diffusivity of ice** | 0.000002 $m^2$/s |
| **Temperature of ice** | 268 K |

Figure 27 shows the pool spreading of LNG at various time intervals. The image sequence shows the growth of pool following a leak due to collision. The pool grows radially initially and then spreads out in lateral directions with further addition of LNG into the pool. The concentration of the LNG was found to be greater near the leak source as expected. The purpose of CFD analysis is to model the obstruction of pool spreading by iceberg. This is well captured by FLACS.

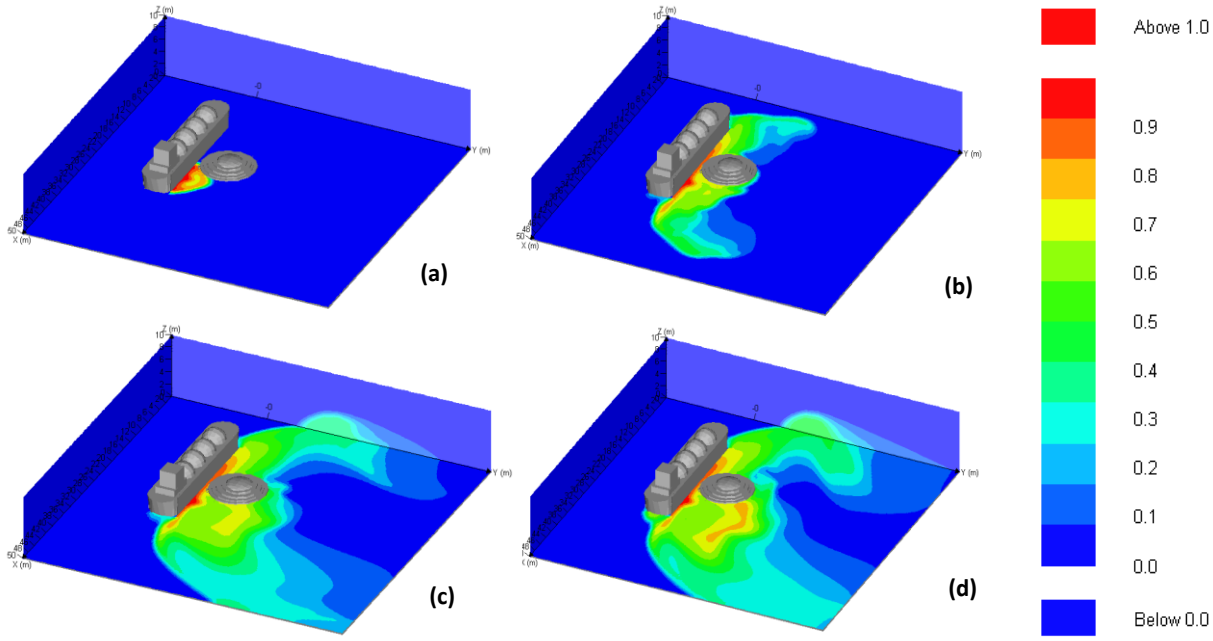


Figure 27. Mole fraction of LNG at time (a) t=5s (b) 30 s (c) 50 s and (d) 100s

The vaporization mass flux determined from FLACS simulation is compared with vaporization mass flux obtained from 1D conduction model (equation (33)) for the similar input conditions as FLACs and is presented in Figure 28. The vaporization mass flux from CFD simulation and 1D conduction model had a similar trend; however, the initial vaporization mass flux of FLACS model was found to be higher than the one dimensional conduction model. The initial vaporization mass flux was found to be high for both the cases. However, as time proceeds, the conduction model predicts a vaporization rate that is 50% greater than the FLACS simulation. However, after a time period of 40s, the predictions by both FLACS and conduction model are found to be similar.

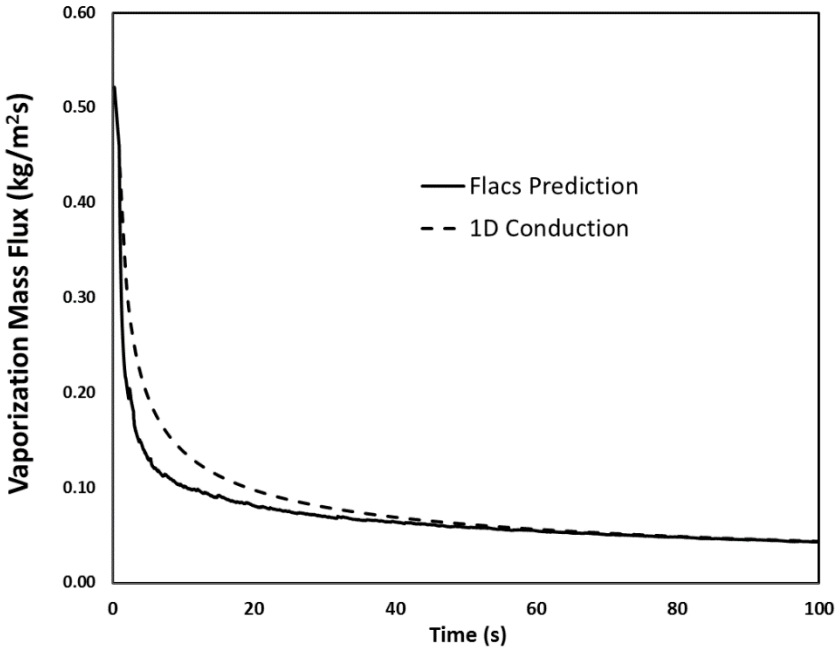


Figure 28. Comparison of FLACS CFD simulation with 1D prediction model

## 5.6. Conclusion

An experimental investigation of small-scale releases of liquid nitrogen on ice was performed to improve the understanding of the source-term modeling of cryogenic liquid spilled on ice. The experiment reflected a scenario of collision of an LNG carrier on an iceberg, leading to a cryogenic liquid release on ice. The vaporization mass flux obtained was independent of the amount of liquid nitrogen spilled, and as expected, was a function of the release rate and ice temperature. When the release rate and ice temperature was high, the vaporization mass flux follows a decreasing trend. With further reduction in release rate and ice temperature, the vaporization mass flux was found to be independent with time. This decreasing trend can be attributed to rapid decrease in temperature difference between ice and liquid nitrogen during the

vaporization process. Once the ice substrate temperature equalizes the cryogenic liquid pool temperature, constant vaporization mass flux is obtained.

The vaporization mass flux was also found to be weakly dependent on ice thickness. Increased ice thickness lead to significant resistance in conduction heat transfer. A very good prediction agreement of the temperature inside the ice obtained by 1D ideal conduction model was observed. The performance of the theoretical model in predicting heat flux for the release on ice was found to be good, but not for the ice-water mixture. The phenomenon of release of liquid nitrogen on ice-water mixture is more representative of spill on water. The heat to liquid nitrogen in such cases was supplied by both water and ice through convection and conduction respectively. A prognostic analysis using CFD was performed to model the collision of LNG carrier on a Bergy bit iceberg. The trend is vaporization mass flux using CFD techniques and 1D conduction model was found to be similar. However, over-prediction was observed in 1D conduction during initial vaporization stages.

# CHAPTER VI

# QUANTIFICATION OF TURBULENCE IN CRYOGENIC LIQUID[3]

## 6.1. Introduction

The quantification of turbulence in the cryogenic liquid pool, when it comes in contact with water, is an important step in LNG source-term modeling. Recent modeling approaches involve Computational Fluid Dynamics (CFD) codes with different types of turbulence models to perform various aspects of LNG consequence analysis. In spite of the increasing use of turbulence parameters in CFD, only a few researchers have tried to quantify the turbulence characteristics through experiments. One of the early attempts made to quantify turbulent intensity of vaporizing LNG was through analysis of video images of experiments (Gavelli, Chernovsky, Bullister, and Kytomaa, 2009). In this study, the spreading velocity of the pool was utilized to quantify the turbulent intensity. In another study, the effect of water turbulence on the cryogenic liquid was studied by varying the turbulent intensity of the water (Morse and Kytömaa, 2011). This approach was classified as free-surface turbulence and it utilized a controlled jet velocity of water in its study. Their study concluded that the vaporization rate was dependent on the height of cryogenic liquid. However, the underlying mechanism for the dependence of height on vaporization rate was not completely understood. A theoretical study was also performed based on a parameter called turbulence factor which was used to model the instability of the thermal film when LNG contacted water (Hissong, 2007). The

[3] Reprinted with permission from "Quantification of turbulence in cryogenic liquid using high speed flow visualization" by Gopalaswami, N., Laboureur, D. M., Mentzer, R. A., & Mannan, M. S. Journal of Loss Prevention in the Process Industries, copyright [2015], Elsevier

turbulence factor reflected the turbulence produced in water due to an LNG spill and was given by the ratio of heat transfer coefficient between water and LNG to the heat transfer coefficient of quiescent water from correlations. Most of work done by researchers was focused on turbulence generated in water. It should be noted that there is the presence of bubbly vaporization even when LNG is spilled on still water. However, the question remains as to whether turbulence, characterized by bubbly vaporization of cryogenic liquid, arises due to water or cryogenic liquid. Despite numerous theoretical models for pool spreading and vaporization, the number of models accounting for turbulence that is associated with vaporization is less. This is attributed to the fact that turbulence is a complex three dimensional phenomenon and it is difficult to develop and incorporate a turbulence model in pool spreading and vaporization models. In addition to it, the nature of turbulence structures that is present inside the cryogenic liquid during vaporization is yet to be studied. Overall, this paves the way to determine sub-grid scale turbulence and examine its effect on vaporization.

## 6.2. Objectives

The main objective of this phase of research study is to investigate the turbulence generated during cryogenic liquid vaporization process. The purpose of the study is to describe a comprehensive and quantitative characterization of velocity and turbulence measurements of cryogenic liquid boiling on water. To achieve this, a high speed flow visualization technique is used to quantify the interfacial turbulence in the boiling phenomenon. Based on the experimental results, image analysis techniques are used to obtain the velocity components. From the velocity measurements turbulence parameters

are determined from correlations. In the end, the interaction of the turbulence structures in the underlying flow field is investigated, which is important for understanding the turbulent effects on heat and mass transfer between water and cryogenic liquid.

## 6.3. Flow Visualization Experiment

### 6.3.1. Flow Visualization Setup

The general experimental arrangement for flow visualization is presented in Figure 29. The flow visualization set-up consisted of a high speed camera (Photron SA 5) capable of frame rates up to 150,000 frames per second. The camera was operated at a frame rate of 5000 frames/s and a shutter speed of 1/6000 seconds to provide a video of 4.37 seconds in each experimental run. The camera had an integrated personal computer, which was used to control the capture and storage of images. Front-end software called Photron Fastcam Viewer (PFV) captured the camera images and stored the information in the computer for image processing. The input parameters were speed of capture (frame rate), shutter speed of the camera and number of frames for storage after triggering the capture. A backlighting technique was used during the data acquisition stage to illuminate the liquid and vapor phases of cryogenic liquid appropriately. The advantage of this technique was that it provided high light intensity, which was needed for extremely short shutter times and high frame rates. The illumination source was provided by a tungsten lamp (60 W) operating with a light capacity of 900 lumens and luminous efficacy of 15 lumens per watt. The light from the lamp was diffused through an optical filter placed between the illumination source and test section to spread the high intensity light evenly on the region of influence.

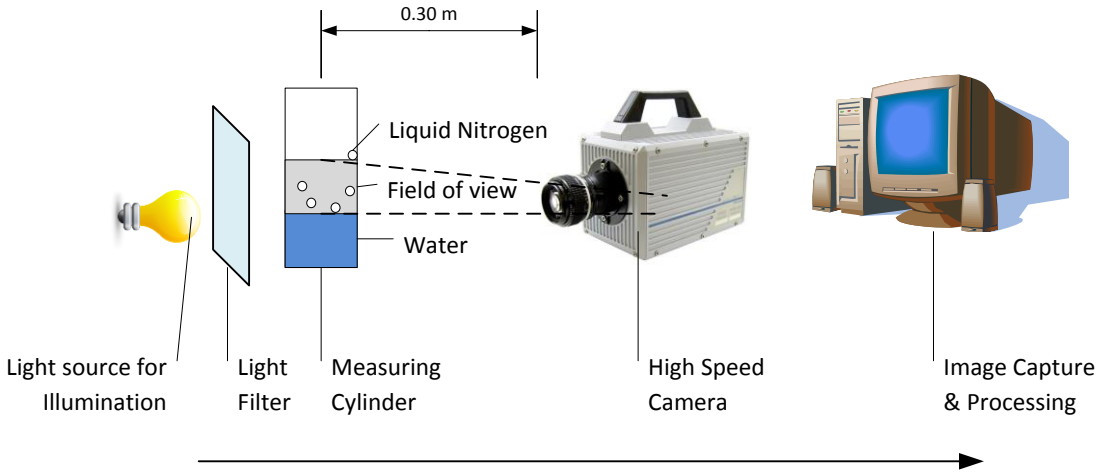


Figure 29. Experimental setup for high speed flow visualization

### 6.3.2. Test Conditions

The test section consisted of a 100 ml cylinder with a height of 24 cm and inner diameter of 2.7 cm. The cylinder was filled with 35 ml of water before the start of the experiment. In each experimental run, a known quantity of liquid nitrogen ($LN_2$) was poured instantaneously (~0.5s) and the camera was triggered. The water was quiescent before liquid nitrogen ($LN_2$) was poured into the setup. The $LN_2$ was poured at the top of the measuring cylinder at every run. This is equivalent to a distance of 24 cm elevation from the base of the setup. The spill was performed manually and was restricted to a consistent duration of less than 0.5s in all the runs. A total of 21,850 images with a maximum resolution of 1024x1024 pixels were produced in each experimental run. The field of view was centered on the water-cryogen interface in all experimental runs. The experiment was repeated by spilling different amounts of liquid nitrogen on water. A summary of experiments and key results is provided in Table 11. The initial water

temperature and cryogenic liquid height were varied in the experiment. These constitute the independent variables. The turbulence parameters were found to be influenced by the independent variables and they are considered as primary dependent variables. The vaporization flux is dependent on both independent variables and primary dependent variables (turbulence parameters) and is considered as secondary dependent variable. An additional note on salt content is included to denote its influence on ice formation.

Table 11. Summary of flow visualization experiment

| Run No | Water level (cm) | Water Tempe-rature (˚C) | Amount of $LN_2$ Spilled (ml) | $LN_2$ ht (cm) | Avg. TI (%) | Avg. TKE ($m^2/s^2$) | Avg. EDR ($m^2/s^3$) | Avg. Vap. Flux ($kg/m^2s$) |
|---|---|---|---|---|---|---|---|---|
| 1 | 6.3 | 17.2 | 7.25 | 1.25 | 33.2 | 0.006 | 0.001 | 0.044± 0.0003 |
| 2 | 6.3 | 15.5 | 7.5 | 1.35 | 27.4 | 0.007 | 0.002 | 0.066± 0.005 |
| 3 | 6.3 | 21.1 | 8.25 | 1.45 | 22.6 | 0.008 | 0.001 | 0.12± 0.009 |
| 4 | 6.3 | 15.5 | 18.5 | 3.25 | 14.3 | 0.009 | 0.001 | 0.15± 0.012 |
| 5 | 6.3 | 17.2 | 20 | 3.5 | 15.8 | 0.005 | 0.001 | 0.081± 0.006 |
| 6 | 6.3 | 17.2 | 22 | 3.6 | 11.0 | 0.007 | 0.002 | 0.23± 0.018 |

## 6.4. Image Processing and Analysis

To quantitatively study the turbulence generated by the boiling of the cryogenic liquid on water, the high speed images were processed using the Large-Scale Particle Induced Velocimetry (LS-PIV) technique (Laboureur, Aprin, Osmont, Buchlin, and Rambaud, 2013). This technique allows the calculation of the flow velocity from an

image pair using algorithms developed for Particle Image Velocimetry (PIV). The traditional PIV technique consists of introducing small particles in the flow to illuminate them with a laser sheet. A couple of successive images at two different instants are then taken with a camera. The velocity is then computed through the estimation of the displacement between the two images, using cross-correlation methods. In the LS-PIV technique, no particles are added to the flow, but the velocity is computed by tracking the movement of large structures instead of individual particles. In this study, the PIV algorithms developed by Thielicke and Stamhuis in Matlab, called 'PIVlab' were applied for image analysis (Thielicke and Stamhuis, 2010). Prior to the analysis, the recorded images were cropped to the region of interest, and the Contrast Limited Adaptive Histogram Equalization (CLAHE) method was applied to the raw images to enhance the contrast between the object and the background (Zuiderveld, 1994). A digital masking technique (Gui, Merzkirch, and Fei, 2000) was also applied to generate a mask for unwanted structures ,like ice and glass, present in the field of view and subtract them from the rest of the images. Additionally, this technique also helped to remove any optical distortions due to the rounded cylinder that is used in this experiment.

The PIV algorithm consists of dividing each pair of images in interrogation windows. The FFT based cross-correlation was applied on each window to determine the most probable spatial displacement (Thielicke, 2014). The interrogation window size was initially fixed to be 32×32 pixels in the first pass and then was reduced to 16×16 pixels in the second pass. For each pass, 50% overlapping and adaptive interrogation window shift was applied. This technique increases data resolution and accuracy that is

required for the cross-correlation calculation. The 21,850 images of each test were divided in batches of 500 images, and a non-overlapping image sequencing (1-2, 3-4,..) was chosen for each run of image processing. The calculated velocity fields were then post processed to remove the improperly matched vectors. The FFT based cross correlation algorithm selects the best match of spatial displacement from the images. Other FFT correlation peaks like second best displacement peaks which are not considered by FFT algorithm become the improperly matched vectors. First, a scatter plot was drawn with the displacements obtained in both the x and y directions. A sample scatter plot is shown in Figure 30. A rectangular box is circumscribed over the area with the highest accumulation of displacement peaks (velocity vectors). The rectangular box is chosen in such a way that the entire cluster is covered by the box. All displacement peaks (velocity vectors) lying outside the rectangle(s) are marked and rejected. Second, only the vectors with a signal-to-noise ratio (SNR) over 3 are considered in this study for a good determination of displacements (Lazar, Deblauw, Glumac, Dutton, and Elliott, 2010). SNR is the ratio of the highest peak to the second highest peak in each individual correlation map. Finally, a median filter is applied to the vector field to remove the outliers by detecting the vectors that significantly deviate from their neighboring vectors. A threshold value of 0.1 pixel was chosen for the corresponding displacement data to check for the deviation of vectors.

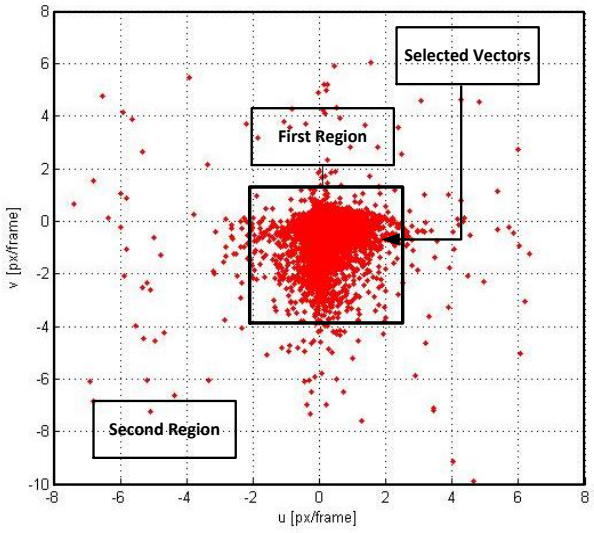


Figure 30. Scatter-plot of velocity vectors

## 6.5. Accuracy and Resolution

An uncertainty analysis was performed in which several important and analyzable factors of image processing were quantitatively investigated. The total uncertainty consists of uncertainty arising from calibration, image detection and displacement, flow visualization experiment and the number of frames chosen for analysis.

The error arising from calibration and experiment was obtained from the velocity field. The high-speed camera detects the flow speed by means of the displacement of thermal convection currents Δx, and the time interval between successive images Δt. The velocity flow field was based on this digitized image. The information captured in the image is different from the actual experiment due to projection of 3-D phenomenon on a 2-D image. This was expressed by the parameter $d$ and it contributes to error in the

experiment. The velocity field obtained by high speed camera is obtained from (Park, Derradji-Aouat, Baoshan, Nishio, and Jacquin, 2008) and is given by

$$u = \alpha\left(\frac{\Delta X}{\Delta t}\right) + d \quad (42)$$

for u-mean velocity, d-projection displacement, while α is the magnification factor. The magnification factor α was determined using the calibration present in the measuring cylinder. This is representative of the speed of the flow. The calibration present in the measuring cylinder was used to determine the magnification factor. The distance between measuring cylinder and camera ($L_r$), distance between two points in the image ($l_r$) and the angle between camera and cylinder (θ) were obtained from (Park *et al*., 2008) and were used to determine the magnification factor given by,

$$\alpha = \frac{l_r\left(1-\frac{\theta^2}{2}\right)}{L_r} \quad (43)$$

The value of $L_r$, $l_r$ and θ in the experiment was 0.3m, 3μm and zero respectively. The magnification factor, α, was determined to be $1x10^{-4}$.

The error due to data processing arises from the FFT based cross-correlation method and the pixel size that was applied for displacement determination. The uncertainty band of the pixel size was estimated statistically, and it was set to be less than 0.1 pixels in the image processing step. The uncertainty associated with FFT based cross-correlation was obtained by sub-pixel analysis using 2-D Gaussian fitting method. The sub-pixel size was varied from 64 pixels to 32 pixels and 16 pixels and the number of passes was varied from 3 to 1 to obtain the uncertainty. This contributes to an error of

0.3 pixels. The total uncertainty associated with data processing amounts to 0.4 pixel (0.1+0.3 pixel).

The uncertainty associated with number of frames was obtained by performing a sensitivity analysis. The number of frames chosen for batch processing was varied from 500, 1000 and 1500 to identify the effect of the number of image pairs on the analysis. The mean velocity profiles are compared and relative difference between the velocities is noted to be around 0.03 pixel.

The total uncertainty was obtained by combining the individual uncertainties and was provided by the Kline McLintock method (Kline and McClintock, 1953) expressed generally as

$$u_c = \sqrt{\left[u_\alpha \left(\frac{\partial u}{\partial \alpha}\right)\right]^2 + \left[u_{\Delta x} \left(\frac{\partial u}{\partial \Delta x}\right)\right]^2 + \left[u_n \left(\frac{\partial u}{\partial n}\right)\right]^2 + \left[u_d \left(\frac{\partial u}{\partial d}\right)\right]^2} \quad (44)$$

where $u_\alpha$, $u_{\Delta x}$, $u_n$ and $u_d$ are the uncertainty and $\left(\frac{\partial u}{\partial \alpha}\right)$, $\left(\frac{\partial u}{\partial \Delta x}\right)$, $\left(\frac{\partial u}{\partial n}\right)$ and $\left(\frac{\partial u}{\partial d}\right)$ are the sensitivity coefficients associated with magnification, data processing, number of frames chosen for analysis and experiment respectively. Table 12 provides a summary of different categories of error, uncertainty and sensitivity coefficient of parameters contributing to uncertainty. The total uncertainty associated with this study is determined from equation (35) and is found to be 8%. Similar values for uncertainty were obtained by Park *et al*. (2008). The values of uncertainty are expected to be lower for actual laser induced PIV techniques (Zhou, Doup, and Sun, 2013) due to high precision of lasers.

Table 12. Summary of uncertainty analysis

| **Parameter** | **Category** | **Uncertainty ($c_i$)** | **Sensitivity Coefficient ($\partial u \backslash \partial c_i$)** | **$((c_i)(\partial u \backslash \partial c_i))^2$** |
|---|---|---|---|---|
| $\alpha$ | Magnification Error | 0.04 (pix) | 200 (mm/pix$^2$) | 64 |
| $\Delta X$ | Data Processing (mismatching and sub-pixel analysis) | 0.4 (pix) | 2 (mm/pix$^2$) | 0.64 |
| $n$ | Number of frames for analysis | 0.03 (no unit) | 1 (no unit) | 0.0007 |
| $\delta u$ | Experiment | 0.04 (no unit) | 1 (no unit) | 0.0016 |

## 6.6. Results and Discussion

### 6.6.1. Qualitative Analysis of Flow Field

When a cryogenic liquid is released on water, there is a large gradient of temperature or heat flux which leads to turbulent convection. The convective heat provided by water is transported upward by molecular motion and small turbulent eddies (Tsinober, 2009). There are two interfaces that are observed in this process (Figure.31). The first interface is formed by $LN_2$ and water (water-cryogenic liquid) and the other interface is formed by $LN_2$ and air (cryogenic liquid-air). Since the temperature difference between $LN_2$ and water is high (> 180K) immediately after spillage, the energy supplied is also high. As the incoming energy to the cryogenic fluid is large, the temperature in the water-$LN_2$ interface increases and convection currents arise from the heated contact layer. Additionally, the convection currents traversing from the water-$LN_2$ interface to the $LN_2$-air produces agitation in the $LN_2$ liquid pool which accounts

for the turbulence. This is typically characterized as interfacial turbulence occurring due to thermal convection (Colinet *et al.*, 2003), (Okhotsimskii and Hozawa, 1998).

In every experimental run, it was observed that wavy patterns of liquid arise from the water-cryogenic layer interface and travel up to the cryogenic–air interface. This object, called 'thermals', was found to be important in the vaporization process. The thermal plumes (thermals) occur when the bottom of the liquid is heated, which drives the hot fluid away from the hot surface and allows colder fluid to be replaced in the region near the water surface (Tsinober, 2009). The thermals occur periodically and successive thermals follow the same path as their predecessors. The thermals were found to have varying kinetic energy levels. Inside the cryogenic liquid, it was observed that the thermals arising from water-cryogenic liquid layer interface were well identified by a zone of high kinetic energy. High energy thermals were formed during the initial stages of boiling and they traverse with high kinetic energy to the cryogen-air interface. This energy level in the thermals declines with time causing dissipation of its energy within the cryogenic liquid layer. These thermals act like a catalyst in increasing the heat transfer and turbulence associated with the cryogenic liquid. As the thermals traversed the cryogenic liquid pool, their energy is reduced and breakdown occurred on the $LN_2$-air interface into the atmosphere. The breakage of the convection current at the $LN_2$-air interface led to the formation of vapor. An image of the cryogenic vapor bubble and thermal produced inside the cryogenic liquid is presented in Figure 31.

Initial experimental runs involved release of $LN_2$ at different heights to allow penetration of $LN_2$ into water. Liquid nitrogen was found to be highly immiscible and

lighter than water. When $LN_2$ was poured into water, it traced back to the surface in less than 5-7 milliseconds due to its immiscible nature. Analysis of those initial experiments revealed that the amount of turbulence in the initial stage, due to injection of cryogenic liquid jet was relatively less. The turbulence parameters (TI,TKE and EDR) were two orders of magnitude lesser than the average values observed in runs where jet penetration was not present (Table 11 values). It is also worthwhile to note that bubbly vaporization is observed even when $LN_2$ was poured on the surface of quiescent water. The turbulence phenomenon predominantly arose due to the vaporization process rather than the jet penetration into water. This can be observed from Figure.32 where $LN_2$ jet does not mix with water, however, pushes the water and traces back immediately to the surface. Due to this reason, the effect of elevation and penetration of $LN_2$ jet into water was not considered for subsequent experimental runs reported in this study.

It was also noted during analysis that ice formation did not occur when deionized water was used in run 2. This was attributed to the fact that the convective heat from water is thermohaline in nature. Thermohaline changes occur when the density inhomogeneity within the liquid is caused by temperature and compositional gradients (double diffusion) (Caldwell, 2006). The ice formation was thus associated with the salt content and impurities which provide a compositional gradient in the water-$LN_2$ interface. Since this phenomenon was observed during the analysis stage, rather than the experimental stage, the effect of salt concentration on turbulence parameters and vaporization process could not be studied through experiments.

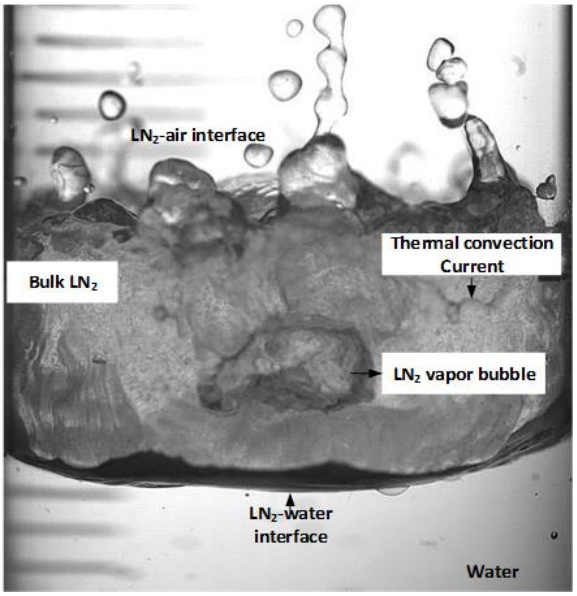


Figure 31. High speed image showing vapor bubble and thermal convection current inside liquid nitrogen

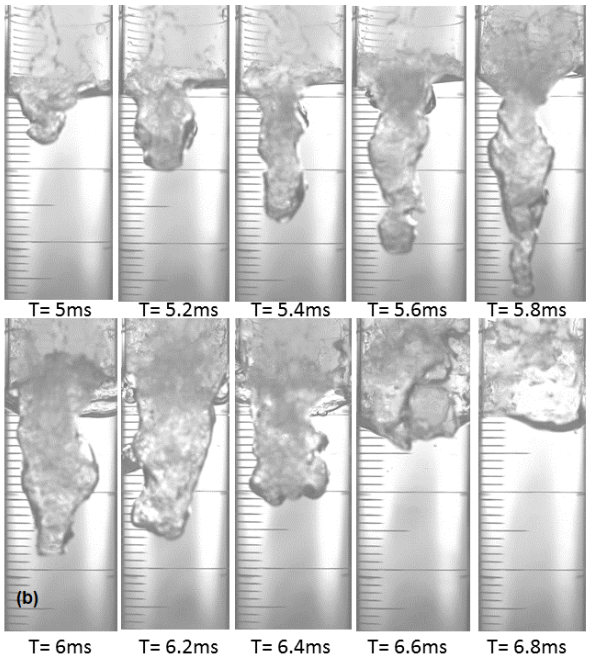


Figure 32. Liquid nitrogen jet penetration and retraction in water

### 6.6.2. Quantitative Characterization of Flow Field

An image sequence of thermal trajectory in the cryogenic liquid from high speed camera and Matlab image analysis is shown in Figure.33. The images were expressed for a time period of 20 milliseconds (ms). The spatiotemporal propagation of the thermals expressed as instantaneous velocity (M) in Matlab agrees well with the observations from high speed video camera. On the high speed digitized image, the thermals and cryogenic liquid appeared as different patterns. The cryogenic liquid appeared stationary with thermals moving with a velocity of $0.9\pm0.1$ $ms^{-1}$ through the bulk phase of the liquid. This difference in velocity between cryogenic liquid and thermals allows automatic detection of velocity magnitude. Similar to the current study, Fdida *et al* performed velocity measurement of bubbles in liquid nitrogen using Laser Doppler Velocimetry (LDV) (Fdida *et al*., 2010). He had compared LDV techniques with Particle Tracking Velocimetry (PTV) and high-speed imaging. The vertical velocity profile obtained by Fdida *et al* were in close agreement with the current values and was found to vary from $0.1\pm0.02$ m/s for time duration of 5ms.

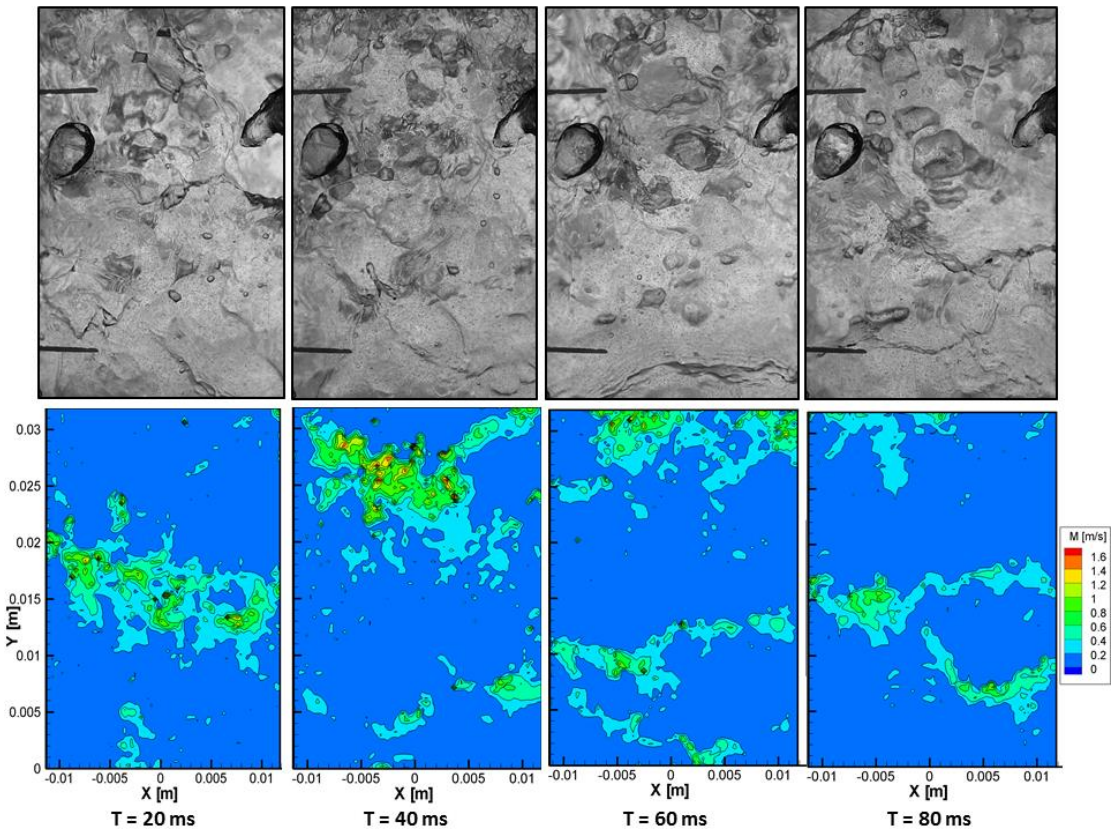


Figure 33. Image sequence of thermal and bubble trajectory. top: high speed images, bottom: velocity field from image processing

The vertical and horizontal components of the velocity were analyzed in order to characterize the evolution of the turbulence in the cryogenic liquid. A series of 500 images were processed at one run to obtain the horizontal and vertical velocity components 'u' and 'v'. A total of 43 batches, each containing 500 images, were processed similarly to obtain the velocity components. The velocity components u and v and overall velocity magnitude obtained from raw experimental data are provided in Figure 34(a), Figure 34(b) and Figure 34(c). The average flow field for run 2 is provided

in the vector plot Figure 34(d). The vector plot provides the spatial variation of velocity inside the cryogenic liquid. The magnitude of horizontal velocity was found to be low and it varied from 0.01 to 0.04 m/s. The lateral movements of thermals contribute significantly to the horizontal velocity. This horizontal component of velocity was observed to decline gradually with time. The vertical velocity component was two times the magnitude of horizontal velocity component for all runs and follows similar flow field behavior for all investigated turbulence cases. This was mainly attributed to the spatial movement of thermals in the upward direction. The overall velocity magnitude was found to decrease gradually with time and the overall velocity magnitude was found to vary between 0.04 to 0.10 m/s.

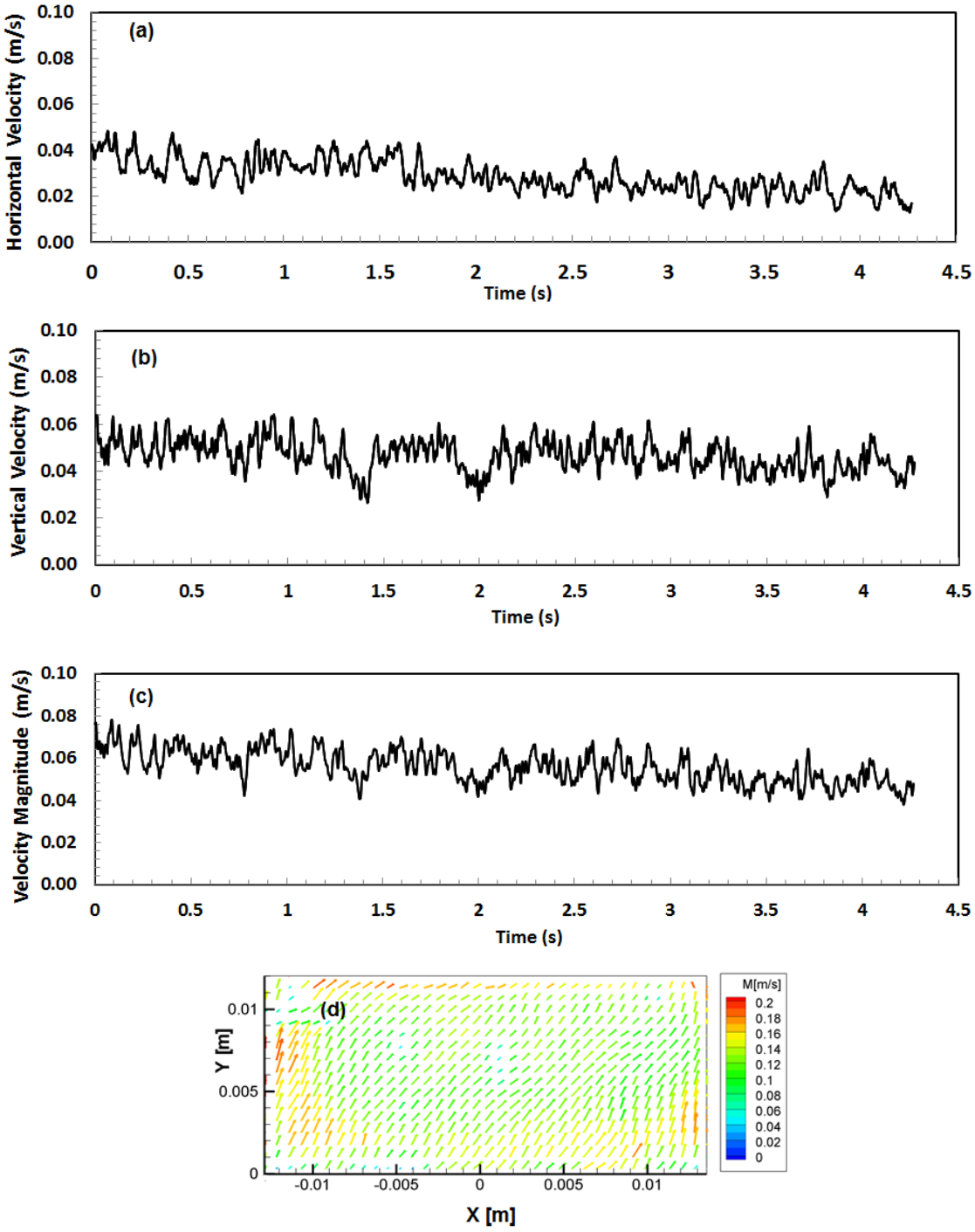


Figure 34. Time evolution of (a) horizontal velocity profile (b) vertical velocity profile (c) velocity magnitude (d) average velocity of the flow from image processing for Run 2

### 6.6.3. Turbulent Intensity

Turbulent intensity is an important parameter to understand the magnitude of turbulence inside the cryogenic liquid. The turbulence parameters were assumed to be isotropic and homogeneous in nature. This means that there are no spatial gradients involved in the mean velocity and the velocity fluctuations are similar in all directions. The turbulent velocity fluctuations in the axial and vertical directions were accounted for when calculating the turbulence parameters. The turbulent intensity (I) was defined as the ratio of root mean square velocity fluctuations to the mean flow velocity.

The Root mean square velocity ($u_{rms}$) is given by

$$u_{rms} = \sqrt{(u'^2 + v'^2)} \tag{45}$$

where u' and v' are the velocity fluctuations in x and y directions respectively.

The mean velocity is expressed as

$$\bar{U} = \sqrt{u^2 + v^2} \tag{46}$$

where u and v represent the horizontal and vertical velocity.

Turbulent intensity or the turbulence level is given by

$$I = \frac{u_{rms}}{\bar{U}} \tag{47}$$

where $u_{rms}$ is the root mean square of the turbulent velocity fluctuations and $\bar{U}$ is the mean velocity.

The mean flow velocity is obtained as an ensemble average of 500 images. The velocity fluctuations in the lateral and vertical directions provide an insight on the rate of fluid being transferred from one phase to another. Additionally, the vertical velocity

profile provided the dynamics of thermals for assessing the rate of mixing in heat transfer.

The turbulent intensity evaluated from the image visualization analysis for all runs is presented in Figure 35. The figure shows the time series averaged on a 60s basis to widen the trend observed in the turbulent intensity parameter. The initial turbulent intensity was found to be over 20% for all the runs. From the analysis, it was observed that the average turbulent intensity decreased with the increase in liquid nitrogen height. For runs 4 and 5 where the initial height of cryogenic liquid was 3.25 and 3.5 cm respectively, the turbulent intensity fluctuated between 10 and 20%. For runs 1 and 2 where the liquid nitrogen initial height was around 1.25 cm and 1.35 cm, the turbulent intensity was found to be higher than runs 4 and 5. The magnitude of turbulent intensity in these runs varied from 20 to 30%. When the height was low (<2cm), the thermals with high energy traveled a shorter distance from the water-$LN_2$ interface to the $LN_2$-air interface. Due to this reason, the amount of heat dissipated during the thermal trajectory was reduced. This was reflected as high intensity in these runs. In run 3, although the average turbulent intensity was around 20%. Sudden overshoots with turbulent intensity rising to ~50% was observed. This was typically two times the average turbulent intensity. A detailed analysis of the images revealed that the overshoots were caused due to collision of thermals with one another causing significant changes to the velocity components. The overshoots were also caused due to breakage of thermals in the $LN_2$-air interface causing cryogenic liquid droplets to rise above the liquid level and vaporize. These overshoots were observed in all runs and found to be influenced by the initial

water temperature. However, the overshoots were pronounced when the initial temperature of water is high. This is visually observed in Figure 35 for run 3. When the water temperature was high, the frequency of thermal production with varying energy increased. For run 3, the turbulent intensity is expected to be less than run 2 owing to the increase in cryogenic liquid height. However, a higher turbulent intensity is produced due to higher initial water temperature. The overshoots were found to be low when the initial temperature was low (<15˚C). For runs 4 and 5 with similar cryogenic liquid height, run 5 is expected to have a turbulent intensity less than run 4. However, since the initial water temperature was higher in run 5 when compared to run 4, the resulting overall turbulent intensity in run 5 was higher than run 4. On the whole, the turbulent intensity was found to decrease with increase in initial cryogenic liquid height. For runs with similar cryogenic liquid height, the turbulent intensity was greater for runs with higher initial water temperature.

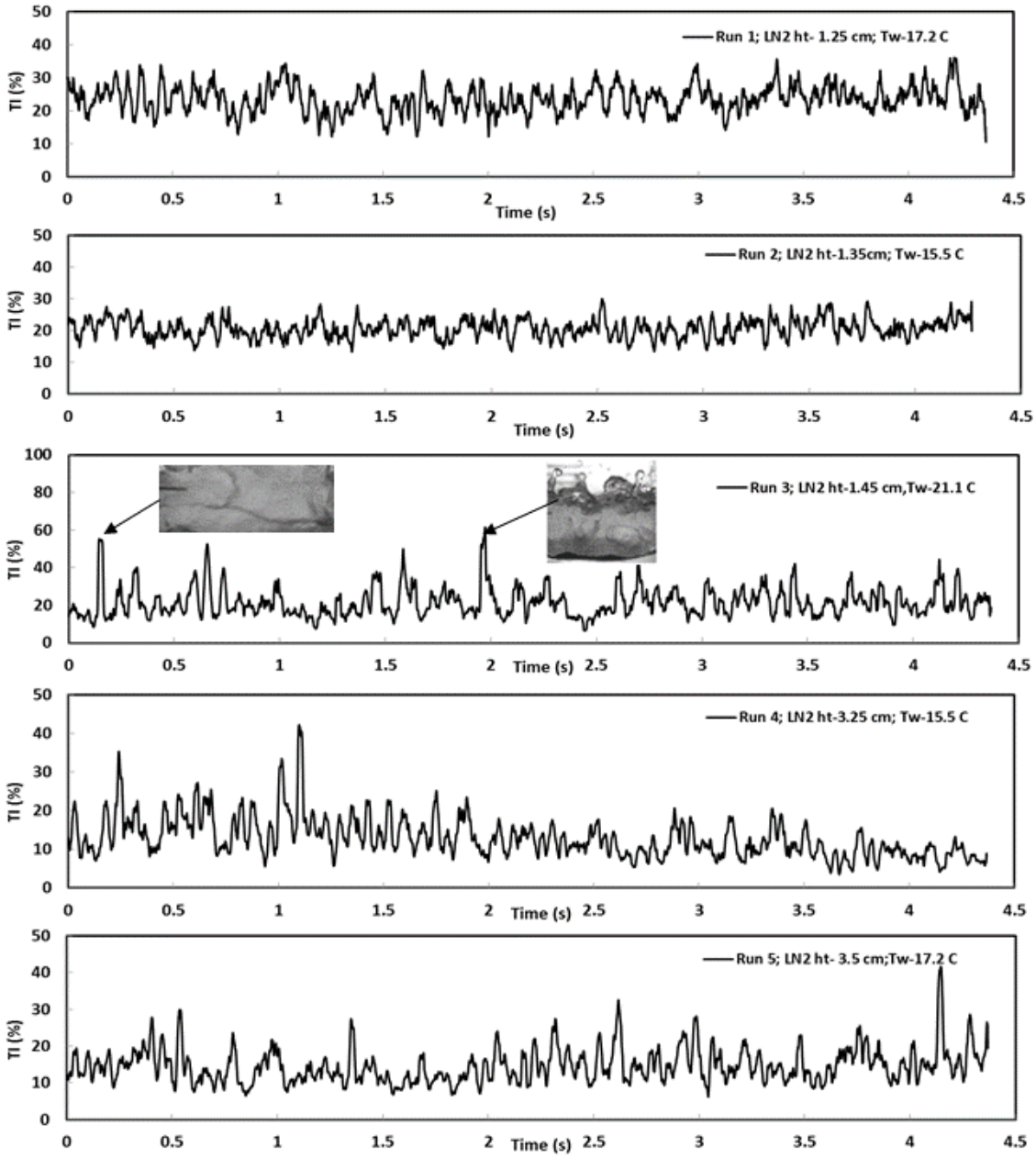


Figure 35. Turbulent Intensity (TI) profiles

### 6.6.4. Turbulent Kinetic Energy

The turbulent kinetic energy is a key indicator of the energy produced in the vaporization process. The turbulent kinetic energy increased when a thermal or a cryogenic bubble traversed through the cryogenic liquid. This was due to the increase in shear and production of wakes during passage. In order to predict the correct turbulent flow field, it was important to capture the energy generated by these turbulent structures such as buoyant thermals inside the cryogenic liquid. This was utilized to provide information on the development of turbulence along the cryogenic layer. It is also worthwhile to note the importance of turbulent kinetic energy as it is widely applied in standard CFD turbulence models like k-ε models. As the thermals rose from the water–cryogenic liquid interface, the kinetic energy was high due to the large temperature difference between the two liquids. As they traversed through the cryogenic liquid, they dissipated energy in the form of heat and the turbulent kinetic energy became more stable.

The TKE is determined as the mean of velocity fluctuations and is expressed as

$$k = \frac{1}{2}(u'^2 + v'^2) \quad (48)$$

The turbulent kinetic energy profiles for different runs are presented in Figure 36. The turbulent kinetic energy typically varied from 0.004 to 0.01 $m^2/s^2$. The variations in turbulent kinetic energy showed a weak dependence with the initial water temperature. The kinetic energy was found to be low when the initial water temperature was low (<20˚C). The low temperature of water resulted in low energy supply to the thermals. This is observed in runs 1 and 5. Runs 1 and 5 were relatively similar and the average

turbulent kinetic energy varied from 0.006±0.01 $m^2/s^2$. However, for run 3, the kinetic energy was found be higher than 0.008 $m^2/s^2$. The initial water temperature was around 21˚C in run 3. Higher temperatures resulted in the large temperature difference between cryogenic liquid and water, and subsequently the energy supplied was also large. It can also be noted that the fluctuations were large and random in run 3 when compared to other runs whose fluctuations were small and stable. These overshoots reached a magnitude of 0.018 $m^2/s^2$. Runs 2 and 4 were found to have similar initial turbulent kinetic energy value of 0.007 $m^2/s^2$ .Even though the initial water temperature in run 4 was similar to run 2, run 4 was found to be anomalous to the other runs having a kinetic energy greater than run 2. This might have been attributed to the ice formation in run 4 during the later stages of vaporization. The ice formation was found to promote the turbulent kinetic energy. Currently there is no well-established theory for explaining the effect of ice formation on turbulent kinetic energy. Thus, it was difficult to conclude the dependency of turbulent kinetic energy on ice formation. In all the runs, a dependence of turbulent kinetic energy on liquid height was not observed.

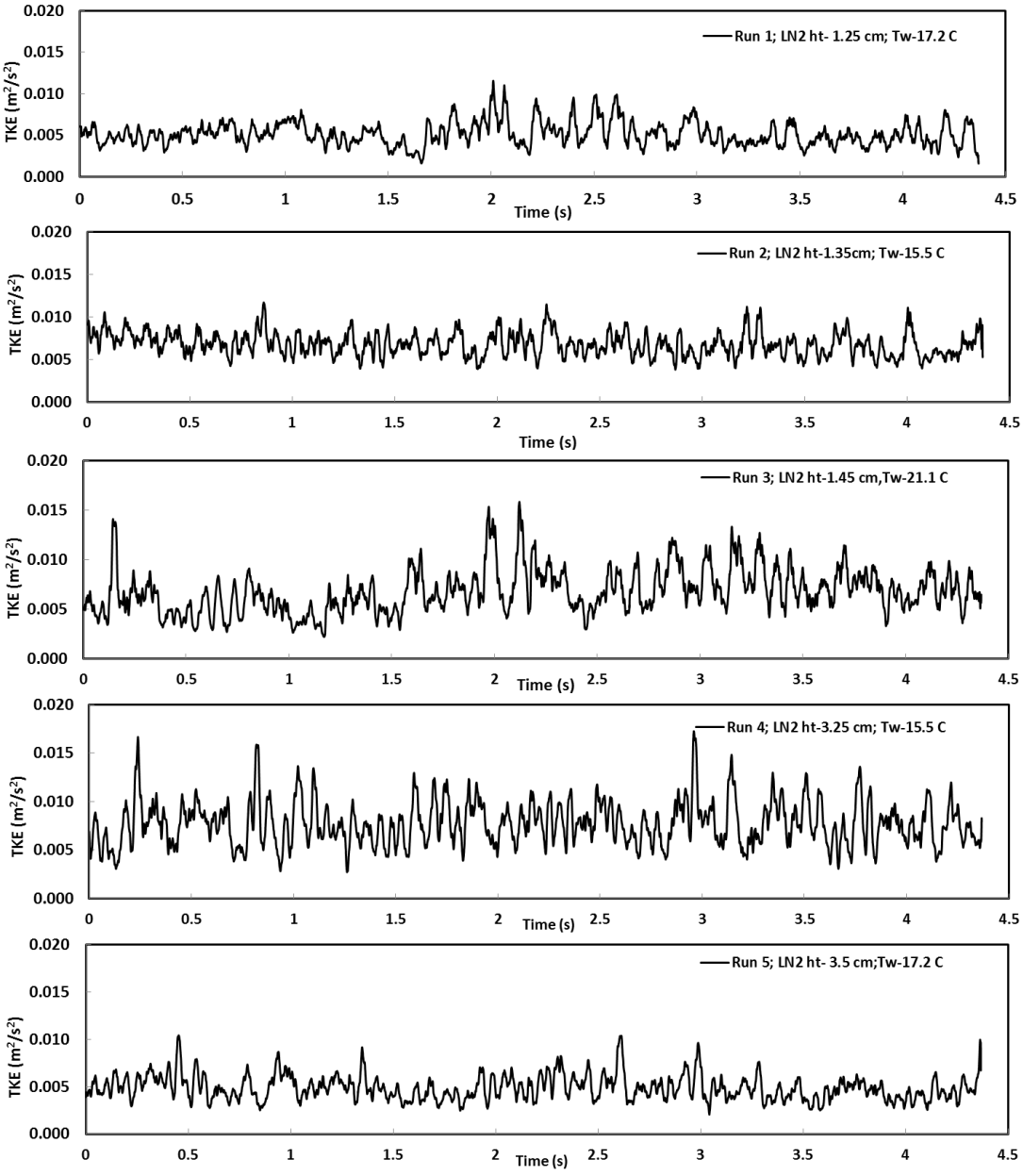


Figure 36. Turbulent Kinetic Energy (TKE) profiles

### 6.6.5. Eddy Dissipation Rate

The dissipation rate of kinetic energy determined the degree of thermal dissipation and break down of thermals that were formed during the vaporization

process. The frozen turbulence hypothesis was employed to determine the dissipation of kinetic energy (Batchelor and Goldstein, 1982). The hypothesis allowed spatial derivatives to be replaced by time derivatives. This was based on the assumption that turbulent eddies that were advected past the point of observation were fast enough to make the flow field constant during the time of passage. For isotropic turbulence the dissipation of kinetic energy '$\epsilon$'can be expressed as ensemble average of velocity as

$$\epsilon = 15\nu < \left(\frac{\partial v}{\partial t}\right)^2 > \quad (49)$$

where $\nu$ is the kinematic viscosity of liquid nitrogen in $m^2/s$, v is the velocity in vertical direction and t is time. Figure 37 depicts the variation of eddy dissipation rate profiles. The eddy dissipation was relatively constant in runs 1, 3, 4 and 5 and was found to vary from 0.001 to 0.002 $m^2/s^3$. The eddy dissipation rate was found to be weakly dependent on the salt content. Higher dissipation rates (> 0.002 $m^2/s^3$) were observed in run 2 when thermals were produced from deionized water. The deionized water tends to have a lower water density than water with salt. This in turn increases the density differences between liquid nitrogen and water. The density differences promote convection which is accompanied by collision of thermals convection currents with one another. The collision caused breakdown of currents and subsequent loss of energy. This phenomenon resulted in higher values of eddy dissipation rate for run 2.

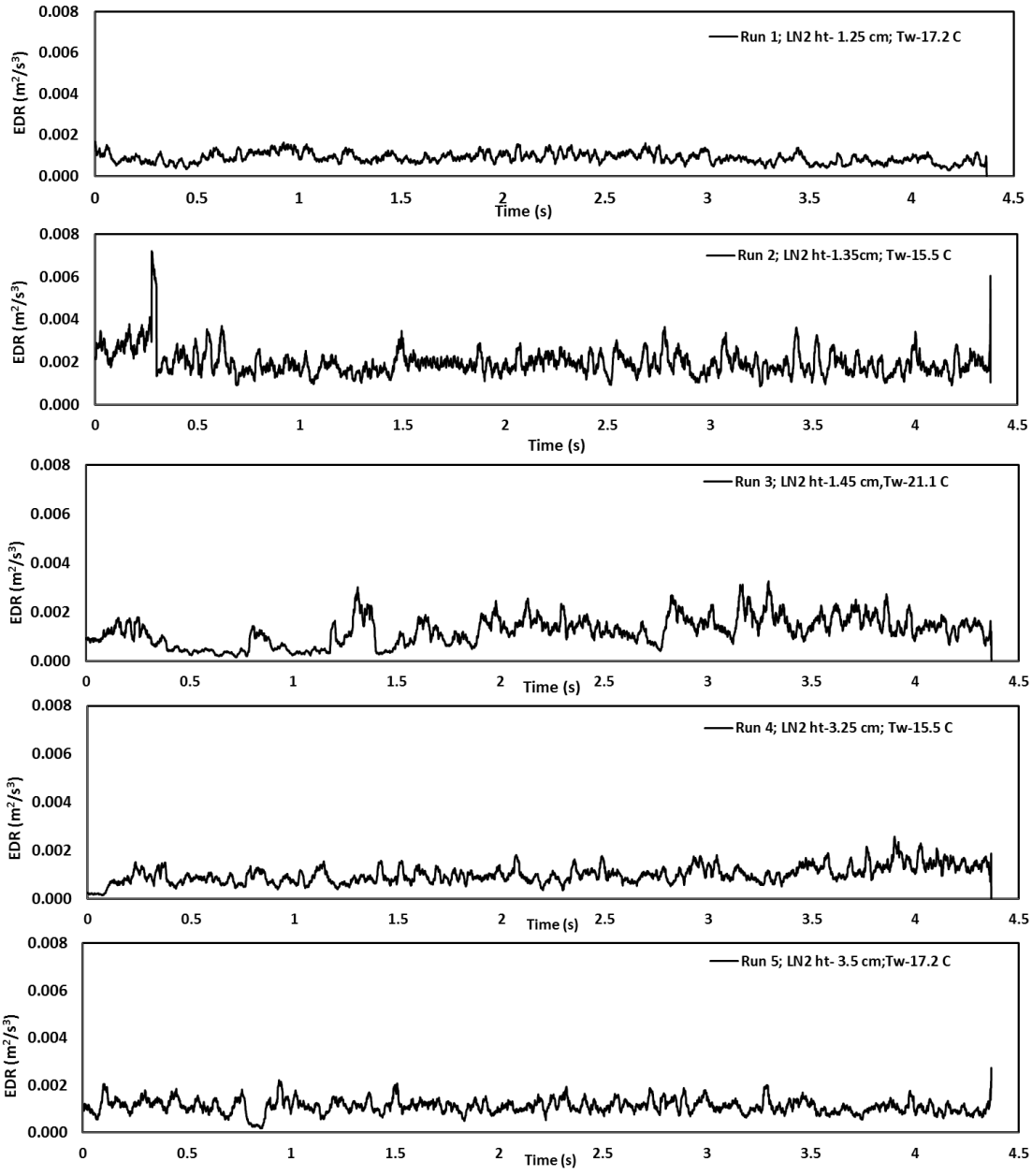


Figure 37. Eddy Dissipation Rate (EDR) profiles

### 6.6.6. Vaporization Mass flux of Cryogenic Liquid

#### 6.6.6.1. Effect of Cryogenic Liquid Height

From the results obtained in previous sections (6.5.3-6.5.5), it is clear that turbulence development and vaporization enhancement cannot be simply explained by change in convection currents in the cryogenic liquid. The vaporization process was dependent on initial water temperature and cryogenic liquid height. Detailed study on effect of initial water temperature was studied previously and is not dealt with here. The results of the study indicated a decreasing trend in vaporization mass flux with increase in initial water temperature. High initial water temperature (>40˚C) resulted in steeper slopes for vaporization flux. This slope gradient was found to decline with the initial water temperature (Gopalaswami, Olewski, Véchot, and Mannan, 2015). More detailed analysis of the cryogenic liquid height was required to understand the vaporization process. To facilitate the analysis, the vaporization mass fluxes were determined by multiplying the velocity magnitude obtained from image processing with vapor density. The effect of liquid nitrogen height on vaporization was studied by determining the height with respect to time. The height of the liquid nitrogen-air interface was determined for each image pair using intensity of the image. The image was first converted to black and white with a threshold that minimizes the intra-class variance of the black and white pixels. The threshold was determined for each image by the Otsu method (Otsu, 1979). From the black and white image, the height of the liquid nitrogen was detected by using a Matlab function that implements the Moore-Neighbor tracing algorithm modified by Jacob's stopping criteria (Gonzalez, Woods, and Eddings, 2006).

The time series of liquid nitrogen height for one run (run 2) is presented in Figure. 38(a). The height could be predicted only for runs 1, 2 and 3 with a low cryogenic liquid height (<2 cm). In runs where cryogenic liquid was high (>2cm), the cryogenic liquid- air interface was not visible in the camera's region of influence. From Figure. 38(a) one can observe that the height of liquid nitrogen declined gradually with time. As the height of liquid nitrogen decreased, the vaporization mass flux was found to decrease gradually. As the vaporization proceeded, the temperature declined gradually and as a result, the turbulent kinetic energy of thermals decreased along with the height. As the temperature declined, the vaporization mass flux also declined as the heat flux provided by water is dependent on the water temperature. This trend is observed in Figure.38 (b). In all runs, the expected trend of gradual reduction in vaporization occurred during the spill. However, the vaporization mass flux was found to be random and chaotic in run 3 owing to the high initial water temperature. This was due to the fact that the high initial water temperature in this run provided additional energy causing upward motion of thermals along the cryogenic liquid layer. As the thermals reached the liquid nitrogen-air interface, an outburst occurred, leading to vaporization of cryogenic liquid. This was observed as sudden shoot-ups in the vaporization mass flux. The magnitude of these outbursts increased with the increase in temperature.

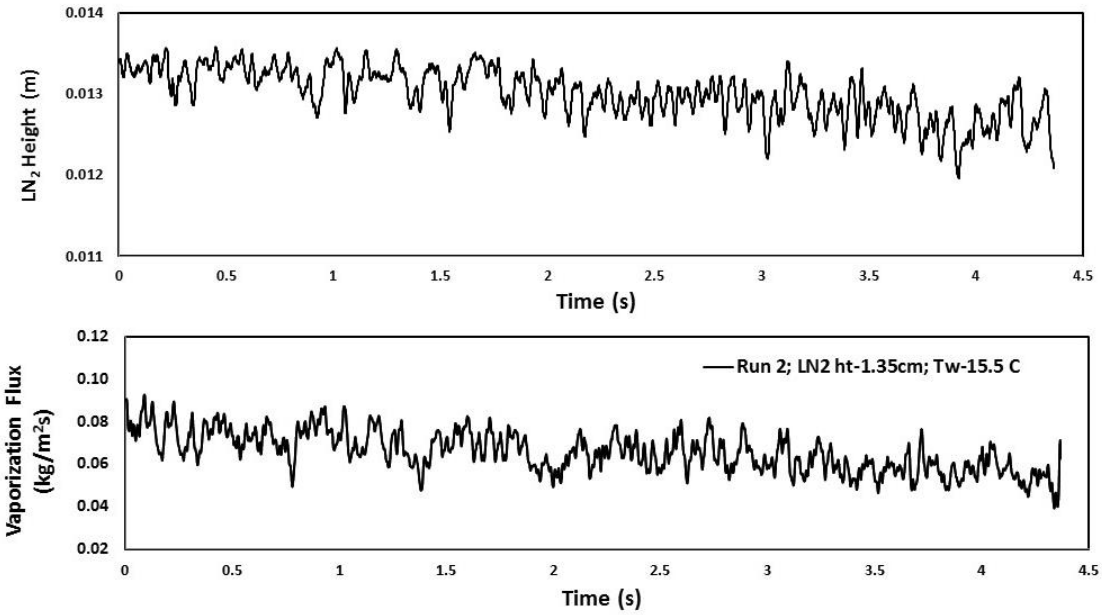


Figure 38. (a) Height of liquid nitrogen (b) vaporization mass flux of liquid nitrogen with respect to time (run 2)

The effect of initial height on vaporization flux was investigated and presented in Figure 39. The experimental results obtained in this study was compared with results from Morse and Kytömaa, (2011) and Drake, Jeje, and Reid, (1975). Drake *et al* performed multiple experiments on methane, ethane and liquid nitrogen by varying the initial water temperature and amount of cryogen spilled. They concluded that the vaporization rate of liquid nitrogen was proportional to the square root of liquid height. In the current study, the vaporization mass flux of liquid nitrogen was found to be directly proportional to the initial height of liquid nitrogen. As the height of cryogenic liquid increased, the collision of thermals with one another increased inside the cryogenic liquid. This resulted in increased mixing within the liquid leading to increasing vaporization. However, when the initial height of cryogenic liquid was low,

the thermals with high initial energy traversed directly to the cryogenic liquid-air interface. This resulted in less mixing within the cryogenic liquid.

The vaporization flux obtained in this experiment was found to be lower than the vaporization flux obtained by Morse and Kytömaa (2011) and Drake, Jeje, and Reid (1975) for the same liquid nitrogen height. The discrepancy was attributed to the methodology used to determine the vaporization flux. In the former paper (Morse and Kytömaa, 2011), the vaporization mass flux was determined from instantaneous velocity, where the instantaneous velocity due to change in height was determined by a balance of kinetic and potential energy. Contrary to this method, the vaporization mass flux in Drake *et al* was obtained by determining the slope of mass loss that occurred during the vaporization process. However, in the current experiment, the vaporization mass flux was obtained from the instantaneous velocity components determined from high speed images. All these three methods differ significantly from the fact that the primary variable used to determine the vaporization mass flux was different (height, mass and velocity). In addition to the method used to determine vaporization mass flux, the initial water temperature used in these three tests was different which caused variations in magnitude of vaporization mass flux. However, the overall increasing trend of vaporization flux with initial $LN_2$ height was found to be the same.

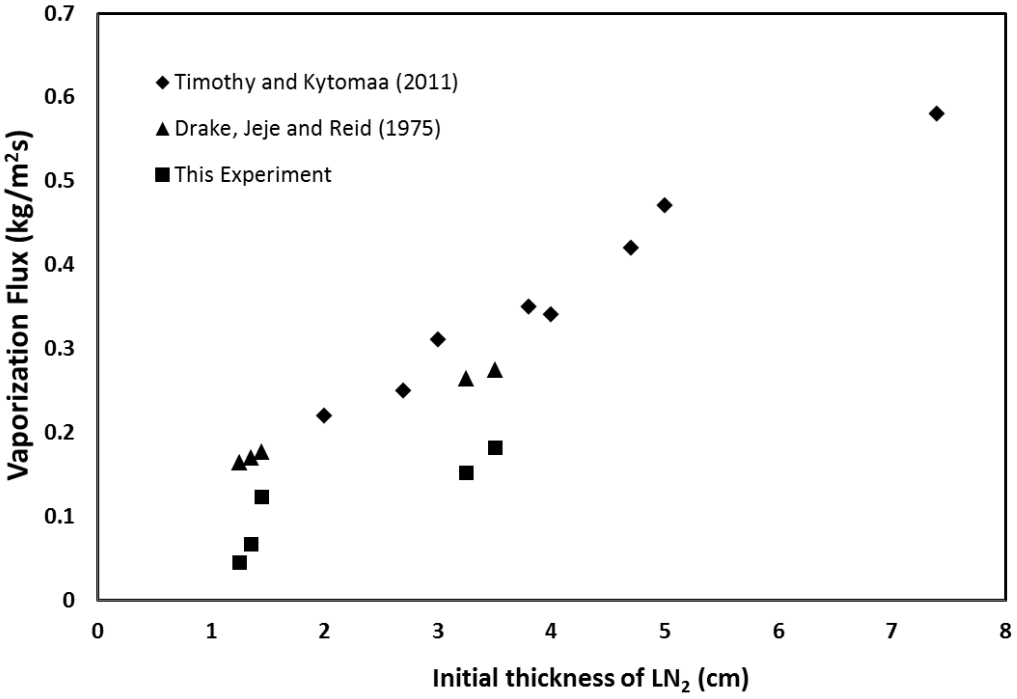


Figure 39. Variation of vaporization flux with initial height of $LN_2$

### 6.6.6.2. Effect of Turbulence Parameters

The main intent of this study is to examine the effect of turbulence parameters on vaporization flux. Figure 40 shows the variation of dimensional turbulent intensity ($\sqrt{(u'^2 + v'^2)}$ ) with vaporization mass flux of liquid nitrogen. The trend lines of data points are fitted by polynomial functions. The dimensional turbulent intensity was chosen here to compare with vaporization flux to characterize the turbulent component of velocity. As mentioned earlier in section 5.3, increase in cryogenic liquid was associated with an increase in vaporization mass flux. This trend is due to the influence of liquid nitrogen height on the instantaneous velocity of thermal convection currents. When the instantaneous velocity was low, the turbulent velocity, which is the difference

between instantaneous velocity and mean velocity ($u' = \bar{U} - u'$) was found to be high. Such high turbulent velocity was associated with high turbulent intensity. However, simultaneously when the turbulent velocity was low, the turbulent intensity, was also observed to be low. This resulted in low vaporization flux during time intervals of low turbulent intensity. Thus, the dimensional turbulent intensity was found to be directly dependent on vaporization mass flux.

The turbulent kinetic energy had a pronounced effect on the vaporization flux. The turbulent kinetic energy was found to have a direct influence on vaporization flux (Figure 41). Higher turbulent kinetic energy resulted in faster velocities of thermals. When the turbulent kinetic energy is high, the likelihood of thermals reaching the cryogenic liquid-air interface increased, which potentially resulted in increased vaporization. However, increase in eddy dissipation rates had minor influence on the vaporization mass flux of liquid nitrogen. This is observed in Figure 42. The dissipation of energy within the cryogenic liquid was less affected by the thermals developing in the water-cryogenic liquid interface. This trend might also be due to the frozen turbulence hypothesis that was applied in determining the eddy dissipation rate parameter. However, more experimental data would be required to analyze the trend of vaporization flux for higher eddy dissipation rates.

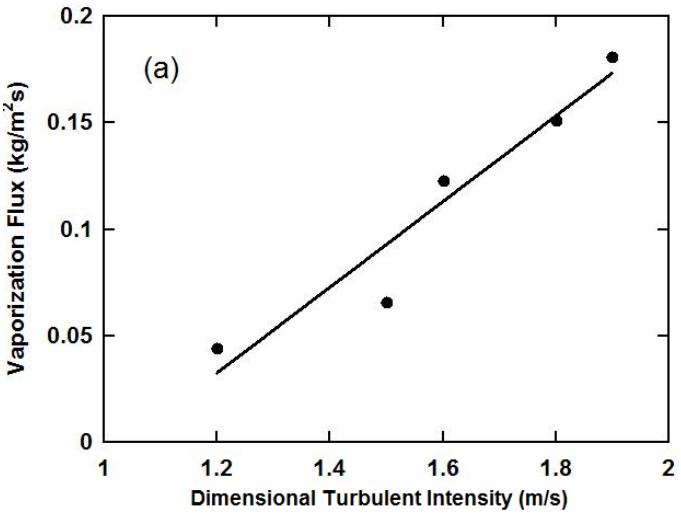


Figure 40. Variation of vaporization mass flux with Turbulent Intensity (TI)

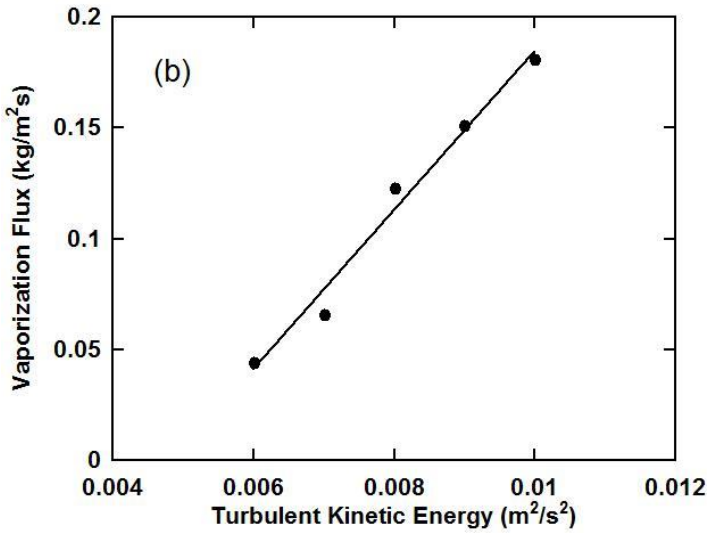


Figure 41.Variation of vaporization mass flux with Turbulent Kinetic Energy (TKE)

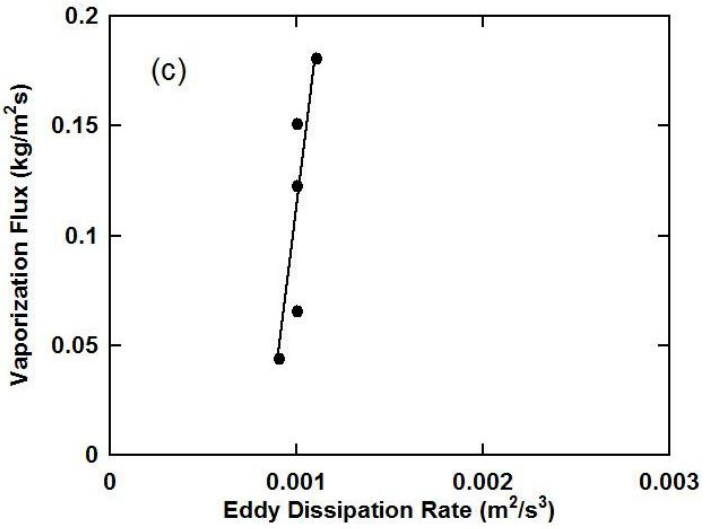


Figure 42. Variation of vaporization mass flux with Eddy Dissipation Rate (EDR)

## 6.7. Conclusion

In this study, turbulence produced due to the vaporization of a cryogenic liquid on water was quantified using a high speed flow visualization process. The determination of its magnitude posed a formidable challenge for understanding the dynamics of turbulence. The turbulence determination experiment showed the existence of transient thermal convection currents that arose from the water-cryogenic liquid interface. The experimental results demonstrated that the propagation of thermal convection currents in the vertical and horizontal direction induced significant turbulent mixing. These turbulent structures were found to act like catalyst in enhancing the vaporization between the cryogenic liquid and water. Both the instantaneous and ensemble-averaged turbulent velocity data highlighted some important features of the flow field inside the cryogenic liquid. The horizontal velocity data presented a

magnitude which was twice as less than the magnitude of vertical velocity. The turbulent intensity, turbulent kinetic energy and eddy dissipation rate were reported with respect to time. In unsteady flow, the turbulent intensity was found to be inversely dependent on height of cryogenic liquid. For runs with similar cryogenic liquid height, the turbulent intensity was found to be greater for runs with higher initial water temperature. The reduction in height of the cryogenic liquid is associated with reduction of vaporization flux. The increase in vaporization flux was found to be associated with increase in turbulent intensity. Variations in turbulence kinetic energy parameter were found to be strongly associated with vaporization mass flux of liquid nitrogen. Increase in initial water temperature resulted in significant enhancement of turbulent kinetic energy. The eddy dissipation rate was relatively constant and had a negligible effect on vaporization mass flux. Application of the experimental results based on $LN_2$ for large-scale spills of LNG will depend on the factors that influence the turbulence parameters. From the current study, it can be concluded that the initial water temperature and height of cryogenic liquid have a strong influence on the turbulence parameters. Similarly, the turbulence parameters and initial height of cryogenic liquid had a direct influence on the vaporization flux. A comparison with literature resulted in similar trends for liquid methane and ethane. Although, the turbulence values are likely to be similar to LNG applications, detailed future work will involve the application of turbulence values in CFD models to computationally analyze the effect of turbulence parameters on vaporization mass flux for LNG spills of varying sizes.

# CHAPTER VII

# CFD METHODOLOGY

## 7.1. Introduction

In this chapter, a novel CFD-based methodology is developed to simulate the pool spreading and vaporization of LNG on water. The CFD method involves a hybrid multiphase flow to capture the flow of LNG on water. A user defined routine is implemented for capturing the vaporization of LNG into air and heat transfer from water to LNG. The CFD methodology is validated against a specific offshore scenario. The scenario involves rupture of loading line leading to a leak of LNG into the space enclosed between two LNG ships. The experimental study was conducted by releasing LNG in a narrow trench filled with water and subsequent measurement of pool spreading parameters and vaporization rate. The spreading of LNG on water and subsequent vaporization involves a multiphase multicomponent flow with heat and mass transfer where LNG flows on water and simultaneously undergoes a phase change to vapor state due to the large temperature difference between water and LNG. The CFD methodology is then validated with the experiment and the efficiency of the model is evaluated in relation to the pool spreading and vaporization phenomena.

## 7.2. Experimental Setup and Procedure

The experiment was performed in an L-shaped trench present in Brayton Fire Training Field (BFTF), College Station. Each leg (leg 1 and leg 2) of the trench is 8.2 m long, 1.22 m wide and 1.05 m deep (see Figure 43). Prior to the experiment, the trench was filled with water up to a height of 0.8m. A weather station was installed near the

trench to obtain the local weather conditions such as wind speed, wind direction, atmospheric pressure and temperature, and relative humidity. The trench was equipped with N-type thermocouples in a linear arrangement to measure the water temperature and LNG temperature respectively during the spill. In addition to these, a wooden boards with an array of thermocouples is installed in between two legs of the trench to measure the height of LNG during the experiment. Table 13 provides the dimensions of thermocouples employed in the experimental setup. The origin is present at the bottom of the leg 1 of trench close to discharge area. The positive x-axis and positive y-axis is representative of the global southwest and southeast directions. The positive z-axis denotes the elevation which is zero at the bottom of the trench.

The experimental setup for pool spreading and vaporization is provided in Figure 43. The experiment was coordinated with three video cameras and one infra-red camera. Camera 1 and camera 2 were placed to track the pool spreading of LNG in leg1 and leg2 respectively and camera 3 provided an aerial view of the experiment. The infrared camera was placed laterally to leg 2 of the trench, to track the LNG liquid pool over water. An ultrasonic level transmitter (Echopod DL-24) was placed in leg 2 of the trench to track the dynamic height of LNG during vaporization process. The advantage of ultrasonic level transmitter is the ability to see through LNG vapors produced during the two-phase flow of LNG and measure the level of liquid effectively. The thermocouples and level sensors' output was recorded every second (1Hz) by a Data Acquisition system (DAQ), and the recorded data was sent to a computer for processing.

Table 13. Thermocouple dimensions

| Leg 1 | | | | Leg 2 | | | | Board 1 | |
|---|---|---|---|---|---|---|---|---|---|
| **TC ID** | **L (m)** | **W (m)** | **H (m)** | **TC ID** | **L (m)** | **W (m)** | **H (m)** | **TC ID** | **H (m)** |
| **TC-1** | 0.8 | 0.90 | 0.90 | **TC-14** | 1.63 | 0.91 | 0.88 | **TB-01** | 0.01 |
| **TC-2** | 1.1 | 0.90 | 0.76 | **TC-15** | 1.93 | 0.91 | 0.85 | **TB-02** | 0.02 |
| **TC-3** | 1.5 | 0.90 | 0.90 | **TC-16** | 2.24 | 0.91 | 0.94 | **TB-03** | 0.03 |
| **TC-4** | 2.0 | 0.90 | 0.86 | **TC-17** | 2.54 | 0.91 | 0.86 | **TB-04** | 0.04 |
| **TC-5** | 2.7 | 0.90 | 0.90 | **TC-18** | 2.87 | 0.91 | 0.93 | **TB-05** | 0.05 |
| **TC-6** | 3.3 | 0.90 | 0.76 | **TC-19** | 3.16 | 0.91 | 0.86 | **TB-06** | 0.08 |
| **TC-7** | 3.6 | 0.90 | 0.91 | **TC-20** | 3.45 | 0.91 | 0.86 | **TB-07** | 0.10 |
| **TC-8** | 4.0 | 0.90 | 0.79 | **TC-21** | 3.76 | 0.91 | 0.86 | **TB-08** | 0.11 |
| **TC-9** | 4.3 | 0.90 | 0.89 | **TC-22** | 4.37 | 0.91 | 0.95 | **TB-09** | 0.13 |
| **TC-10** | 4.6 | 0.90 | 0.91 | **TC-23** | 4.67 | 0.91 | 0.86 | **TB-10** | 0.14 |
| **TC-11** | 5.2 | 0.90 | 0.93 | **TC-24** | 4.98 | 0.91 | 0.95 | **TB-11** | 0.15 |
| **TC-12** | 5.8 | 0.90 | 0.88 | **TC-25** | 5.28 | 0.91 | 0.86 | **TB-12** | 0.18 |
| **TC-13** | 7.0 | 0.90 | 0.98 | **TC-26** | 5.59 | 0.91 | 0.95 | | |
| | | | | **TC-27** | 5.88 | 0.91 | 0.85 | | |
| | | | | **TC-28** | 6.20 | 0.91 | 0.95 | | |
| | | | | **TC-29** | 6.50 | 0.91 | 0.88 | | |
| | | | | **TC-30** | 6.81 | 0.91 | 0.95 | | |
| | | | | **TC-31** | 7.11 | 0.91 | 0.86 | | |
| | | | | **TC-32** | 7.42 | 0.91 | 0.98 | | |

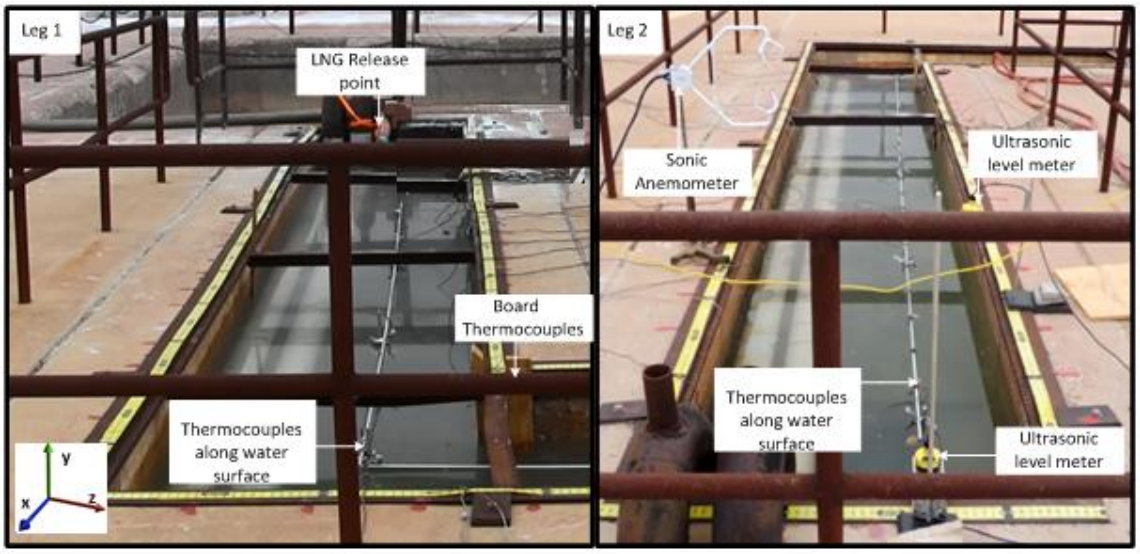


Figure 43. Experimental setup

LNG was continuously discharged from a tanker of 11000 gallon capacity through a cryogenic hose (internal diameter-0.076m). As and when LNG was released continuously, it traversed through the trench and liquid level starts to increase. A total of 20 $m^3$ of LNG was released at a rate of 9.5±0.08 kg/s for duration of about 20 minutes. A summary of release conditions and atmospheric conditions present during the experiment is provided in Table 14.

Table 14. Summary of release conditions and atmospheric conditions of experiment

| **Release Conditions** | | |
|---|---|---|
| **LNG flow rate** | 9.5±0.08 kg/s | |
| **Spill duration** | 1200 s | |
| **Water temperature** | 20 ˚C | |
| **Spill area** | 17.8 $m^2$ | |
| **LNG Composition** | 100% Methane | |
| **Diameter of discharge pipe** | 0.076 m | |
| **Atmospheric Conditions** | | |
| **Wind Velocity** | 6.2±1.3 | m/s |
| **Wind Direction** | SE | |
| **Atmospheric Temperature** | 25.6±0.03 | ˚C |
| **Air Pressure** | 30.15 | in |
| **Relative Humidity,** | 52.6 | % |
| **Dew Point temperature** | 15.1 | ˚C |
| **Stability Class** | C | |
| **Solar radiation** | 4.34 | $kW/m^2$/day |
| **Sensible heat flux** | 18.06 | $kW/m^2$ |
| **Ground Roughness length** | 0.03 | m |
| **Water Roughness** | 0.0004 | m |

### 7.3. Mathematical Model

The Ansys CFX software was chosen to develop the computational model. The CFD methodology is named as ‘LSPREAD’ for LNG pool spreading and vaporization

and will be referred to the same in the rest of the paper for convenience. Three fluids, namely LNG, water, and air were defined in the computational domain. LNG was modeled as pure methane with density 450 kg/$m^3$. For suitability of performing phase change modeling, it is assumed that vapor liquid equilibrium exists in phase equilibrium.

To model the LNG flow on water the homogeneous Eulerian multiphase model was adopted. The release of LNG on water involves a fragmented jet where small droplets vaporize immediately to vapor and large droplets collect to form a pool. To address this phenomenon, LNG is modeled as dispersed phase droplets which break-up and evolve in the continuous phases (air and water). Contrary to this method, there is another approach called Volume of Fluid (VOF) approach where LNG is modeled as continuous phase. In VOF methodology, the droplets which are smaller than the grid size cannot be represented in a mesh and discretized which can lead to compromise in the physics. The mean diameter chosen is based on the initial volume of LNG present at each timestep. The droplet size was assumed to be between 0.01-0.02m. The droplets size shown in this study corresponds to a value of 0.017 m. Currently LNG droplet sizes are not available and the values of bubble diameter were adopted. The diameter corresponds to the size range of bubbles (0.01-0.018m) observed in pure methane and light LNG during vaporization process (Drake *et al.*, 1975a), (Drake *et al.*, 1975b).

In LSPREAD all three components are solved using one single flow field and the fluids interact via interphase transfer terms. The particle model was chosen to capture the interphase phenomena between LNG and air and LNG and water, whereas the sharp interface between two continuous phases- air and water was modeled using the free

surface model. A volume fraction function is introduced to characterize the mixing of LNG droplets with continuous phases like water and air. The transport properties of the mixture are deduced from volume fraction of each fluid.

### 7.3.1. Computational Domain

Currently, there exists a whole range of models for LNG pool spreading and vaporization, but CFD offers an additional advantage of handling complex geometries, which can either be imported or built with in the software. Geometry is important to capture the pool spreading scenario between obstacles and to capture the flow fields that influence the simulated variables of interest. The computational domain of interest was built in design modeler of CFX and it consists of the L-shaped trench and a rectangular region to simulate the atmosphere above the trench. This is represented in Figure 44(a). The atmosphere over the trench extended 15.24 m (50ft) in the lateral directions and 1.54 m (5ft) above the trench. Each leg of the trench was modeled based on the dimensions of actual setup. Negative Z axis is the downwind direction, negative X axis is the direction of LNG flow in leg 1 and Y axis reflects the vertical direction.

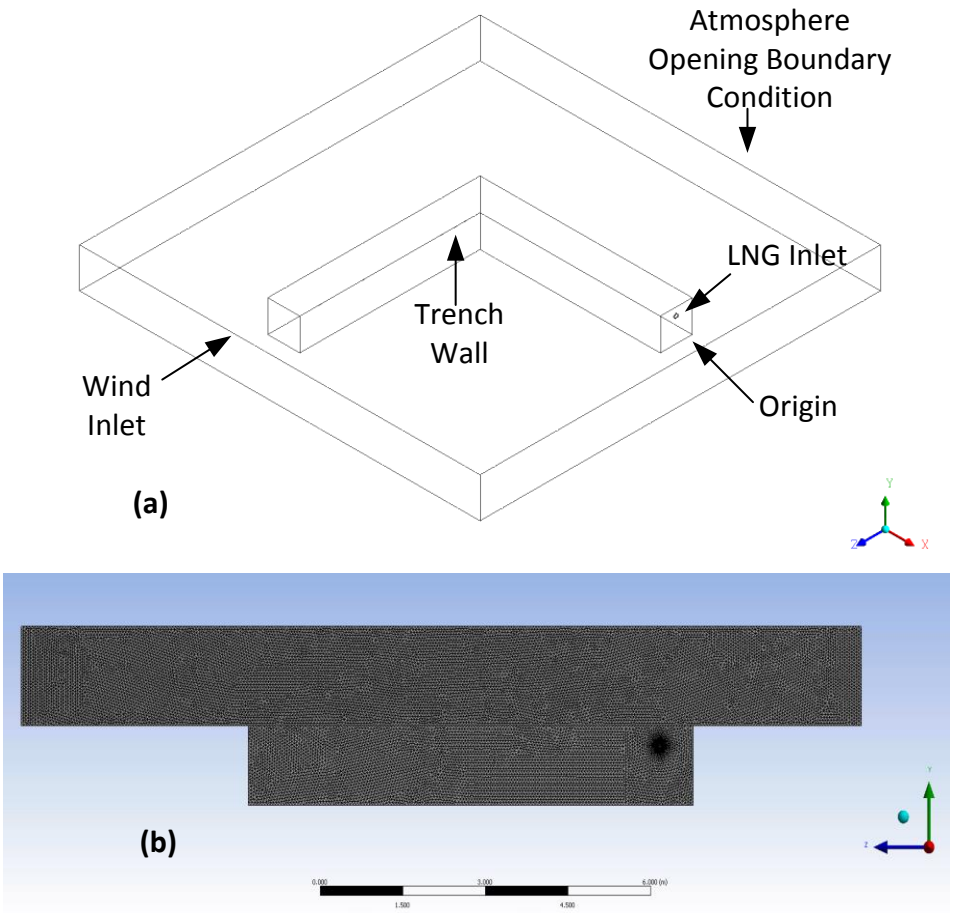


Figure 44 (a). Computational domain (b). Side view of the mesh

### 7.3.2. Grid Sensitivity Analysis

Discretization is achieved by Finite Volume Method (FVM) implemented in CFX. In this method, the computational domain is divided into small control volumes and governing equations are solved at each control volume. A block structured meshing approach was used to create the meshes with tetrahedral cells in Ansys meshing module and is shown in Figure 44(b). This is computationally efficient in multiphase simulations where time taken for computation is extremely large (order of days). The meshes were

refined to investigate its effect on the results. A grid sensitivity analysis was performing by simulating three grids of sizes $0.96x10^6$ elements, $3.2x10^6$ elements and $7.7\ x10^6$ elements. The grids correspond to different element sizes as shown in Table 15. All the simulation parameters were kept identical in all the runs to ensure the grid independency of the results. Figure 45 shows the water temperature value with respect to the distance from LNG discharge. The water temperature is an important variable from which the pool spreading parameters and vaporization mass fluxes are determined in this study. This is greatly influenced by the discharge location and it reduces more near the discharge when compared to regions away from the discharge location. As can be seen in Figure 45, the results of grid 2 and grid 3 are identical whereas grid 1 depicts a magnitude and a trend that is different from grid 2 and grid 3. A mesh-independent solution was achieved with a grid consisting of $3.2x10^6$ elements. This was applied for rest of the simulations as any further increase in grid size does not alter the simulations results. The elements size in this grid was restricted to 0.05m in the trench to allow for the optimum resolution of interface between water and LNG. The element size was restricted to 0.1 m in the atmospheric region.

Table 15. Grid sensitivity analysis

| Parameters | Grid 1 | Grid 2 | Grid 3 |
|---|---|---|---|
| **Smallest element size** | 0.075 | 0.05 | 0.05 |
| **Largest element size** | 0.15 | 0.1 | 0.075 |
| **(Largest -smallest) element** | 0.075 | 0.05 | 0.025 |
| **Total Nodes** | 176154 | 573256 | 1346905 |
| **Total Elements** | 969218 | 3245728 | 7706835 |
| **Total simulation time** | 600 | 600 | 600 |
| **Water temperature at 600s** | 290.8 | 291.4 | 291.4 |

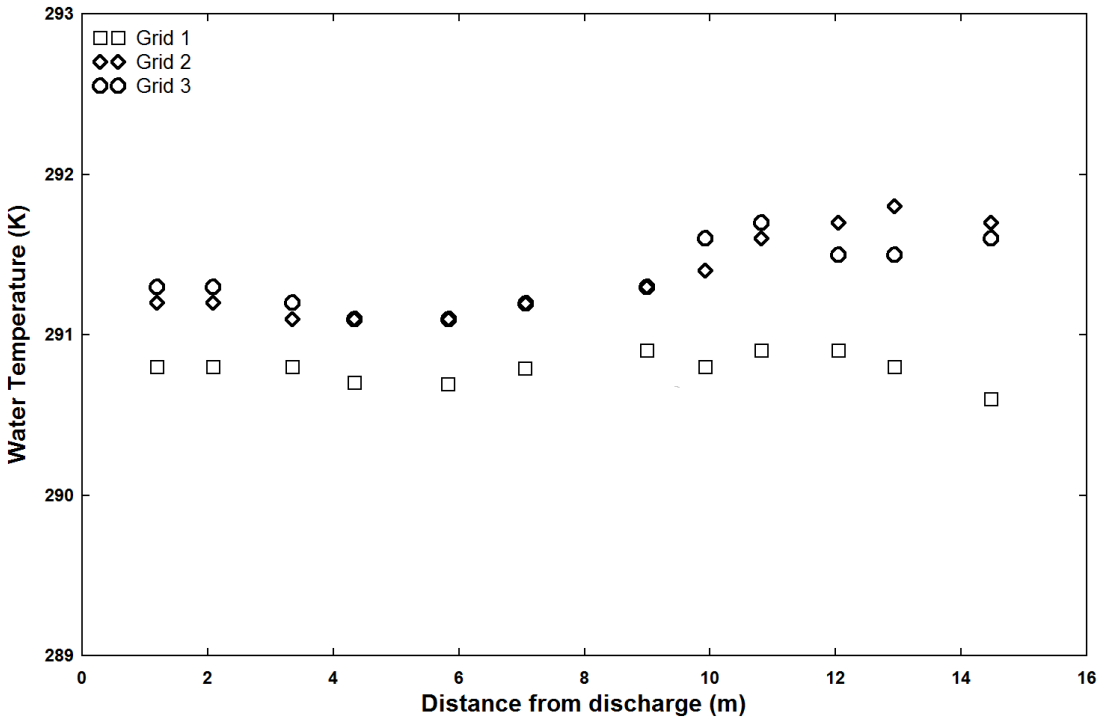


Figure 45. Grid sensitivity analysis showing water temperature values with respect to distance from discharge.

### 7.3.3. Boundary Conditions

The walls of the trench were provided with a no slip boundary condition. The walls of trench were classified as adiabatic providing no heat transfer to the water. Although, in experiment the concrete wall would have provided heat, this heat was neglected as the height of concrete interacting with LNG was quite low. The LNG pipe of diameter 0.076 m was provided as inlet. The top surface of the trench was provided with an opening boundary condition to allow the transfer of LNG to air and penetration of air into LNG. A wind velocity was provided at wind inlet to simulate the effect of wind on the pool. The initial setup of the geometry included the initial height of water in

the trench with air above it. The volume fractions of water and air were provided based on the height of water. The reference parameters are defined by the acceleration due to gravity (9.81 m/s$^2$), reference pressure (1 atm), and reference density (air density- 1.225 kg/m$^3$).

### 7.3.4. Governing Equations

The governing equations consists of a set of partial differential equations expressing the conservation of mass, momentum, enthalpy and two turbulence variables in a three dimensional flow. In doing this, it is assumed that the Coriolis forces are negligible and the Boussinesq approximation is valid.

The mass transport equation is given by

$$\frac{\partial \rho}{\partial t} + \nabla.(\rho U) = \Gamma_{\alpha|\beta} \quad (50)$$

where $\frac{\partial \rho}{\partial t}$ is called the transient term, $\nabla.(\rho U)$ is the convection term and $\Gamma_{\alpha|\beta}$ is the source-term. $\rho$, r and U are the density, phase fraction and velocity. $r_{LNG}, r_{air}, r_{water}$ refer to the phasic fraction of LNG, air and water respectively. $\Gamma_{LNG|air}$ refers to the mass transfer occurring from LNG to air phase. $\Gamma_{LNG|Water}$ refers to the mass transfer between LNG and water and $\Gamma_{Air|Water}$ refers to the mass transfer between air and water. $\Gamma_{LNG|Water}$ =$\Gamma_{Air|Water}$ $= 0$ as there is no mass been transferred from LNG to water.

Expanding it in scalar terms we get

$$\frac{\partial \rho}{\partial t} + \frac{\partial(\rho u)}{\partial x} + \frac{\partial(\rho v)}{\partial y} + \frac{\partial(\rho w)}{\partial z} = \Gamma_{\alpha\beta} \quad (51)$$

Here density is based on volume fraction of each component given by

$$\rho = r_{LNG}\rho_{LNG} + r_{air}\rho_{air} + r_{water}\rho_{water} \quad (52)$$

This involves transfer of one fluid to another.

$$\Gamma_{\alpha|\beta} = \Gamma_{LNG|air} + \Gamma_{LNG|water} + \Gamma_{air|water} \quad (53)$$

The momentum transport equation is given by

$$\frac{\partial(\rho U)}{\partial t} + \nabla(\rho UU) = -\nabla p + \nabla.\tau + \rho g \quad (54)$$

$$\tau = r_{LNG}\tau_{LNG} + r_{air}\tau_{air} + r_{water}\tau_{water} \quad (55)$$

$\frac{\partial(\rho U)}{\partial t}$ is the transient term that accounts for the accumulation of LNG, air and water in the concerned control volume , $\nabla(\rho UU)$ is the convection term that addresses the transport of components due to the existence of the velocity field $(-\nabla p + \nabla.\tau + \rho g)$ is called the diffusion term that accounts for the transport of components due to its gradients.

Writing this in scalar form we obtain

u momentum:

$$\frac{\partial(\rho u)}{\partial t} + u\frac{\partial(\rho u)}{\partial x} + v\frac{\partial(\rho v)}{\partial y} + w\frac{\partial(\rho w)}{\partial z} = -\left(\frac{\partial p}{\partial x}\right) + \rho g + \frac{\partial \tau_{xx}}{\partial x} + \frac{\partial \tau_{yx}}{\partial y} + \frac{\partial \tau_{zx}}{\partial z} \quad (56)$$

v momentum:

$$\frac{\partial(\rho v)}{\partial t} + u\frac{\partial(\rho v)}{\partial x} + v\frac{\partial(\rho v)}{\partial y} + w\frac{\partial(\rho v)}{\partial z} = -\left(\frac{\partial p}{\partial y}\right) + \rho g + \frac{\partial \tau_{xy}}{\partial x} + \frac{\partial \tau_{yy}}{\partial y} + \frac{\partial \tau_{zy}}{\partial z} \quad (57)$$

w momentum:

$$\frac{\partial(\rho v)}{\partial t} + w\frac{\partial(\rho w)}{\partial x} + v\frac{\partial(\rho w)}{\partial y} + w\frac{\partial(\rho w)}{\partial z} = -\left(\frac{\partial p}{\partial z}\right) + \rho g + \frac{\partial \tau_{xz}}{\partial x} + \frac{\partial \tau_{yz}}{\partial y} + \frac{\partial \tau_{zz}}{\partial z} \quad (58)$$

The energy transport equation is given by

$$\frac{\partial}{\partial t}(e_{LNG}) + \nabla.(r_{LNG}\rho_{LNG}\ Ue_{LNG}) = \nabla.(r_{LNG}\lambda_{LNG}T_{LNG}) + r_{LNG}\tau_{LNG}:\nabla U_{LNG} + S_{E_{LNG}} + Q_{LNG} + \Gamma_{LNG|air} \quad (59)$$

The terms $h_{LNG}, T_{LNG}, \lambda_{LNG}, e_{LNG}$ refer to the static enthalpy, temperature, thermal conductivity and internal energy of LNG. $\frac{\partial}{\partial t}(e_{LNG})$ refers to the change in internal energy, $\nabla.(r_{LNG}\lambda_{LNG}T_{LNG}) + Q_{LNG}$ refers to the change in enthalpy along x, y, z directions, $r_{LNG}\tau_{LNG}:\nabla U_{LNG}$ refers to the change in kinetic energy along x, y, z directions, $S_{E_{LNG}}$ refers to the external heat sources to LNG from water and air and $\Gamma_{LNG|air}$ refers to the phase change from LNG to air . The rest of the interphase changes are zero.

Expanding this in scalar term we obtain,

$$\frac{\partial}{\partial t}(\rho e) + w\frac{\partial(\rho e)}{\partial x} + v\frac{\partial(\rho e)}{\partial y} + w\frac{\partial(\rho e)}{\partial z} = -\left(w\frac{\partial(\rho)}{\partial x} + v\frac{\partial(\rho)}{\partial y} + w\frac{\partial(\rho)}{\partial z}\right) + [\frac{\partial(u\tau_{xx})}{\partial x} + \frac{\partial(u\tau_{yx})}{\partial y} + \frac{\partial(u\tau_{zx})}{\partial z} + \frac{\partial(v\tau_{xy})}{\partial x} + \frac{\partial(v\tau_{yy})}{\partial y} + \frac{\partial(v\tau_{zy})}{\partial z} + \frac{\partial(w\tau_{xz})}{\partial x} + \frac{\partial(w\tau_{yz})}{\partial y} + \frac{\partial(u\tau_{zz})}{\partial z} - \left(\frac{\partial(q_x)}{\partial x} + \frac{\partial q_y}{\partial y} + \frac{\partial q_w}{\partial z}\right) + S_{E_{LNG}} + \Gamma_{\alpha\beta} \quad (60)$$

Heat is been supplied from external sources like air ($q_{air}$) and water ($q_{water}$). This external heat source $S_{E_{LNG}}$ is given by

$$S_{E_{LNG}} = q_{air} + q_{water} \quad (61)$$

#### 7.3.4.1. Vaporization Model

The heat transfer from water to LNG is model is implemented using user defined functions in Ansys CFX through CFX Expression Language (CEL). Since heat is being

transferred from water to LNG, the water temperature declines with time whereas the LNG stays in its boiling point when it is boiling on water. The heat transfer coefficient is modeled based on the boiling regime; hence a time varying heat input is specified. From the previous experiments, it was observed that LNG stays in film boiling when released on water (Gopalaswami *et al.*, 2014) . Due to this reason, the Berenson model for film boiling was adapted for determining heat transfer coefficient (Berenson, 1961). The sub-model for vaporization was previously validated with small-scale experiments involving continuous releases of cryogenic liquid (Gopalaswami, Olewski, *et al.*, 2015).

The heat flux q is a combination of temperature difference and heat transfer coefficient provided by the Berenson's correlation expressed as

$$q_{water} = (T_{water} - T_{LNG}) * 0.425 \left[ \frac{k_V^3 \lambda \rho_V (\rho_L - \rho_V)}{\mu_V \Delta T \left( \frac{g(\rho_L - \rho_V)}{\sigma} \right)^{\frac{1}{2}}} \right]^{\left(\frac{1}{4}\right)} \quad (62)$$

The mass vaporization flux of LNG to air phase ($\Gamma_{LNG|air}$ ) is obtained from energy balance as

$$q_{air} = h_a . (T_{air} - T_{LNG}) \quad (63)$$

$$\Gamma_{LNG|air} = \phi \frac{q_{water} + q_{air}}{H_v} \quad (64)$$

The user defined function for mass transfer is implemented in CFX by enabling the 'specified mass transfer' for interphase fluid transfer. As LNG spreads, heat is provided by water and the amount of heat can be quantified by determining the heat transfer coefficient and temperature difference.

#### 7.3.4.2. Interphase Transport

The Particle model is selected for interfacial transfer between two LNG and air and LNG and water. The surface area per unit volume is determined based on the assumption that LNG is present as spherical particle of mean diameter. The interfacial area density is given by

$$A_{LNG|Air} = 6\frac{r_{LNG}}{d_{LNG}} \tag{65}$$

$$A_{Water|LNG} = 6\frac{r_{LNG}}{d_{LNG}} \tag{66}$$

#### 7.3.4.3. Turbulence Model

A homogeneous turbulence model is implemented which utilizes the value obtained from flow visualization studies. The turbulence was modeled using the standard k-ε turbulence model (Launder and Spalding, 1974). This model has been applied for numerical simulations of various LNG vapor dispersion experiment with satisfactory results (Luketa-Hanlin, Koopman, and Ermak, 2007) . The model developed by Launder and Spalding (1974) involves the solution of turbulent kinetic energy equation expressed as

$$\frac{\partial \rho k}{\partial t} + \nabla.(\rho u k) = \nabla.\left(\left[\mu_{lam} + \frac{\rho v_t}{\sigma_k}\right] \nabla k\right) + \rho v_t G - \rho\varepsilon \tag{67}$$

And the dissipation rate ($\varepsilon$) equation is as follows

$$\frac{\partial \rho \varepsilon}{\partial t} + \nabla.(\rho u \varepsilon) = \nabla.\left(\left[\mu_{lam} + \frac{\rho v_t}{\sigma_\varepsilon}\right] \nabla \varepsilon\right) + C_1 \rho v_t G \frac{\varepsilon}{k} - C_2 \rho \frac{\varepsilon^2}{k} \tag{68}$$

where the rate of generation of the turbulent kinetic energy, G, is given by

$$G = 2\left(\left[\frac{\partial u}{\partial x}\right]^2 + \left[\frac{\partial v}{\partial y}\right]^2 + \left[\frac{\partial w}{\partial z}\right]^2\right) + \left(\frac{\partial u}{\partial x} + \frac{\partial v}{\partial x}\right)^2 + \left(\frac{\partial u}{\partial y} + \frac{\partial v}{\partial y}\right)^2 + \left(\frac{\partial w}{\partial y} + \frac{\partial v}{\partial z}\right)^2 \tag{69}$$

where $\sigma_k$ and $\sigma_\epsilon$ are Prandtl numbers for k and ε respectively and $C_1$, $C_2$ and $C_\mu$ are model constants, $\mu_{lam}$signifies the laminar viscosity, $\mu_t$ and $\nu_t$ refers to the turbulent viscosity and kinematic viscosity.

The turbulence viscosity is related to $k$ and $\varepsilon$ by

$$\mu_t = \rho C_\mu \frac{k^2}{\varepsilon} \tag{70}$$

The effects of turbulence is incorporated as viscosity $\mu$ in the momentum equation which is the sum of laminar and turbulent viscosity

$$\mu = \mu_{lam} + \mu_t \tag{71}$$

The values of the empiric constants employed are given as

$$C_\mu = 0.09, \sigma_k = 1.0, \sigma_\varepsilon = 1.3, C_1 = 1.44, C_2 = 1.92 \tag{72}$$

The values of turbulence kinetic energy and eddy dissipation rate were obtained from a previous experimental study involving quantification of turbulence parameters using high speed visualization for cryogenic liquid spilled on water (Gopalaswami, Laboureur, Mentzer, and Mannan, 2015). The results provided average values of turbulent kinetic energy (0.005 $m^2/s^2$) and eddy dissipation rate (0.004 $m^2/s^3$).

Once the simulation is set, the governing equations are solved around the domain and each small volume defined by the mesh.

### 7.3.5. Solution Strategy

The equations were solved in RAAD supercomputer in Texas A&M Qatar. The criterion of convergence of Navier-Stokes equation was set to a value of $1E^{-4}$.The advection term is discretized using a second-order scheme weighted between central and upwind differencing, whereas the diffusion time was approximated according to the

second-order central differencing scheme. The time derivative term was approximated using a second-order backwards Euler time discretization scheme. A coupled solver is adopted for the momentum and pressure equations which are then solved iteratively with the turbulent scalar equations in an implicit manner for each time step. Pressure correction is achieved through a segregated solver which solves the momentum equations iteratively using an initial guessed pressure. The widely used SIMPLE algorithm is applied for the pressure correction scheme.

This timestep limits of interface capturing methods are limited by the Courant number (Moura and Kubrusly, 2012) expressed as

$$Cr = \frac{\Delta t}{\Delta x/u} \tag{73}$$

The timestep, $\Delta t$ is proportional to the mesh spacing, $\Delta x$ and inversely proportional to the flow velocity. This means that a spatial decomposition will result in a decrease of the time step that is to be used. The maximum courant number was restricted to 2. The time-stepping was performed using adaptive time stepping techniques that provides automatic control of time-step to achieve convergence in transient run. The minimum time-step was set to 0.001s and the maximum time-step was set to 1s with time step updating frequency of every 10 time steps. Figure 46 shows the schematic of CFD model with salient input and output parameters.

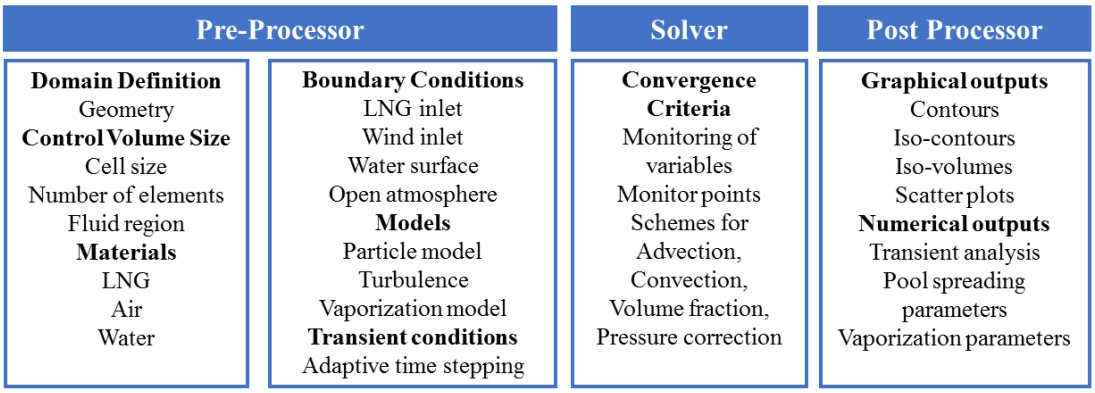


Figure 46. Schematic of CFD model showing salient input and output parameters

## 7.4. Results and Discussion

The results from the CFD simulation are validated against the experimental results. Key parameters like pool area, pool height, spreading rate, and vaporization mass flux are discussed in sections 7.4.3-7.4.7 along with additional important results such as flashing of LNG during the initial stages of discharge and water temperature changes during the release. These two parameters are discussed in sections section 7.4.1 and 7.4.2. An error analysis was performed using the Kline McClintock Method (Kline and McClintock, 1953) for all the parameters that were determined from thermocouples and the total propagated error was determined to be around 12%. This is expressed as shaded error regions in experimentally determined values.

### 7.4.1. Flashing of LNG

When LNG is released from a pipe, it flashes initially as LNG gets heated by the walls of the pipe before it contacts the atmosphere. Figure 47 compares the vapor emanating from LNG inlet during the initial stages of the spill between the experiments

captured using normal camera (Figure 47(a)) and IR camera (Figure. 47(b)) with CFD simulation (Figure 47(c)). LNG vapor was found to be flashing for duration of 30s producing vapor and LNG droplets. During flashing methane vapor was found to ruffle the water surface causing significant disturbance in quiescent water. The momentum of the vapor was high enough to create small water droplets from the water surface. Similar disturbance in water was observed in CFD simulation when LNG vapor was emanating from the discharge pipe. The concentration of vapor during flashing was measured previously in field experiments and was typically low of the order of 2% v/v (Qi *et al.*, 2010). The visible boundary of vapor corresponding to a temperature of 10˚C was observed from IR camera present during the test. This was well represented in the CFD simulation. The temperature of vapor was approaching the temperature of air during flashing and was around 10˚C. Unlike the LNG vapor cloud which has distinct white appearance due to condensation of water droplets in air, the LNG vapor was relatively translucent providing a distinct variation in the concentration between flashing and vapor cloud formation. In the LNG experiment and CFD simulation, the height of the methane vapor extended up to the fence surrounding the trench (~1m). With further continuation of LNG spill, a dense vapor cloud was formed with significant increase in vapor cloud volume. The geometry effects including the restriction of the spill to the boundaries of the trench were also captured by the CFD simulation. On a real incidental release, LNG vapor is bound to come out of the containment first. This can be first detected by placing a low level alarm calibrated to detect methane concentrations that are lesser than their

flammability limits. This will reduce the time taken for leak detection and also the overall emergency response time.

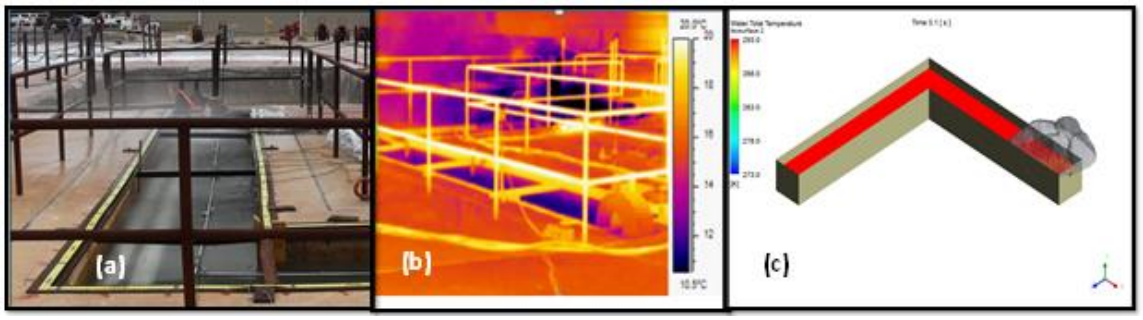


Figure 47. Comparison of flashing phenomenon from (a) normal camera (b) IR camera (c) CFD simulation

Figure 48(a) shows comparison of temperature profiles of water observed in thermocouples placed in leg 1 and leg 2 respectively. The thermocouples that were placed closer to the water surface undergo a large temperature gradient. An overall reduction in bulk water temperature of 4-14 ℃ was observed in the experiment. This is an accordance with a similar study where liquid nitrogen was found to reduce the temperature of water to about 5-10℃ during a continuous spill (Gopalaswami, Olewski, *et al.,* 2015). Similar reduction of temperature up to 8℃ was obtained in Falcon test series (Chan, 1992). It was also observed that the temperature of water in leg 1 (final temperature~6˚C) reduced to a temperature lower than thermocouples present in leg 2 (final temperature~11˚C). This is likely due to the fact that contact time of LNG with water was higher in leg 1 when compared leg 2. This temperature difference in water was sufficient to provide the heat required to vaporize the LNG spilled in the

experiment. This behavior is attributed to the large difference in heat capacity observed in LNG and water. Temperature of thermocouples placed in leg 1 of the trench was also found to reduce steeply during the experiment whereas temperature of thermocouples placed in leg 2 was found to reduce steadily with contact with LNG. This is most likely due to the fact that the spreading rate of the pool was higher in leg 1 compared to leg 2. Higher spreading rate leads to greater contact of LNG with water surface. This reflects as higher rates of heat transfer in leg 1 leading to significant reduction in temperature during the initial stages of the spill where LNG first contacts the pool. The temperature profiles from experiment were also compared to temperature profiles from CFD. The water temperature from CFD was found to match well up to duration of 600s in leg 1. After 600s, an under-prediction was obtained in CFD. This is most likely due to the formation of ice in experiment in leg 1. The ice creates a resistance between water and LNG and the measurement from thermocouple after ice formation is less likely to represent the water temperature. The water temperature of leg 2 from CFD was similar in trend compared to experimental value with a small difference.

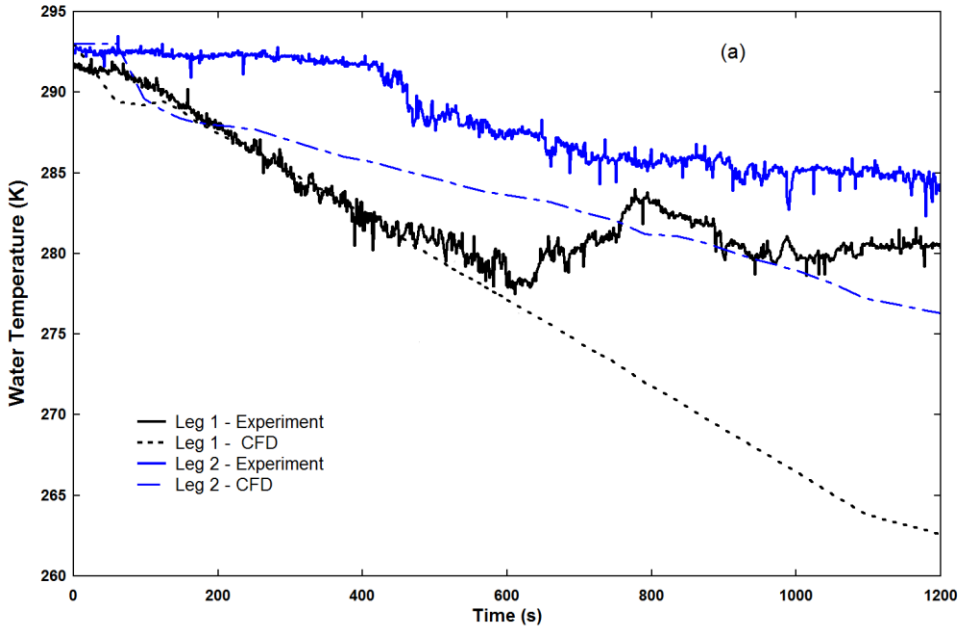


Figure 48 (a). Temperature profiles of thermocouples measuring water temperature

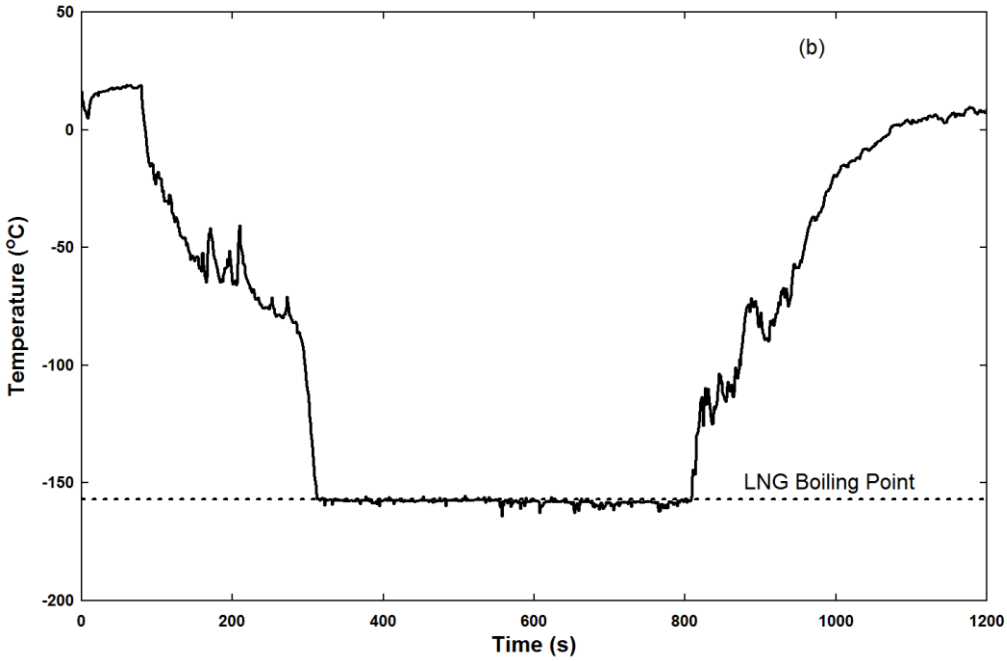


Figure 49 (b). Temperature profiles of thermocouples measuring LNG temperature

Figure 48(b) shows the temperature profiles of thermocouples placed above the water surface to measure the LNG temperature. As the pool traverses along the water surface, the temperature reads that of LNG boiling temperature indicating that LNG remained in boiling point throughout the vaporization process.

The temperature of the water reduced gradually after the cold LNG started spreading from the pool. Figure 49 provides the temperature contours at different time snapshots. During the experiment, the water temperature was found to reduce more near the discharge area when compared to other locations in the trench. As the LNG spread on water, significant amount of heat transfer occurred at the water surface. Since the incoming LNG was high near the LNG discharge area, the amount of mixing and heat transfer was also found to be high leading to high transfer. In a real spill during side-by-side loading operations, the pool is also going to follow a narrow path in the vapor space between the ships until it branches out to a larger area of open water. The temperature of water present between the ships is going to reduce more than the open water. This can lead to formation of bigger vapor cloud in the space between the two ships when compared to locations away from the ship.

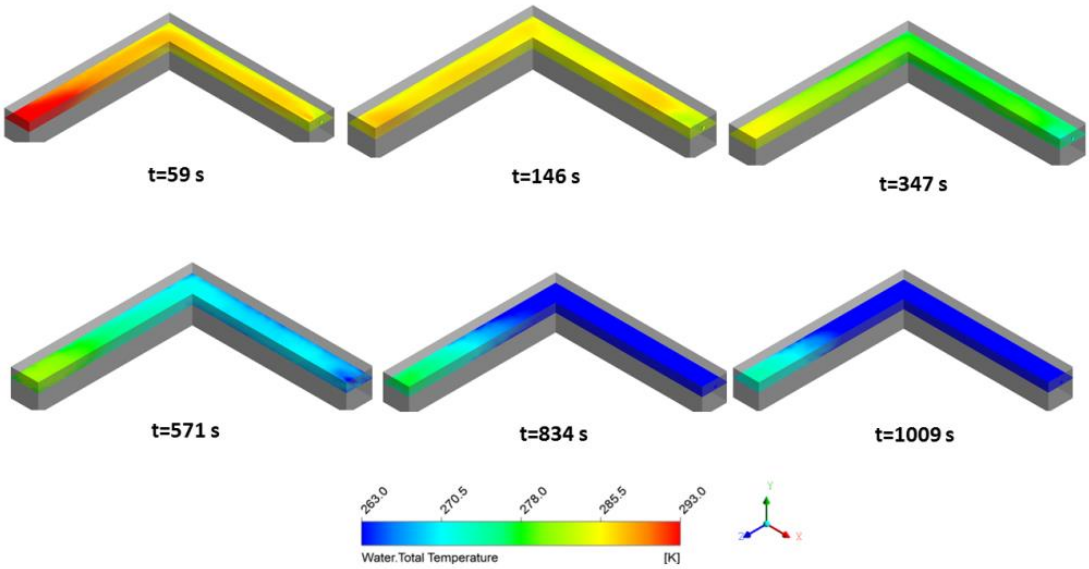


Figure 49. Timed snapshots of water temperature at different time intervals

### 7.4.2. Pool Area

The pool spreading parameters is obtained from experimental data using thermocouple measurements. Figure 50 shows the snapshots of LNG traversing on water in leg 2 section of the trench. As LNG was released into the trench, it contacts water and increases the contact area as it spreads on water. This area covered by LNG can be determined by recording the time at which the LNG pool contacts thermocouples. As the locations of the thermocouple position are prior to the experiment, the area is then determined by multiplying the length and the width from the origin. The spreading area is determined by time take by thermocouples to read LNG boiling temperature.


Figure 50. Snapshots of LNG pool (a) traversing leg 1 of trench (b) entering the leg 2 of trench (c) covering 1/8$^{th}$ of leg 2 length (d) covering 1/4$^{th}$ of leg 2 length (e) covering ½ of leg 2 length (f) covering ¾ $^{th}$ of leg 2 length (g)covering entire trench (f) regressing

A comparison of pool area between experiment and CFD simulation is provided in Figure 51. The pool spreading data points from experiment are observed as square markers in Figure 51. The shaded region around the data points represents the error associated with the experiment. The error in experiments is likely due to two reasons. While determining the pool area experimentally, it is assumed that the LNG pool covers a rectangular area of water up to the point where thermocouple is present. However, in the CFD simulation, LNG was found to cover the water surface in a non-uniform shape. The second error is due to error propagation from the thermocouples. As the pool spreads, the pool covers the first leg of the trench. This happens around 200s. The CFD results predict the pool area very well up this duration. As the pool spreads, the pool area reaches a maximum value when the LNG pool contacts the end of leg 2 of the trench.

This happens around 400s. The CFD results over-predict the pool area up this duration. This difference is attributed to the delay in wind stability in CFD. A maximum pool area is maintained for few minutes where addition of LNG into the pool increases the height, rather than the area. At this stage, the mass inflow to the pool is equalized by the LNG vaporized. It was also observed that due to high wind speed blowing in the opposite direction of pool spreading in leg 2, rapid vaporization was found to take place and the LNG pool hit the boundary of leg 2 multiple times. As a result of this, the pool was found to spread and regress multiple times in during the interval 400-700s. The CFD results follow a similar trend. Once the vaporization increases, the pool starts regressing. This is expressed as circular data points in Figure 51. This value was obtained experimentally by noting down the time at which temperature of water returns to atmospheric temperature during the experiment. With further vaporization, the pool area reduces starting from the end of second leg of trench. Once the discharge was shutoff the LNG continue to vaporize near the discharge area. This can be observed from the non-zero value of pool area observed in Figure 51. The pool continues to vaporize with maximum pool area in the CFD simulation showing an over-prediction for the duration from 900-1200s. In a real spill, the vaporization rate will increase as long as the pool is spreading. The vaporization rate will tend to remain constant once the pool has stopped spreading as long as there is no change in pool area or movement in water causing the pool to break.

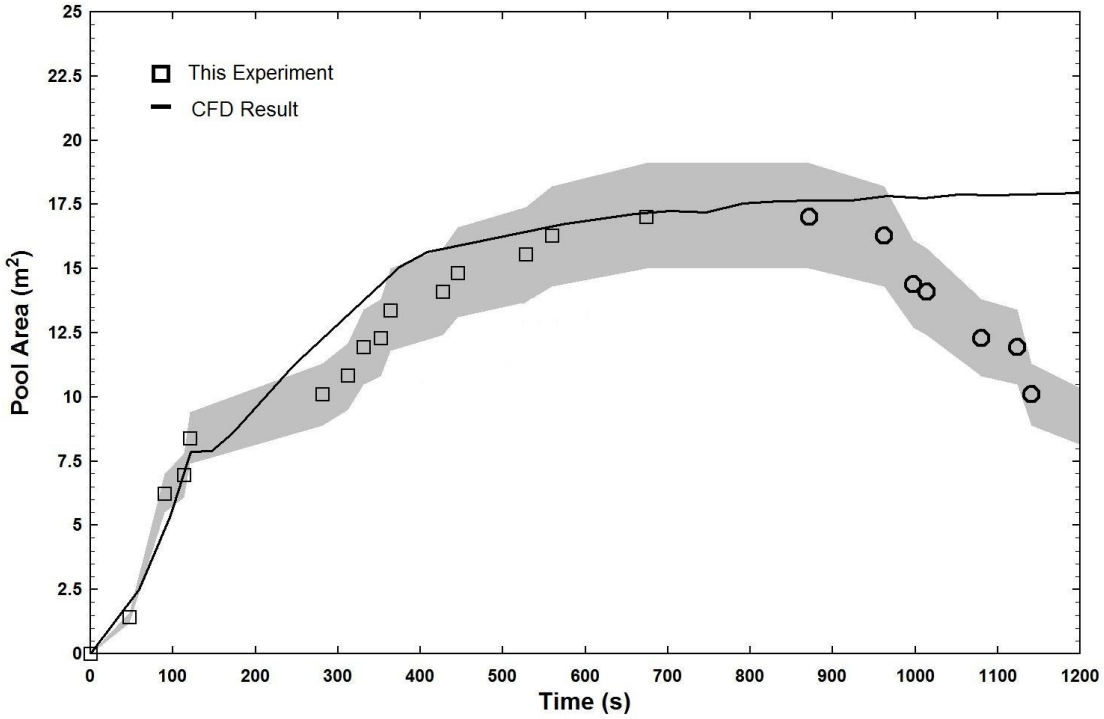


Figure 51. Comparison of pool area between experiment and CFD simulation

### 7.4.3. Spreading Rate

The spreading rate is determined from experiments by calculating the time taken to reach selected N-type thermocouples present in the experiment. Since the position of thermocouples is previously known, the velocity is then determined as distance by time. This method gives an estimate of spreading rate during the initial stage of spill, when LNG touches the thermocouples for the first time. A comparison of spreading rate from experiment and simulation is provided in Figure 52. The spreading rate increases initially up to a value of 0.06 m/s till 130s after which, the speed starts reducing to a minimum value of 0.02 m/s. However, in CFD, the maximum spreading rate in leg 1 was

around 0.08 m/s. The LNG pool was present in leg 1 up to 130s and moved to leg 2 later. After 130s the pool hits the boundary of leg 1 of the trench, where it takes a turn to leg 2 causing a reduction in speed due to hydraulic jump. The wall present at end of leg 1 of trench exerts a drag force on the moving pool that reduces the momentum of the pool. As a result of this, a marked difference in spreading rate is observed between leg 1 and leg 2 of the trench. Figure 52 also shows the velocity contour of LNG near the discharge area. The momentum of LNG pool near the discharge is very high, but as it moves away from the leak source, the momentum of the LNG pool reduces and becomes stable. The CFD results were obtained from LNG superficial velocity variable. The trend of spreading rate between experiment and CFD simulation was similar, however, the CFD was found to over-predict the velocity in leg 1. The CFD simulation was able to predict the spreading rate in leg 2 with significant accuracy. The spreading rate was found to be constant once the entire trench was covered with LNG pool.

In a real spill, wind blowing towards the ship can increase the risk of hazards as the possibility of encountering an ignition source is high in ship when compared to open waters. Slow spreading rate can lead to accumulation of vapors near the leak area, whereas, faster spreading rate will lead to increase in vaporization rate as LNG will contact more water in shorter duration. The ships can also act as barriers and will tend to reduce the momentum of the pool when it contacts the ship.

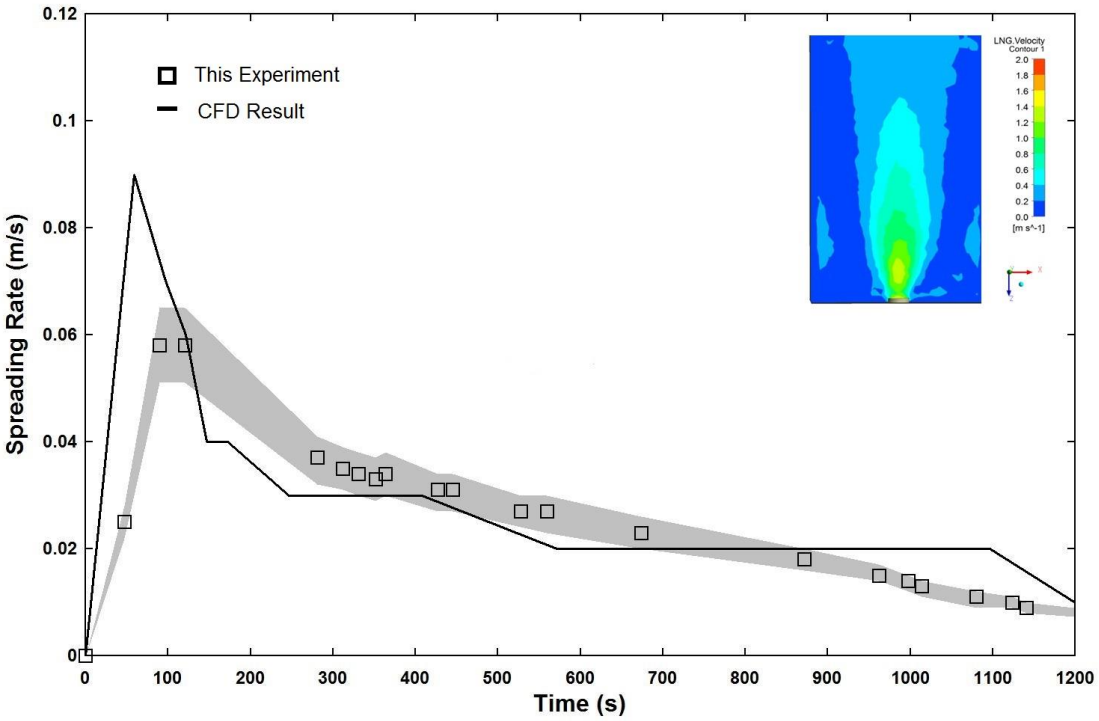


Figure 52. Comparison of spreading rate between experiment and CFD simulation. Contour shows the velocity near the discharge area

### 7.4.4. Pool Height

Pool height is one of the most important parameter which has been difficult to measure in experiments. It was also observed from previous experiments that pool height strongly affects the vaporization rate of LNG (Gopalaswami, Laboureur, *et al.*, 2015). Efforts were directed to measure pool height through multiple methods. During the entire duration of the experiment, the pool height was also measured manually using dip stick at regular intervals by a firefighter (Figure 53 (b)). The height of the pool measured manually by a firefighter using dipstick is expressed as square markers in

Figure. 53(a). The maximum height of the pool was measured manually was found to be around 0.13 m.

A linear array of thermocouples was placed on the path of the pool to determine the pool height (see Figure 53(c)). The thermocouple board was placed on the water surface and as LNG level started to increase, the thermocouples present near the water surface started to measure LNG temperature. This is observed as circular data points in Figure 53(a). As the LNG inflow to the pool increases, the contact of thermocouples from bottom to top increases. Based on the elevation of thermocouples and the time at which LNG pool contacts the thermocouple, the height is then determined with respect to time. As the pool reached the end of second leg of trench, the pool starts to regress. This is captured dynamically using ultrasonic level sensor (Figure 53(d)).

The difference in various measurements of pool height observed in Figure 53(a) is possibly due to the different location in which it was measured. Even though significant differences in pool height were observed with respect to location, less focus is provided as the spatial variation of pool height has less impact on vaporization when compared to variation of pool height with respect to time.

From Figure 53(a), we can observe that the height of the pool tends to increase only after duration of 400s. This is the time taken by the pool to reach the end of leg 2 of the trench. However, the pool height starts to increase earlier in CFD. The pool height in CFD was determined by finding out the LNG volume fraction that was more than 50%in a line. The height starts to increase and as it vaporizes, height decreases when the pool starts regressing near the end of the trench. It starts to increase again as LNG is pumped

back into the pool. These dynamic changes were recorded by ultrasonic level sensor, but were hard to capture in other experimental methods employed here. The pool height from experiments was also compared with pool height from CFD. The pool height predicted by simulation was in close agreement with the values recorded by manual measurement and array of thermocouples. The pool height was under-predicted in CFD after duration of 1100s. This is likely due to the fact that the manual measurement was taken near the intersection of leg 1 and leg 2 and the CFD results were obtained near leg 2. During these stages, the discharge of LNG into the pool was equalized by the vaporization rate of LNG.

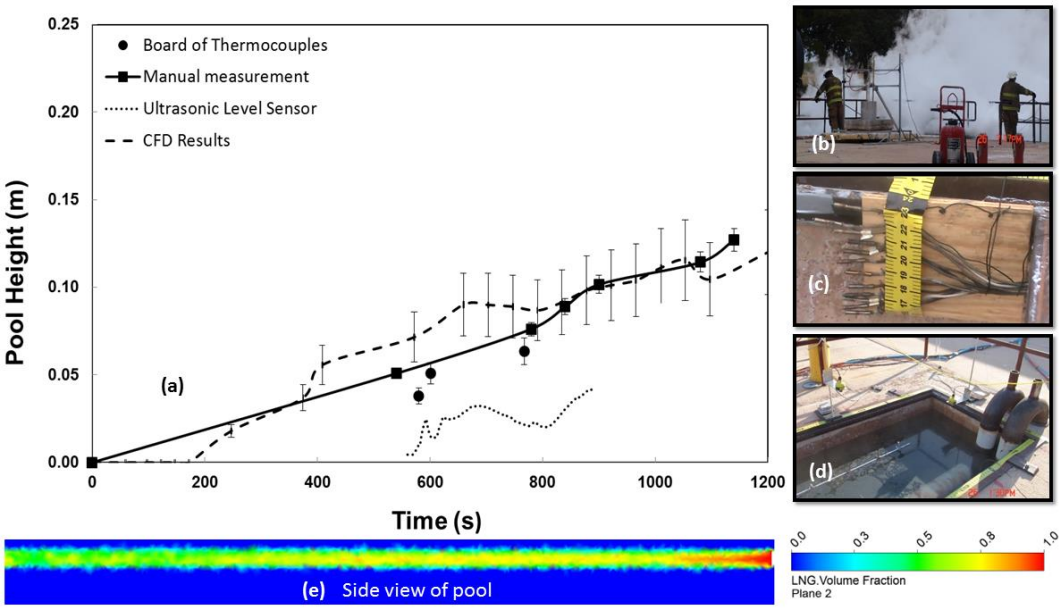


Figure 53.(a) Comparison of pool height between simulation and experiment using (b) manual measurement (c) array of thermocouples (d) ultrasonic level sensor (e) contour of LNG volume fraction indicating the height of LNG in the pool.

### 7.4.5. Vaporization Mass Flux

Vaporization mass flux is a parameter that cannot be measured directly in experiment. The vaporization mass flux from experiment is obtained from thermocouple values. The temperature of water is measured and empirical correlations on heat transfer correlations like convective boiling is applied to obtain the vaporization mass flux. This method has been widely used in small and medium-scale tests (Burgess *et al.,* 1970). The method involves a heat transfer analysis where LNG vaporization rates are estimated from an energy balance by equating the total heat input to the pool to the latent heat of vaporization of LNG. The vaporization rate in LNG experiments is determined by two other methods in the past. The first method is the measure of the loss of LNG mass that is occurring due to vaporization (Boyle and Kneebone, 1973). The vaporization rate is obtained by determining the slope of mass loss data. This method has been applied widely in small-scale experiments. The second method is to determine the rate of flow of vapor through an array of gas sensors. The vaporization rate is determined by integrating the measured concentration data across the area covered by gas sensors. This method has been widely used in large-scale LNG experiments like the Esso tests (May *et al.,* 1973). However, in this test, both mass loss measurement using weighing balance and gas detectors were not employed and hence, the vaporization mass flux was determined using thermocouple values.

The average vaporization mass flux determined from experiment is found to be around 0.2 $kg/m^2s$ in the experiment. The high initial vaporization mass flux may be accounted for by the large temperature difference that is present during the initial stages

of the continuous spill. Once the pool covered the entire water surface, the vaporization mass flux was found to remain constant at 0.195 kg/m$^2$s after a time period of 500s. The shift from 0.2 to 0.195 kg/m$^2$s shows a minor change in vaporization mass flux, after 500s. A minor change in vaporization mass flux is reflected with a significant change in vapor production. During the time period 500-800s, the pool area was maintained constant. The vaporization mass flux further reduces to 0.19 kg/m$^2$s once the pool starts regressing.

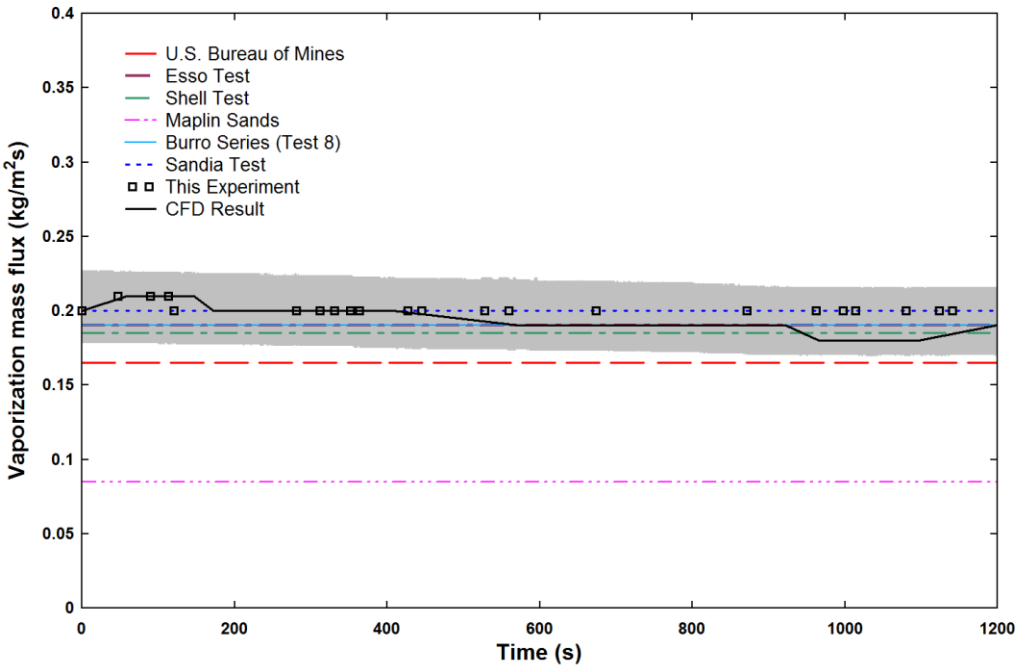


Figure 54. Vaporization mass flux and rate from experiment and CFD simulation

The vaporization mass flux from experiment was obtained by calculating the heat input from air and water. Wind had a significant influence in the vaporization mass flux.

The effect of wind on vaporization is twofold. Wind provides heat to LNG in the form of convection. Similarly, wind also makes the air above LNG unsaturated which leads increase in vaporization. Equations (62)-(64) was used to determine the vaporization mass flux from experiment. Similar methodology was used to determine the vaporization mass flux from CFD. It is to be noted that both experiment and CFD had a similar trend of vaporization mass flux. However, the vaporization mass flux in CFD was similar to experiment up to a duration of 400s. The vaporization mass flux was under-predicted by CFD after a duration of 400s. The CFD is able to predict the vaporization mass flux when the pool is spreading and under-predicts when entire trench is covered by the pool. The vaporization during regression stage in CFD is not matched well with the regression time vaporization in experiment. This is likely due to the momentary wind effects in the regression stage. The vaporization continued to occur until all the LNG vaporized from the pool. This extended the time period of vaporization to increase more than the discharge time. The vapor production is initially high and tends to decline as the time proceeds. Hence it is recommended to use a time varying vaporization mass flux as inputs to the dispersion model for accurate determination. Figure 54 provides a comparison of the vaporization fluxes determined in each test. The values of the current tests are compared with similar LNG experiments. The vaporization rates obtained in this test were comparable to values obtained in Esso Test (May W.G. et al., 1973) , Burro Series (Koopman *et al.*, 1982), Sandia Tests (Blanchat *et al.*, 2011) and Shell Test (Boyle and Kneebone, 1973b).

## 7.5. Conclusions

This chapter makes a fundamental contribution to CFD-based consequence analysis by providing a methodology for the development and validation of CFD model for LNG pool spreading and vaporization phenomenon. Additionally, experimental methods were established to measure the pool spreading parameters and vaporization mass flux. The L-shaped trench employed in this study provides a unique scenario of pool spreading in narrow pathways. The pool spreading parameters showed different trends in each leg of the trench. The wind blowing in opposite direction of the pool tends to impede the spreading phenomenon significantly. Similar wind had a significant influence on vaporization. The LSPREAD methodology was able to capture the pool spreading parameters and vaporization physics. However, differences were observed between LSPREAD and experimental values due to the ways of determination of source-term parameters.. The vaporization mass flux parameters obtained from CFD was comparable to values obtained in this experiment and LNG field experiments from the past. Through this study areas for improvement have been explored and identified. In particular, a properties dependent on a wide range of temperature and pressure is required for LNG to enable quantitative prediction of vaporization rate and the interaction of LNG with air and water with greater fidelity in CFD. Future research is also required to gain information of the sizes of droplets that are formed during flashing stage. The model also paves the way to address the action of waves on LNG pool as water is modeled as a separate fluid rather than assuming it as a wall.

# CHAPTER VIII

# CONCLUSIONS, RECOMMENDATIONS AND FUTURE WORK

This section summarizes the main findings of the work presented in this dissertation (Section 8.1) and recommendations based on the research performed (Section 8.2). The final section of this chapter outlines the opportunities to continue this research (Section 8.3).

## 8.1. Conclusions

This dissertation involved experimental and computational methods using CFD to investigate the complex aspects of LNG pool spreading and vaporization on water. This work showed different methods to measure the pool spreading and vaporization parameters. Furthermore, a novel methodology in CFD was also provided to simulate the releases of LNG on water. This methodology can be adopted to study site-specific scenarios involving leaks of LNG on water. The following conclusions were deduced from this research:

1. The key parameters influencing the pool spreading and vaporization behavior was determined by analyzing the existing data in the literature and was found to be heat flux from water, heat flux from ice (if water is ice borne), turbulence in LNG.
2. The experimental determination methods for measuring the pool spreading parameters and vaporization rates were established.
3. Determination of vaporization through water temperature measurement was found to be effective in determining the vaporization rate of LNG.

4. A methodology was developed to determine source-term from experiments and it was used a sub-model for vaporization in CFD model. The sub-model was validated with small-scale experiments.
5. A turbulence that is generated when cryogenic liquid is released on water was quantified through flow visualization experiments. The high-speed images provide important information on thermals which catalyze the vaporization process.
6. A methodology in CFD was developed to simulate the pool spreading and vaporization phenomena and was validated with LNG experiments for specific scenario of LNG leak on water.
7. Recommendations were provided for improving emergency response through the research performed.

The experimental data, methodology and techniques employed in this research help in improving the different stages of consequence analysis of LNG releases on water like vapor dispersion modeling, thermal radiation modeling and explosion modeling. A time varying vaporization mass flux can be applied for vapor dispersion modeling. Both the pool spreading parameters and vaporization parameters reported in this research can be used for modeling LNG pool fires on water. Subsequently, the research results can also be used for selecting or comparing different passive mitigation measures like Passive Fire Protection (PFP) coatings and expansion foams. Other applications of the research includes development of emergency response measures, marine facility siting

and fire and gas mapping based on cloud formation. It was also demonstrated that CFD methods can provide detailed information on the phenomenon with significant accuracy.

## 8.2. Recommendations

### 8.2.1. Recommendations for Modeling

1. The height and width of the vapor cloud is dependent on the momentum provided by the LNG pool vaporizing on water. To accurately determine this extent of the cloud, it is recommended to include the appropriate values of turbulent intensity, kinetic energy and eddy dissipation rate while modeling in CFD.
2. The vaporization rate varies with respect to time based on the amount of heat flux supplied by the water body. This vaporization rate can vary based on several factors like the size of the water body and the obstacles encountered by the pool. Current safety regulations involve the usage of single value of vaporization rate as input in vapor dispersion modeling. However, it is recommended to use a time-based vaporization rate to accurate determine the amount of vapor cloud.

### 8.2.2. Recommendations for Safeguards

1. It is recommended to mandate the use of drip trays for ships with LNG loading arms. These drip trays should be cryogenic resistant and robust against external environment. The drip trays should be connected to drainage or collection tank where LNG can be directed to a safe environment in case of a leak in the ship's deck.
2. Leaks in annular space between ships during loading operations can be identified by installing different type of leak detection equipment like temperature sensors,

low temperature alarms, cameras and other types of gas detectors. This detection equipment can be operated from the control center to trigger emergency shutdown systems if necessary.

3. LNG firefighting systems like dry chemical powder can be made available throughout the ships.
4. It was observed that the concentration of methane during flashing was lower (2-3%) than the LFL value of methane (5%). It is important to install gas detectors that are calibrated to detect concentration of methane starting from 10% LFL near loading arms and waist of the ship. This will help in faster detection of LNG leaks which initially contains vapor.
5. LNG initially flashes as it is released through the pipe. This was primarily due to heating caused by internal walls of the pipe. In the LNG experiment, the flashing was characterized by distinct whistling sound from the pipe and extended to duration of 30 – 60 seconds. The detection and reaction time for automatic isolation devices and the response time for manual operation typically took up to three minutes for fire fighters during the experiment. This valve closure time is increased for longer pipe. Therefore, the detection systems should be capable to reacting within 30s to fasten the emergency response.

## 8.3. Future Work

### 8.3.1. Effect of Composition on LNG Consequence Modeling

The current consequence modeling approaches for releases of LNG are conducted with certain level of accuracy and most of the work employ LNG composed

of pure methane in their models. However, LNG can contain methane typically from 70-100 mol% and is mixture of various components like nitrogen, methane, ethane, propane and butane. With the LNG vaporizing after spill on the ground, the light components (*e.g.* nitrogen, methane) will vaporize faster than the heavy components (*e.g.* ethane, propane, butane, etc.). Therefore, the fraction of light components will decrease and the bubble point of the LNG mixture will increase. The boiling of a hydrocarbon mixture also behaves differently from the pure components with similar physical properties due to the concentration gradients and mass diffusion effects in the liquid. Both concentration gradient and temperature gradient have to be determined simultaneously to determine the heat flux values. This is due to the fact that the vapor and liquid phases are present in different compositions during boiling. The accuracy of every step of consequence modeling, including LNG spilling, spreading, vaporization and vapor dispersion, influences the precision of this exclusion zone estimation. This exclusion distance is bound to change when the LNG composition changes as the flammability limit of the components are different. Currently there are very few models which take into account the multicomponent nature of LNG. Research can be conducted using different blends of cryogenic liquids to track the vaporization rate. Modeling can be performed by incorporating a thermodynamic model in a CFD model to study the effect of composition on the vaporization rate. The research can be performed by initially taking binary and tertiary hydrocarbons. The behavior of pure methane liquid and several different LNG compositions can also be compared.

### 8.3.2. Effect of Waves on Source-Term Modeling

Currently the effect of waves on LNG pool is unknown. A release occurring on unconfined space like oceans and seas is accompanied by the action of waves which tend to break the spreading pool. The pool breakage can result in the formation of smaller pools and subsequent smaller plumes. Previous studies have assumed waves to be stationary and have demonstrated that waves reduce the spread of the LNG pool. It is observed that as the LNG pool thins out, the gravity –driven spreading of the pool will be slow as LNG gets trapped between troughs of waves. The velocity of wave and other wave parameters which contribute to pool breakage is currently not known and computational and experimental study is proposed as a part of this research. A wave tank can be constructed to perform the experimental study. A release of LNG on waves can be performed to study the effect of wave velocity and wave height on LNG pool breakage. Once the parameters affecting the pool breakage is known, the pool diameter can be measured and hence the mass vaporization rate. The computational study can be performed by applying the airy wave theory in CFD. There are three types of waves that LNG traffic experiences – regular waves that are present in deep and shallow water, irregular waves and short crested or directional waves. The Airy wave theory can be applied to waves of different depths like deep, shallow and intermediate depth.

### 8.3.3. Cryogenic Spill Protection Optimization of LNG Assets

One of the main consequences of LNG release during marine operation is the brittle fractures caused due to exposure of metal surfaces to cryogenic liquids. This can lead to loss of assets due to failure of mechanical integrity of the ship or offshore

structure. A cryogenic spill brittle fracture analysis can be performed numerically using advanced numerical tools like CFD. The brittle fracture analysis involves an analysis of the structural integrity of the metal structures to cryogenic fluid and subsequent heat transfer. The computational analysis consists of analyzing the effect of low temperatures on metal structures using CFD, heat transfer analysis to understand the cooling behavior of metals and analyzing the structural integrity with finite element methods like LS-DYNA. The three steps are to be optimized using optimization methods to avoid total collapse and cascading effects due to LNG spill. The overall aim of the study will be to develop a prediction models for structural failures and assess the integrity of surrounding support elements to prevent total collapse or cascading effects.

### 8.3.4. LNG Release Modeling and Aerosol Formation

The release process is currently modeled using the orifice equation which takes into account the height of the liquid in reservoir, the area of the leak and LNG density. It assumes circular leak geometry and a non-flashing liquid at the orifice. However, LNG tends to flash initially during a leak due to heat offered by internal and external sections of the reservoir. LNG aerosols are formed near the impingement area. Due to rapid boiling, drops of LNG liquid fall into the cloud leading to aerosol dispersion. This phenomenon can be determined by incorporating the thermodynamics effects of the release process. Additionally, the ullage pressure of the tank is also neglected. A theoretical study is required on the LNG release modeling which incorporates the thermodynamic effects and removes the current assumptions existing for the orifice equation.

# REFERENCES


ABS. 2014. “LNG Bunkering : Technical and Operational Advisory.” American Bureau of Shipping, Houston. Retrieved from http://ww2.eagle.org/content/dam/eagle/publications/2015/LNG_Bunkering Advisory.pdf.

Ali, D. K., Drake, E. M., & Reid, R. C. (1975). Boiling of Liquid Nitrogen and Methane on Water. The effect of Initial Water Temperature. International Journal of Heat and Mass Transfer, 31(2), 176–177.

Atallah, S., Sirdesai, M., & Jennings, D. . (1993). Source1: A Model for Creating a DEGADIS Input File (No. 1GRI-92/0543). Des Plaines, IL Gas Research Institute.

Baker Engineering and Risk Consultants. (2005). "Safesite3G.Theory Manual: version 1.04" San Antonio Baker Engineering and Risk Consultants.

Batchelor, G. K., & Goldstein, S. (1982). The Theory of Homogeneous Turbulence (1st ed.). Cambridge, UK: Cambridge University Press.

Baumeister, J. K., Papell, S. S., & Robert, G. W. (1964). A Correlation of Film-Boiling Heat-transfer Coefficients Obtained with Hydrogen, Nitrogen, and Freon 113 in Forced Flow (No. NASA TN D-2294). Washington ,D.C. National Aeronautics and Space Administration

Berenson, P. J. (1961). Film-Boiling Heat Transfer From a Horizontal Surface. Journal of Heat Transfer, 83(3), 351–356.

Bevington, P. R., & Robinson, K. D. (2003). Error Analysis. In Daryl Bruflodt (Ed.), Data Reduction and Error Analysis for Physical Sciences (Third, pp. 36–46). New York: McGraw-Hill.

Blanchat, T., Helmick, P., Jensen, R., Luketa, A., Deola, R., Suo-Anttila, S., Mercier, J., Miller, T., Ricks, A., Simpson, R., Demosthenous, B., Tieszen, S., and Hightower, M., (2010). Summary of the Phoenix Series Large Scale LNG Pool Fire Experiments (No. SAND2010-8676). Albuquerque. Sandia National Laboratories, Retrieved from http://prod.sandia.gov/techlib/access-control.cgi/2010/108676.pdf

Boyle, G. ., & Kneebone, A. (1973a). Laboratory Investigations into the Characteristics of LNG Spills on Water. Evaporation, Spreading and Vapor Dispersion (No. 6Z32). Chester. Shell Research Limited, Thronton research centre

Briscoe, F., & Shaw, P. (1980). Spread and Evaporation of Liquid. Progress in Energy and Combustion Science, 6(1), 127–140.

Burgess, D. ., Murphy, J. ., & Zabetakis, M. . (1970). Hazards of LNG Spillage in Marine Transportation. Pittsburgh, Pennsylvania. U.S Department of the Interior, Bureau of Mines

Burgess, D., Biordi, J., & Murphy, J. (1972). Hazards of Spillage of LNG into Water. Pittsburg, Pennslyvania. U.D Department of the Interior, Bureau of Mines

Bushuyev, A. V. (1970). Sea Ice Nomenclature (No. WMO/OMM/BMO - No.259). Russian Federation World Maritime Organization,. Retrieved from http://www.aari.nw.ru/gdsidb/docs/wmo/nomenclature/WMO_Nomenclature_draft_version1-0.pdf

Caldwell, D. R. (2006). Experimental Studies on the Onset of Thermohaline Convection. Journal of Fluid Mechanics, 64(02), 347. http://doi.org/10.1017/S0022112074002436

Carslaw, H. S., & Jaeger, J. C. (1986). Conduction of Heat in Solids (2nd ed.). Oxford University Press, USA.

Cavanaugh, T. A., Siegell, J. H., & Steinberg, K. W. (1994). Simulation of Vapor Emissions from Liquid Spills. Journal of Hazardous Materials, 38(1), 41–63. http://doi.org/10.1016/0304-3894(93)E0111-E

Chan, S. T. (1992). Numerical Simulations of LNG Vapor Dispersion from a Fenced Storage Area. Journal of Hazardous Materials, 30(2), 195–224. http://doi.org/10.1016/0304-3894(92)85078-F

Colinet, P., Joannes, L., Iorio, C. ., Haut, B., Bestehorn, M., Lebon, G., & Legos, J. C. (2003). Interfacial Turbulence in Evaporating Liquids: Theory and Preliminary Results of the ITEL-MASTER 9 Sounding Rocket Experiment. Advanced Space Research, 32(2), 119–127. http://doi.org/10.1016/S0273-1177(03)90241-9

Cormier, B. R., Qi, R., Yun, G., Zhang, Y., & Sam Mannan, M. (2009). Application of Computational Fluid Dynamics for LNG Vapor Dispersion Modeling: A Study of Key Parameters. Journal of Loss Prevention in the Process Industries, 22(3), 332–352. http://doi.org/10.1016/j.jlp.2008.12.004

Dahl, K. A. (2012). Analysis of Accidental Iceberg Impacts with LNG Tank Carriers. Norwegian University of Science and Technology. Retrieved from http://www.diva-portal.org/smash/get/diva2:566152/FULLTEXT01.pdf

Diemand, D. (2001). Icebergs. In Encyclopedia of Ocean Sciences (2nd Editio, pp. 1255–1264). Elsevier Science & Technology Books.

http://doi.org/10.1006/rwos.2001.0002

DNV (Det Norske Veritas). (2012). PHAST Consequence Modelling Software version 6.7. Hovik ,Norway: DNV Corporate Headquarters.

Dodge, F., Park, J. T., Buckingham, J. C., & Magott, R. . (1983). Revision and Experimental Verification of the Hazard Assessment Computer System Models for Spreading, Movement, Dissolution, and Dissipation of Insoluble Chemicals Spilled onto Water (No. Report CG-D-35-83). Washington, DC 20593. U.S. Department of Transportation , United States Coast Guard

Drake, E. M., Jeje, A. a., & Reid, R. C. (1975a). Transient Boiling of Liquefied Cryogens on a Water Surface I. Nitrogen, Methane and Ethane. International Journal of Heat and Mass Transfer, 18(12), 1361–1368. http://doi.org/10.1016/0017-9310(75)90249-5

Drake, E. M., Jeje, A. A., & Reid, R. C. (1975b). Transient Boiling of Liquefied Cryogens on a Water Surface. II Light Hydrocarbon Mixtures. International Journal of Heat and Mass Transfer, 18(12), 1369–1375. http://dx.doi.org/10.1016/0017-9310(75)90250-1

Fannelop, T. K., & Waldman, G. D. (1972). Dynamics of Oil Slicks. American Institute of Aeronautics and Astronautics Journal, 10, 506–510.

Fay, J. a. (2007). Spread of Large LNG Pools on the Sea. Journal of Hazardous Materials, 140(3), 541–51. http://doi.org/10.1016/j.jhazmat.2006.10.024

Fdida, N., Blaisot, J. B., Rouland, E., Bégin, V., Rouvray, S., & Cedex, V. (2010). Velocity Measurements of Bubbles in Liquid Nitrogen. 23rd Annual Conference on Liquid Atomization and Spray Systems, 2(September), 1–14. Retrieved from http://www.ilasseurope.org/ICLASS/ilass2010/FILES/ABSTRACTS/045.pdf

Forster, H. K., & Zuber, N. (1955). Dynamics of Vapor Bubbles and Boiling Heat Transfer. AIChE Annual Meeting, 1(4), 531–535.

Foss, M. M. (2006). Offshore LNG Receiving Terminals. Austin, Texas. Retrieved from http://www.beg.utexas.edu/energyecon/lng/LNG_OFFSHORE_RECEIVING_TERMINALS-release-updated.pdf

Gavelli, F., Chernovsky, M. K., Bullister, E., & Kytomaa, H. K. (2009). Quantification of Source-Level Turbulence during LNG Spills onto a Water Pond. Journal of Loss Prevention in the Process Industries, 22(6), 809–819. http://doi.org/10.1016/j.jlp.2009.08.015

Gonzalez, R. C., Woods, R. E., & Eddings, S. L. (2006). Digital image processing using Matlab. New Jersey: Pearson Prentice Hall.

Gopalaswami, N., Laboureur, D. M., Mentzer, R. A., & Mannan, M. S. (2015). Quantification of turbulence in cryogenic liquid using high speed flow visualization. Journal of Loss Prevention in the Process Industries. http://doi.org/10.1016/j.jlp.2015.08.005

Gopalaswami, N., Mentzer, R. A., & Sam Mannan, M. (n.d.). Investigation of pool spreading and vaporization behavior in medium-scale LNG tests. Journal of Loss Prevention in the Process Industries, (0). http://doi.org/http://dx.doi.org/10.1016/j.jlp.2014.10.012

Gopalaswami, N., Olewski, T., Véchot, L. N., & Mannan, M. S. (2015). Small-scale experimental study of vaporization flux of liquid nitrogen released on water. Journal of Hazardous Materials, 297(0), 8–16. http://doi.org/http://dx.doi.org/10.1016/j.jhazmat.2015.04.057

Gopalaswami, N., Vechot, L., Olewski, T., & Mannan, M. S. (2015). Small-Scale Experimental Study of Vaporization Flux of Liquid Nitrogen Released on Ice. Journal of Loss Prevention in the Process Industries. http://doi.org/10.1016/j.jlp.2015.07.006

Gui, L., Merzkirch, W., & Fei, R. (2000). A digital mask technique for reducing the bias error of the correlation-based PIV interrogation algorithm. Experiments in Fluids, 29(1), 30–35. http://doi.org/10.1007/s003480050423

Hissong, D. W. (2007). Keys to modeling LNG spills on water. Journal of Hazardous Materials, 140(3), 465–77. http://doi.org/10.1016/j.jhazmat.2006.10.040

Ivings, M. J., & Webber, D. M. (2007). Modelling bund overtopping using a shallow water CFD model. Journal of Loss Prevention in the Process Industries, 20(1), 38–44. http://doi.org/10.1016/j.jlp.2006.08.004

Jeje, A. A. (1974). Transient Pool Boiling of Cryogenic Liquids on Water. Boston, Massachusetts Institute of technology.

Kalinin, E. K., Berlin, I. I., Kostyuk, V. V, & Nosova, E. M. (1976). Heat transfer in transition boiling of cryogenic liquids. Advances in Cryogenic Engineering, 21, 273–277.

Klimenko, V. V. (1981). Film boiling on a horizontal plate — new correlation. International Journal of Heat and Mass Transfer, 24(1), 69–79. http://doi.org/10.1016/0017-9310(81)90094-6

Kline, S. J., & McClintock, F. A. (1953). Describing Uncertainties in Single-Sample Experiments. Mechanical Engineering, 75, 3–8.

Koopman R.P., Cederwall R.T., Ermak D.L, Goldwire H.C. Jr., Hogan W.J., McClure, J.W., McRae T.G., Morgan D.L., Rodean H.C., Shinn J.H. (1982). Analysis of Burro Series 40$m^3$ LNG Spill Experiments. Journal of Hazardous Materials, 6, 43–83.

Kuhs, W. F., & Lehmann, M. . (1986). The Structure of Ice-Ih. In Water Science Review (pp. 1–66). Cambridge University Press. Retrieved from http://dx.doi.org/10.1017/CBO9780511897504.001

Laboureur, D., Aprin, L., Osmont, a., Buchlin, J. M., & Rambaud, P. (2013). Small Scale Thin-Layer Boilover Experiments: Physical Understanding and Modeling of the Water Sub-layer Boiling and the Flame Enlargement. Journal of Loss Prevention in the Process Industries, 26(6), 1380–1389. http://doi.org/10.1016/j.jlp.2013.08.016

Launder, B. E., & Spalding, D. (1974). The Numerical Computation of Turbulent Flows. Computer Methods in Applied Mechanics and Engineering, 3(2), 169–289.

Lazar, E., Deblauw, B., Glumac, N., Dutton, C., & Elliott, G. (2010). A Practical Approach to PIV Uncertainty Analysis. In 27th AIAA Aerodynamic Measurement Technology and Ground Testing Conference (pp. 1–22). Chicago. Retrieved from http://enu.kz/repository/2010/AIAA-2010-4355.pdf

Lee, S., & Nguyen, H. (2011). LNGC Collision Response Analysis with Iceberg Considering Surrounding Seawater. In Proceedings of the twenty-first (2011) International Offshre and Polar Engineering Conference (Vol. 8, pp. 1128–1135). Maui, Hawaii: International Soceity of Offshore and Polar Engineers (ISOPE). Retrieved from http://www.isope.org/publications/proceedings/ISOPE/ISOPE 2011/data/papers/11HIP-07Lee.pdf

Luketa-Hanlin, A., Koopman, R. P., & Ermak, D. L. (2007). On the Application of Computational Fluid Dynamics Codes for Liquefied Natural Gas Dispersion. Journal of Hazardous Materials, 140(3), 504–17. http://doi.org/10.1016/j.jhazmat.2006.10.023

Martins, M. R., de Souza, G., & Ikeda, N. H. (2011). Consequence Analysis of a Liquefied Natural Gas Floating Production Storage Offloading (LNG FPSO) Leakage. In Proceeding of the ASME 2011 30t International Conference on Ocean, Offshore and Arctic Engineering (OMAE 2011) (pp. 1–8). Rotterdam, The Netherlands. Retrieved from http://www.gbv.de/dms/tib-ub-hannover/717430790.pdf

May W.G., McQueen, W., & Whipp, R. . (1973). Spills of LNG on Water. In Operating Section proceedings (p. D–140– D–150). Arlington, VA: American Gas Association.

Melheim, J. A., Ichard, M., & Pontiggia, M. (2009). Towards a Computational Fluid Dynamics Methodology for Studies of Large Scale LNG Releases. In Hazards XXI-Process Safety and Environmental Proctection (pp. 336–343). Manchester.

Morse, T. L., & Kytömaa, H. K. (2011). The Effect of Turbulence on the Rate of Evaporation of LNG on Water. Journal of Loss Prevention in the Process Industries, 24(6), 791–797. http://doi.org/10.1016/j.jlp.2011.06.004

Moura, Carlos A de, and Carlos S Kubrusly. 2012. The Courant-Friedrichs-Lewy (CFL) Condition: 80 Years After Its Discovery. Edited by Carlos A. de Moura and Carlos S. Kubrusly. 1st ed. New York: Birkhäuser Basel. doi:10.1007/978-0-8176-8394-8.

Nakanishi, E., & Reid, R. C. (1971). Liquefied Natural Gas-Water Reactions. Chemical Engineering Progress, 67(12), 36–41.

Okhotsimskii, A., & Hozawa, M. (1998). Schlieren Visualization of Natural Convection in Binary Gas –Liquid Systems. Chemical Engineering Science, 53(14), 2547–2573. http://doi.org/10.1016/S0009-2509(98)00092-X

Olewski, T., Véchot, L., & Mannan, M. S. (2013). Study of the Vaporization Rate of Liquid Nitrogen by Small- and Medium-Scale Experiments. Chemical Engineering Transactions, 31(1), 133–138. Retrieved from http://www.aidic.it/cet/

Opschoor, G. (1977). Investigations into the Spreading and Evaporation of LNG Spilled on Water. Cryogenics, 17(11), 629–634.

Otsu, N. (1979). A Threshold Selection Method from Gray-Level Histograms. IEEE Transactions on Systems, Man and Cybernetics, 9, 62–66. http://doi.org/10.1109/TSMC.1979.4310076

Otterman, B. (1975). Analysis of Large LNG Spills on Water Part 1 : Liquid Spread and Evaporation. Cryogenics, 15(8), 455–460.

Park, J. T., Derradji-Aouat, A., Baoshan, W., Nishio, S., & Jacquin, E. (2008). Uncertainty Analysis Particle Imaging Velocimetry ITTC 7.5-01-03-03. In 25th Annual International Towing Tank Conference by Specialist Committee on uncertainty analysis. Fukuoka, Japan: ITTC. Retrieved from http://ittc.sname.org/CD 2011/pdf Procedures 2011/7.5-01-03-03.pdf

Puttock, J. S., Blackmore, D. R., & Colenbrander, G. W. (1982). Field Experiments on Dense Gas Dispersion. Journal of Hazardous Materials, 6, 13–41.

Qi, R., Ng, D., Cormier, B. R., & Mannan, M. S. (2010). Numerical Simulations of LNG Vapor Dispersion in Brayton Fire Training Field tests with ANSYS CFX. Journal of Hazardous Materials, 183(1-3), 51–61. http://doi.org/10.1016/j.jhazmat.2010.06.090

Raj, P. K. (1981). Models for Cryogenic Liquid Spill Behavior on Land and Water. Journal of Hazardous Materials, 5(1-2), 111–130. http://doi.org/10.1016/0304-3894(81)85009-1

Sharqawy, M. H., Lienhard V, J. H., & Zubair, S. M. (2010). Thermophysical Properties of Seawater: A Review of Existing Correlations and Data. Desalination and Water Treatment, 16, 354–380. http://doi.org/10.5004/dwt.2011.2947

Taylor, J. R. (1996). Introduction to Error Analysis. (Ann McGuire, Ed.) (2nd ed.). Sausalito, California: University Science Books.

Thielicke, W. (2014). The Flapping Flight of Birds – Analysis and Application. Netherlands, University of Groningen. Retrieved from http://irs.ub.rug.nl/ppn/382783069

Thielicke, W., & Stamhuis, E. J. (2010). PIVLab- Time Resolved Digital Particle Induced Velocimetry Tool for MATLAB,. Massachusetts.Mathworks Inc

Tsinober, A. (2009). An Informal Conceptual Introduction to Turbulence. (A. Tsinober, Ed.) (Vol. 92). Dordrecht: Springer Netherlands. http://doi.org/10.1007/978-90-481-3174-7

Vesovic, V. (2007). The Influence of Ice Formation on Vaporization of LNG on Water Surfaces. Journal of Hazardous Materials, 140, 518–526. http://doi.org/10.1016/j.jhazmat.2006.10.039

Waite, P. J., Whitehouse, R. J., Wakbham, W. A., & Winn, E. B. (1983). The Spread and Vaporisation of Cryogenic Liquids on Water. Journal of Hazardous Materials, 8, 165–184.

Webber, D M. 1991. “Source Terms.” Journal of Loss Prevention in the Process Industries 4 (June 1990): 5–15. http://dx.doi.org/10.1016/0950-4230(91)80002-C.

Webber, D. M., Gant, S. E., Ivings, M. J., & Jagger, S. F. (2010). LNG Source Term Models for Hazard Analysis: A Review of the State-of-the-Art and an Approach to Model Assessment (No. Research Report: RR789). HSE Books. Buxton,

Derbyshire, UK. Retrieved from http://www.hse.gov.uk/research/rrpdf/rr789.pdf

Webber, D. M., & Ivings, M. J. (2010). Modelling Bund Overtopping using Shallow Water Theory. Journal of Loss Prevention in the Process Industries, 23(5), 662–667. http://doi.org/http://dx.doi.org/10.1016/j.jlp.2010.07.002

Zheligovskaya, E. a, & Malenkov, G. G. (2006). Crystalline Water Ices. Russian Chemical Reviews, 75(1), 57–76. http://doi.org/10.1070/RC2006v075n01ABEH001184

Zhou, X., Doup, B., & Sun, X. (2013). Measurements of Liquid-Phase Turbulence in Gas–Liquid Two-phase flows using Particle Image Velocimetry. Measurement Science and Technology, 24(12), 125303. http://doi.org/10.1088/0957-0233/24/12/125303

Zuiderveld, K. (1994). Contrast Limited Adaptive Histograph Equalization. In Graphic Gems IV (pp. 474–485). San Deigo.